

# Numerical Solution of the Schrödinger Equation on Unbounded Domains

Inaugural-Dissertation  
zur Erlangung des akademischen Grades  
*Doktor der Naturwissenschaften*  
im Fachbereich Mathematik und Informatik  
der Mathematisch-Naturwissenschaftlichen Fakultät  
der Westfälischen Wilhelms-Universität Münster

eingereicht von

**Maike Schulte**  
aus Ahaus

betreut durch  
Prof. Dr. Anton Arnold

am  
Institut für Angewandte und Numerische Mathematik  
der Westfälischen Wilhelms-Universität Münster

Münster, November 2007

Dekan:

Prof. Dr. Dr. h.c. Joachim Cuntz

Erster Gutachter:

Prof. Dr. Anton Arnold

Zweiter Gutachter:

Prof. Dr. Helmut Maurer

Tag der mündlichen Prüfung:

Tag der Promotion:





# Contents

<b>Introduction</b>	<b>7</b>
<b>Acknowledgements</b>	<b>9</b>
<b>1 Transparent boundary conditions for quantum-waveguide simulations</b>	<b>10</b>
1.1 Introduction . . . . .	10
1.2 Finite difference scheme and DTBCs for the 2D Schrödinger equation	12
1.3 Numerical results . . . . .	16
1.3.1 Implementation of DTBCs . . . . .	16
1.3.2 Implementation of ABCs . . . . .	17
1.3.3 Example 1: Travelling Gaussian waves . . . . .	19
1.3.4 Example 2: Simulation of quantum waveguides . . . . .	23
Bibliography . . . . .	26
<b>2 DTBCs for the Schrödinger equation – a higher compact order scheme</b>	<b>27</b>
2.1 Introduction . . . . .	27
2.2 A fourth order difference scheme for the Schrödinger equation . .	30
2.3 DTBCs for the fourth order difference scheme . . . . .	33
2.4 Asymptotic behaviour of the convolution coefficients . . . . .	38
2.5 Numerical tests . . . . .	44
2.5.1 Example 1: Travelling Gaussian wave functions . . . . .	44
2.5.2 Example 2: Simulation of quantum waveguides . . . . .	51
2.6 Conclusion . . . . .	61
Bibliography . . . . .	62
<b>3 Transient quantum simulations for the double gate MOSFET</b>	<b>66</b>
3.1 Introduction . . . . .	66
3.2 Overview of the analytical model . . . . .	68
3.2.1 Subband decomposition of the analytical 2D Schrödinger equation . . . . .	71
3.2.2 Adding the self-consistent potential . . . . .	72
3.3 Discretization of the Schrödinger-Poisson system . . . . .	75
3.3.1 Extended DTBCs for the discretized Schrödinger equation	75
3.3.2 Discretizing the Poisson equation . . . . .	78

## Contents

---

3.3.3	Implementation of the model . . . . .	78
3.4	Numerical results . . . . .	81
3.4.1	Example 1: $y$ -dependent potentials in the outer domains .	81
3.4.2	Example 2: A solution to the Schrödinger-Poisson system .	82
3.5	Conclusion . . . . .	87
	Bibliography . . . . .	91
<b>4</b>	<b>DTBCs for the two dimensional Schrödinger equation on circular do-</b>	
	<b>main</b>	<b>92</b>
4.1	Introduction . . . . .	92
4.1.1	Analytic TBCs for the 2D Schrödinger equation on circular domains . . . . .	93
4.1.2	The difference equations . . . . .	94
4.2	DTBCs for circular domains . . . . .	95
4.2.1	Mass conservation property . . . . .	96
4.2.2	DTBCs for a single azimuth mode . . . . .	98
4.2.3	Calculation of the convolution coefficients . . . . .	100
4.2.4	Examples of the calculation of coefficients $\ell_j^{(n)}$ . . . . .	104
4.2.5	Two dimensional DTBCs for circular domains . . . . .	104
4.3	Approximation by sums of exponentials . . . . .	106
4.3.1	Fast evaluation of the discrete convolution . . . . .	109
4.4	Numerical results . . . . .	110
4.4.1	Example 1 . . . . .	110
4.4.2	Example 2 . . . . .	111
4.4.3	Example 3 . . . . .	115
	Bibliography . . . . .	125

# Introduction

In this thesis we discuss and analyze the results on open boundary conditions for the two-dimensional time-dependent Schrödinger equation. The aim of the research presented here is to derive new mathematical models for the simulation of novel electronic devices of nanoscale dimensions. Within these models it is possible to study the electron flow through devices and their operations like the switching behaviour between on- and off states. In practice, devices consist of an “active region” (often having a complicated geometry) which is connected to leads or contact regions. Compared to the domain of interest, these leads are so long that they are usually modeled as infinitely long. For numerical purposes it is hence necessary to reduce the computational domain of the simulation model to a small region around the domain of interest – however, without changing the simulation results. Hence we need to use *artificial boundary conditions* at the cut-offs of the computational domain. These boundary conditions are called *transparent*, if the solution on the restricted area with the new boundary conditions coincides with the solution on the unbounded domain (i.e. the channel). The main focus of this thesis is the discretization of such artificial boundary conditions in conjunction with various finite difference schemes for the Schrödinger equation.

The thesis consists of the following four sections:

In §1 we present a short overview on existing transparent boundary conditions for the Schrödinger equation and show some new two dimensional simulations. We will compare numerical results obtained with different types of artificial boundary conditions. The results of this first chapter will be published in *Mathematics and Computers in Simulation* (2007), Proceedings of MATHMOD 2006, Vienna, Austria and in the *Proceedings in Applied Mathematics and Mechanics* (2008).

In the second chapter we derive a new discretization scheme of the two dimensional Schrödinger equation. We prove the  $\ell^2$ -norm preservation of the highly accurate scheme and analyze the obtained transparent boundary conditions in detail. In several examples we present numerical tests concerning the error due to the scheme and to the boundary conditions. These results will appear in a joint work with Prof. Dr. Anton Arnold in *Kinetic and related models* **1** (2008).

§3 deals with some physical extensions of the model and of the artificial bound-

## Introduction

---

ary conditions. We relax the strong assumptions on external potentials that were needed for the analysis presented in §1 and §2. Additionally, we include a self-consistent potentials derived through a nonlinear coupling between the Schrödinger and the Poisson equation. With this model it is possible to simulate semiconductor devices like the *double gate metal oxide semiconductor field-effect transistor*. Furthermore, we reduce the numerical effort for the calculation of the solution by introducing a highly efficient algorithm based on “subband decompositions”. This amounts to projecting the solution onto the (local) Schrödinger eigenfunctions in the orthogonal direction to the device channel. The work presented in §3 has been developed under supervision of Prof. Dr. Naoufel Ben Abdallah of the Laboratoire MIP - Mathématiques pour l’Industrie et la Physique in Toulouse, France and will be submitted in 2008.

Finally we present results for the Schrödinger equation on circular domains in §4. Therefore we consider the 2D Schrödinger equation in polar coordinates and derive new transparent boundary condition for the discretized Schrödinger equation. After a stability analysis we give some numerical examples. These results will be submitted in a joint work with Prof. Dr. Anton Arnold, Dr. Matthias Ehrhard, and Prof. Dr. Ivan Sofronov in 2007.

# Acknowledgements

I would like to express my gratitude to all those who gave me the possibility to complete this thesis. I thank my Ph.D. adviser Anton Arnold for his supervision, his support, for answering questions and for several fruitful discussions. It was a great pleasure to be a part of the research group under his mentoring in a very pleasant working atmosphere.

I also like to thank my colleagues at the Universities of Münster and Vienna, especially Jens Bierwirth, Dr. Tareq Amro and Prof. Dr. Helmut Maurer for their support. My acknowledgement is also addressed to Prof. Dr. Naoufel Ben Abdallah and Dr. Matthias Ehrhardt who gave me the opportunities to work in productive collaborations in Toulouse and Berlin for several weeks.

For financial support I would like to thank the European network HYKE and the DFG research center MATHEON.

Special thanks go to my family, my parents Bernhard and Margareta Schulte and my brothers and sisters Nils, Birte and Anne for all their support during the years of my studies. Finally I thank Tobias Kerkering for his patience, his support on computer stuff, mathematical conservation and putting up with me and my moods during this time.

# 1 Transparent boundary conditions for quantum-waveguide simulations

In this first chapter we give an introduction to open boundary problems for the time-dependent Schrödinger equation. We will show some numerical results obtained with different numerical methods for simulating open quantum systems.

## 1.1 Introduction

Quantum waveguides are novel electronic switches of nanoscale dimensions. They are made of several different semiconductor materials such that the electron flow is confined to small channels or waveguides. Due to their sandwiched structure the relevant geometry for the electron current is roughly two dimensional. Using external electrostatic potentials the “allowed region” for the electrons, and hence the geometry can be modified. This allows to control the current flow through such an electronic device. It makes it a switch, which resembles a transistor, but on a nanoscale.

Being quantum particles, the electron transport through a quantum waveguide can be modeled in good approximation by a two dimensional, time-dependent Schrödinger equation

$$\begin{aligned} i\hbar\frac{\partial}{\partial t}\psi(x, y, t) &= \left(-\frac{\hbar^2}{2m^*}\Delta + V(x, y, t)\right)\psi(x, y, t), \quad (x, y) \in \Omega(t), t > 0, \\ \psi(x, y, 0) &= \psi^I(x, y), \quad (x, y) \in \Omega(0), \\ \psi(x, y, t) &= 0, \quad (x, y) \in \partial\Omega(t) \end{aligned} \tag{1.1}$$

on a time-dependent geometry  $\Omega(t) \subset \mathbb{R}^2$  with  $\psi^I \in L^2(\Omega(0))$  and homogeneous Dirichlet boundary conditions.  $\hbar$  and  $m^*$  denote the Planck constant and effective mass, respectively;  $\Delta$  the 2D Laplacian. The external potential satisfies  $V(\cdot, t) \in L^\infty(\Omega(t))$  and  $V(x, y, \cdot)$  is piecewise continuous. The spatial domain consists of (very long) leads and the active switching region, which sometimes has the shape of a stub. Here, we shall only consider domains  $\Omega(t)$  that are piecewise constant in  $t$  and monotonously growing in time. At the jump discontinuities of the domain we shall extend the solution  $\psi$  by zero, as a new initialization.

In typical applications, electrons are continuously fed into the leads. Depending on the size and shape of the stub, the electron current is either reflected (*off-state* of the device) or it can flow through the device (*on-state*). Since the applied external potential can modify the stub size, it hence allows to switch the device. Important device data for practitioners are the ratio between the on- and the (residual) off-current as well as the switching time between these two stationary states. These data can be obtained from numerical simulations of the described Schrödinger equation model. The leads are very long compared to the typical size of the active region and they usually only carry (linear combinations of) plane wave solutions. For the efficiency of numerical simulations it is therefore desirable to restrict the simulation model to a small region close to the stub (see Figure 1.5). Hence, the leads should to be cut off by using artificial boundary conditions. This is possible without changing the solution of the Schrödinger equation by introducing *transparent boundary conditions* (TBCs), which are non-local in time (convolution type) and in space.

To illustrate the idea we first consider the time-dependent Schrödinger equation (1.1) in one dimension  $x \in \Omega(t) \subset \mathbb{R}$  with a potential that satisfies  $V(x, t) = V_l$  for  $x \leq x_l$  and  $V(x, t) = V_r$  for  $x \geq x_r$  and all  $t \geq 0$ . The analytic TBC for this one dimensional equation reads

$$\psi_x(x_r, t) = -\sqrt{\frac{\hbar}{2\pi m^*}} e^{-i\frac{\pi}{4}} e^{-i\frac{V_r}{\hbar}t} \frac{d}{dt} \int_0^t \frac{\psi(x_r, \tau) e^{i\frac{V_r \tau}{\hbar}}}{\sqrt{\tau - t}} d\tau, \quad t > 0, \quad (1.2)$$

for the right boundary  $x = x_r$  (and analogously for the left boundary) and was first derived in [Pa82], [BaPo91]. The numerical discretizations of this artificial boundary condition is delicate, as it may easily render the initial-boundary value problem unstable. *Discrete transparent boundary conditions* (DTBCs) for a Crank-Nicolson finite difference discretization of the Schrödinger equation were first given in [Ar98] and [EhAr01] (cf. also [AABES07] for a recent review of the various alternative approaches). Another strategy to simulate open quantum systems consists in the use of *absorbing boundary conditions* (ABCs). ABCs are local approximations to the exact TBCs. These boundary conditions minimize the reflections at the artificial boundary, e.g. based on pseudodifferential approaches. ABCs may be also derived by an enlargement of the computational domain and applying penalty potentials, like it was done in [Bu97].

For the two dimensional geometry of quantum waveguides, TBCs were rigorously derived in [BeMePi05]. A discrete analogue along with a fast evaluation algorithm was given in [ArEhSo03]. The topic of this introducing chapter is to discuss the algorithmic issues of implementing these DTBCs for the 2D Schrödinger equation (§1.3.1), to compare them with ABCs (§1.3.2, §1.3.3) and to use

## 1 Transparent boundary conditions for quantum-waveguide simulations

---

them for simulating a quantum waveguide with a resonating stub (§1.3.4). A more detailed derivation and analysis of DTBCs for the fourth order “Numerov-scheme” for the two dimensional Schrödinger equation will appear in §2 and in [ScAr07].

### 1.2 Finite difference scheme and discrete transparent boundary conditions for the two dimensional Schrödinger equation

In this section we shall briefly review the derivation of DTBCs for the two dimensional Schrödinger equation on a rectangular geometry in conjunction with a finite difference discretization. Here, we are ultimately interested in solving the Schrödinger equation on a geometry like in Figure 1.5 with both leads being rectangular and infinitely long. When discussing TBCs we only need to consider the geometry of the *exterior domain*, i.e. the domain to be eliminated by the TBCs. The *interior domain* shall be kept in the simulation and can have an irregular geometry (e.g. T-shaped like in Figure 1.5). For a more realistic model one should actually solve the nonlinear Schrödinger-Poisson equation in the interior domain (cf. §3 or [BeMePi05]), but this still does not effect the shape of the TBCs.

Here, we choose  $\Omega_{comp} = \mathbb{R} \times [0, Y] \subset \mathbb{R}^2$  as the domain of interest. Let  $\psi_{j,k}^n$  be the numerical approximation of the solution  $\psi(x_j, y_k, t_n)$  to the Schrödinger equation (1.1) on the equidistant grid  $\Omega_{\Delta x, \Delta y}$  with the nodes  $x_j = j\Delta x$ ,  $j \in \mathbb{Z}$ ;  $y_k = k\Delta y$ ,  $0 \leq k \leq K$  and the time discretization  $t_n = n\Delta t$ ,  $n \in \mathbb{N}_0$ . DTBCs shall be employed at  $x_0 = 0$  and  $x_J = J\Delta x = X$ , hence the computational domain is chosen as the rectangle  $[0, X] \times [0, Y]$ . At  $y_0 = 0$  and  $y_K = K\Delta y = Y$  we use zero Dirichlet boundary conditions.

Following [ArEhSo03] we shall now briefly review the derivation of DTBCs for the 2D Schrödinger equation. Using the five-point finite difference scheme in space and the Crank-Nicolson scheme in time, the discrete Schrödinger equation on  $\Omega_{\Delta x, \Delta y}$  reads

$$i\hbar D_t^+ \psi_{j,k}^n = -\frac{\hbar^2}{2m^*} \left( D_x^2 \psi_{j,k}^{n+\frac{1}{2}} + D_y^2 \psi_{j,k}^{n+\frac{1}{2}} \right) + V_{j,k}^{n+\frac{1}{2}} \psi_{j,k}^{n+\frac{1}{2}}. \quad (1.3)$$

Here,

$$D_t^+ \psi_{j,k}^n = \frac{\psi_{j,k}^{n+1} - \psi_{j,k}^n}{\Delta t},$$

$$D_x^2 \psi_{j,k}^n = \frac{\psi_{j-1,k}^n - 2\psi_{j,k}^n + \psi_{j+1,k}^n}{\Delta x^2},$$

## 1.2 Finite difference scheme and DTBCs for the 2D Schrödinger equation

$$D_y^2 \psi_{j,k}^n = \frac{\psi_{j,k-1}^n - 2\psi_{j,k}^n + \psi_{j,k+1}^n}{\Delta y^2}$$

denote the standard finite difference operators,

$$\begin{aligned} V_j^{n+\frac{1}{2}} &:= V\left(x_j, t_{n+\frac{1}{2}}\right), \\ \psi_{j,k}^{n+\frac{1}{2}} &:= \frac{1}{2}(\psi_{j,k}^{n+1} + \psi_{j,k}^n) \end{aligned}$$

a time averaging.

**Remark 1.1** *The discretization scheme (1.3) is of second order both in time and space. Since the discrete  $\ell^2$ -norm is preserved under the evolution, i.e.*

$$D_t^+ \|\psi\|_2^2 := \Delta x \Delta y D_t^+ \sum_{j \in \mathbb{Z}, 0 \leq k \leq K} |\psi_{j,k}^n|^2 = 0$$

for all  $n \geq 0$  (cf. [ArEhSo03]), the scheme is unconditionally stable.

Like in the analytical case we assume that the potential is constant outside of the computational domain:  $V_{j,k}^n = V_0$  for  $j \leq 1$  and  $V_{j,k}^n = V_J$  for  $j \geq J - 1$ , and for all  $0 \leq k \leq K$  and  $n \geq 0$ . This implies that the transversal solution modes (i.e. orthogonal to the channel axis) are decoupled in the exterior domain. Hence, we shall now Fourier transform equation (1.3) with respect to the discrete sine-functions

$$\begin{aligned} \hat{\psi}_{j,m}^n &:= \frac{1}{K} \sum_{k=1}^{K-1} \psi_{j,k}^n \sin\left(\frac{\pi km}{K}\right), \quad m = 1, \dots, K-1, 0 \leq j \leq J, n \geq 0, \\ \hat{\psi}_{j,0}^n &= \hat{\psi}_{j,K}^n = 0, \quad 0 \leq j \leq J, n \geq 0. \end{aligned}$$

It can be easily shown that

$$-\frac{1}{2\Delta y^2} \left( \psi_{j,k-1}^n - 2\psi_{j,k}^n + \psi_{j,k+1}^n \right)_m \hat{=} \frac{1}{\Delta y^2} \left( 1 - \cos\left(\frac{\pi m}{K}\right) \right) \hat{\psi}_{j,m}^n$$

for  $1 \leq k, m \leq K-1$ ,  $j \in \mathbb{Z} \setminus [1, J-1]$ . Since the potential  $V_{j,k}^n$  is constant in the exterior domain, the solution modes  $\hat{\psi}_{j,m}^n$  are independent of each other and we obtain  $K-1$  one dimensional discrete Schrödinger equations

$$\frac{i\hbar}{\Delta t} \left( \hat{\psi}_{j,m}^{n+1} - \hat{\psi}_{j,m}^n \right) = -\frac{\hbar^2}{2m^* \Delta x^2} \left( \hat{\psi}_{j+1,m}^{n+\frac{1}{2}} - 2\hat{\psi}_{j,m}^{n+\frac{1}{2}} + \hat{\psi}_{j-1,m}^{n+\frac{1}{2}} \right) + \tilde{V}_{j,m} \hat{\psi}_{j,m}^{n+\frac{1}{2}} \quad (1.4)$$

with the modified potential

$$\tilde{V}_{j,m} := V_j + \frac{\hbar^2}{m^*} \left( \frac{1 - \cos\left(\frac{\pi m}{K}\right)}{\Delta y^2} \right), \quad j \in \mathbb{Z} \setminus [1, J-1], m = 1, \dots, K-1.$$

## 1 Transparent boundary conditions for quantum-waveguide simulations

---

Next we assume that the discrete initial function  $\psi_{j,k}^0$  is compactly supported in the grid  $[1, J-1] \times [1, K-1]$ . Performing the discrete  $\mathcal{Z}$ -transformation,

$$\mathcal{Z}\{\psi^n\} = \Psi(z) := \sum_{n=0}^{\infty} \psi^n z^{-n}, \quad z \in \mathbb{C}, |z| > 1,$$

of (1.4) on the exterior domain, we derive  $K-1$  second order difference equations

$$\Psi_{j+1,m}(z) + \left( iR \frac{z-1}{z+1} - 2 - w\tilde{V}_{j,m} \right) \Psi_{j,m}(z) + \Psi_{j-1,m}(z) = 0, \quad j \leq 0 \text{ or } j \geq J, \quad (1.5)$$

with  $R = -\frac{4\Delta x^2 m^*}{\hbar \Delta t}$  and  $w = \frac{2\Delta x^2 m^*}{\hbar^2}$ . For each fixed  $m$ , equation (1.5) has two fundamental solutions of exponential form  $\Psi_{j,m}(z) = \alpha_m(z)^j$ . Both for physical reasons and since the discrete solution stays in  $\ell^2(\mathbb{Z} \times [1, K-1])$ , each mode  $\Psi_{j,m}(z)$  has to decay for  $|j| \rightarrow \infty$ . This requirement selects a unique root  $\alpha_m(z)$  (with  $|\alpha_m(z)| > 1$  for  $j \leq 0$ , e.g.) and the  $\mathcal{Z}$ -transformed DTBCs hence read

$$\Psi_1(z) = \alpha_0(z)\Psi_0(z), \quad \Psi_{J-1}(z) = \alpha_J(z)\Psi_J(z). \quad (1.6)$$

**Theorem 1.1 (DTBCs for the 2D Schrödinger equation)** *Consider the two dimensional time-dependent Schrödinger equation, discretized with the five-point difference scheme in space and the Crank-Nicolson scheme in time. Then, the sine-transformed DTBCs at  $x_0 = 0$  and  $x_J = J\Delta x$  read respectively*

$$\hat{\psi}_{1,m}^n - s_{0,m}^{(0)} \hat{\psi}_{0,m}^n = \sum_{\nu=1}^{n-1} s_{0,m}^{(n-\nu)} \hat{\psi}_{0,m}^\nu - \hat{\psi}_{1,m}^{n-1}, \quad n \geq 1, \quad (1.7)$$

$$\hat{\psi}_{J-1,m}^n - s_{J,m}^{(0)} \hat{\psi}_{J,m}^n = \sum_{\nu=1}^{n-1} s_{J,m}^{(n-\nu)} \hat{\psi}_{J,m}^\nu - \hat{\psi}_{J-1,m}^{n-1}, \quad n \geq 1, \quad (1.8)$$

where the convolution coefficients  $s_{j,m}^{(n)}$  are given by (cf. [ArEhSo03]):

$$\begin{aligned} s_{j,m}^{(n)} &= \left[ 1 - i\frac{\rho}{2} + \frac{\sigma_{j,m}}{2} \right] \delta_{n,0} + \left[ 1 + i\frac{\rho}{2} + \frac{\sigma_{j,m}}{2} \right] \delta_{n,1} \\ &\quad + \alpha_{j,m} e^{-in\varphi_{j,m}} \frac{P_n(\mu_{j,m}) - P_{n-2}(\mu_{j,m})}{2n-1}, \quad \rho = -iR, \quad \sigma_{j,m} = w\tilde{V}_{j,m}, \\ \xi_{j,m} &= \sqrt{(\rho^2 + \sigma_{j,m}^2)(\rho^2 + (\sigma_{j,m} + 4)^2)}, \quad \mu_{j,m} = \frac{\rho^2 + 4\sigma_{j,m} + \sigma_{j,m}^2}{\xi_{j,m}}, \\ \varphi_{j,m} &= \arctan \left( \frac{2\rho(\sigma_{j,m} + 2)}{\rho^2 - 4\sigma_{j,m} - \sigma_{j,m}^2} \right), \quad \alpha_{j,m} = \frac{i}{2} \sqrt{\xi_{j,m}} e^{i\varphi_{j,m}/2} \end{aligned}$$

for  $j = 0, J$ ,  $m = 1, \dots, K-1$ .  $P_n$  denotes the Legendre polynomials ( $P_{-1} \equiv P_{-2} \equiv 0$ ) and  $\delta_{n,\nu}$  is the Kronecker symbol.

## 1.2 Finite difference scheme and DTBCs for the 2D Schrödinger equation

**Remark 1.2** *The decay rate of the convolution coefficients coincides with the decay  $\mathcal{O}(t^{-3/2})$  of the convolution kernel in the analytical TBC (1.2).*

**Remark 1.3** *The discrete Schrödinger equation (1.3) and the DTBCs (1.7), (1.8) are solved iteratively in time. The convolution length in (1.7), (1.8) therefore grows with every time step. This makes it impossible to simplify (or accelerate) the numerical evaluation of these time convolutions by using a fast Fourier transform (FFT). Hence, the evaluation of the convolution sum up to time level  $n$  requires a memory of the order  $\mathcal{O}(Kn)$  and numerical costs of the order  $\mathcal{O}(Kn^2)$ . The latter can easily surpass the costs of solving the PDE in the interior domain which only grows linearly in  $n$ . As a remedy it is possible to approximate the convolution coefficients by a sum of exponentials (say  $L$  terms) and to calculate the convolution sum recursively, as shown in [ArEhSo03]. We write*

$$s_{j,m}^{(n)} \approx \tilde{s}_{j,m}^{(n)} = \begin{cases} s_{j,m}^{(n)} & : n = 0, \dots, r-1 \\ \sum_{l=1}^L b_{j,m,l} q_{j,m,l}^{-1} & : n = r, r+1, \dots \end{cases} \quad (1.9)$$

for some parameters  $L, r \in \mathbb{N}$ . Typical values to obtain good results are  $L = 10$  or  $20$ ,  $r = 1, 2$ . Furthermore, the non-local part

$$C^n(\widehat{\psi}_{j,m}) := \sum_{k=0}^{n-r} \tilde{s}_{0,m}^{(n-k)} \widehat{\psi}_{j,m}^k$$

of the approximated DTBCs can be evaluated efficiently by the sum

$$C^n(\widehat{\psi}_{j,m}) = \sum_{l=1}^L c_l^n(\widehat{\psi}_{j,m}) \quad (1.10)$$

and the recursion

$$\begin{aligned} c_l^n(\widehat{\psi}_{j,m}) &= q_{j,m,l}^{-1} c_l^{n-1}(\widehat{\psi}_{j,m}) + b_{j,m,l} q_{j,m,l}^{-r} \widehat{\psi}_{j,m}^{n-r}, \quad n = r+1, r+2, \dots, \\ c_l^r(\widehat{\psi}_{j,m}) &= 0. \end{aligned}$$

This way, the numerical costs may be reduced to  $\mathcal{O}(KLn)$  and the memory to  $\mathcal{O}(KL)$  with  $L \ll n$ , while still keeping high accuracy (cf. [ArEhSo03]). A numerical example concerning the approximated DTBCs will be given in the following section.

**Remark 1.4** *In (1.7), (1.8) the DTBCs are formulated in sine-transformed space. Hence, these DTBCs are also non-local in space – more precisely in the tangential*

## 1 Transparent boundary conditions for quantum-waveguide simulations

---

manifold of the artificial boundary. Due to the sine-modes in  $y$ -direction, this non-locality can easily be dealt with using FFT (cf. §1.3.1). If the exterior potential is not constant in the transversal direction (of the channel), the solution can still be expanded in the eigenfunctions of the transversal Schrödinger operator (cf. §3 or [BeMePi05]). But then FFTs cannot be used for the evaluation of the DTBCs (cf. §3).

**Remark 1.5** *The numerical costs of implementing the DTBCs (1.7), (1.8) agree with the costs for “ad-hoc” discretizations of the analytical TBC (1.2) (or its 2D-analogue) that were proposed in the literature. But (1.7), (1.8) have the advantage not to introduce any numerical reflections or to destroy the unconditional stability of the underlying PDE scheme.*

**Remark 1.6** *The Crank-Nicolson finite difference scheme (1.3) is of the order  $\mathcal{O}(\Delta x^2 + \Delta y^2 + \Delta t^2)$ . With a higher order scheme (compact finite differences) one can again derive modified DTBCs and obtain an order of convergence of  $\mathcal{O}(\Delta x^4 + \Delta y^4 + \Delta t^2)$  (cf. §2 or [ScAr07]).*

### 1.3 Numerical results

In this section we discuss the practical implementation of DTBCs and ABCs and compare the results obtained with DTBCs, approximated DTBCs and ABCs for travelling Gaussian waves. Furthermore, we present some numerical results when using DTBCs for simulating quantum waveguides.

#### 1.3.1 Implementation of DTBCs

In (1.7), (1.8) the DTBCs are written in sine-transformed space. A direct implementation in position space would necessitate tremendous numerical costs, hence they are implemented in  $y$ -Fourier space. The discrete convolution

$$\hat{C}_{J,m}^{(n-1)} := \frac{1}{K} \sum_{\nu=1}^{n-1} s_{J,m}^{(n-\nu)} \hat{\psi}_{J,m}^{\nu}, \quad m = 1, \dots, K-1 \quad (1.11)$$

for the right boundary  $x_J = J\Delta x$  is calculated in Fourier space and inverse transformed by

$$C_{J,k}^{(n-1)} = 2 \sum_{m=1}^{K-1} \sin\left(\frac{\pi mk}{K}\right) \left( \sum_{\nu=0}^{n-1} s_{J,m}^{(n-\nu)} \hat{\psi}_{J,m}^{\nu} \right), \quad k = 1, \dots, K-1.$$

Since the convolution (1.11) only involves the solution at the boundary at past time levels (i.e. for  $\nu \leq n-1$ ), one can directly store the sine-transformed boundary

data  $\hat{\psi}_{J,m}^\nu$ . Moreover, this part of the DTBCs only enters the inhomogeneity of the linear system to be solved at each time level.

The part  $s_{J,m}^{(0)}\hat{\psi}_{J,m}^n$  of the left hand side of the DTBCs (1.8) has to be inverse transformed to physical space and we get the couplings

$$\begin{aligned} \left(s_{J,m}^{(0)}\hat{\psi}_{J,m}^n\right)_{J,k,l}^\vee &= 2 \sum_{m=1}^{K-1} \sin\left(\frac{\pi mk}{K}\right) s_{J,m}^{(0)}\hat{\psi}_{J,m}^n \\ &= \frac{2}{K} \sum_{m=1}^{K-1} \sum_{l=1}^{K-1} s_{J,m}^{(0)} \sin\left(\frac{\pi mk}{K}\right) \sin\left(\frac{\pi kl}{K}\right) \psi_{J,l}^n \end{aligned}$$

for  $k, l = 1, \dots, K - 1$ . Hence, the 5-diagonal system of the discrete 2D Schrödinger equation (1.3) obtains additional entries due to the DTBCs.

In order to model the electron influx from the left lead, we shall prescribe an incoming plane wave  $\varphi(x, y, t)$  at the left boundary. Hence, inhomogeneous DTBCs have to be used at  $x_0 = 0$ :

$$\begin{aligned} \hat{\psi}_{1,m}^n - \hat{\varphi}_{1,m}^n - s_{0,m}^{(0)} \left( \hat{\psi}_{0,m}^n - \hat{\varphi}_{0,m}^n \right) \\ = \sum_{\nu=1}^{n-1} s_{0,m}^{(n-\nu)} \left( \hat{\psi}_{0,m}^\nu - \hat{\varphi}_{0,m}^\nu \right) - \left( \hat{\psi}_{1,m}^{n-1} - \hat{\varphi}_{1,m}^{n-1} \right), \quad n \geq 1, \quad (1.12) \end{aligned}$$

with the discrete, sine-transformed incoming wave  $\varphi_{j,k}^n$ ,  $0 \leq k \leq K, 0 \leq j \leq J$ . These boundary conditions are implemented analogously to the DTBCs at  $x_j = X$ .

### 1.3.2 Implementation of ABCs

It is also possible to simulate open quantum systems with ABCs, like it has been done in [Bu97]. Since the Crank-Nicolson finite difference scheme is also used for the discretization of the time-dependent Schrödinger equation in [Bu97] it is easy to compare our results based on DTBCs with ones received using the ABCs there. The ABCs in [Bu97] are based on the enlargement of the computational domain  $\Omega_{comp} = (X_0, X) \times (0, Y)$  to  $\Omega_{ABC} = (X_0, X_d) \times (0, Y)$  with  $X_d > X$ . A constant complex-valued penalty potential  $V(x, y) = W - iA$  is introduced for  $(x, y) \in (X, X_d) \times (0, Y)$ . A schematic view of the enlarged computational domain  $\Omega_{ABC}$  is presented in Figure 1.1.

For the derivation of ABCs we consider the one dimensional Schrödinger equation (1.1) on the enlarged computational domain  $(X_0, X_d)$ . At  $x = X_d$  we assume zero Dirichlet boundary conditions, ABCs will be derived at  $x = X < X_d$ . In the

## 1 Transparent boundary conditions for quantum-waveguide simulations

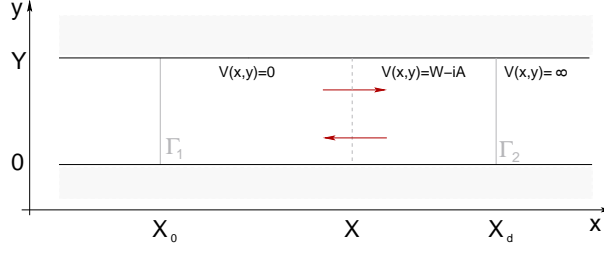


Figure 1.1: Enlarged computational domain  $\Omega_{ABC} = (X_0, X_d) \times (0, Y)$  for the usage of ABCs. At  $X_d$  we assume zero Dirichlet boundary conditions.  $X$  denotes the artificial boundary, where we introduce ABCs.

zones  $(X_0, X)$  and  $(X, X_d)$  the solutions  $\psi(x)$  to the 1D stationary Schrödinger equation read

$$\begin{aligned} \psi(x) &= B e^{ikx} + C e^{-ikx}, & x \leq X, \\ \psi(x) &= b e^{ik_1 x} + c e^{-ik_1 x}, & X_0 \leq x \leq X, \\ \psi(x) &= 0, & x \geq X_d \end{aligned}$$

with transmission coefficients  $0 \leq B, b \leq 1$ , reflexion coefficients  $0 \leq C, c \leq 1$  and wave numbers

$$\begin{aligned} k^2 &= \frac{2m_* E}{\hbar^2}, \\ k_1^2 &= k^2 + \frac{2m_*}{\hbar^2} (iA - W) \end{aligned} \quad (1.13)$$

obtained by the continuous dispersion relation.  $E$  denotes the given energy. The ABCs follow by the assumption that  $\psi(x)$  and the first derivative  $\psi'(x)$  are continuous at  $x = X$  and setting the reflection coefficient  $C = 0$ . For parameters  $X = 0$  and  $X_d = d$  we calculate

$$C = \frac{b}{2} \left[ 1 - \frac{k_1}{k} - \left( 1 + \frac{k_1}{k} \right) e^{2ik_1 d} \right],$$

and the condition  $C = 0$  leads to the nonlinear coupled equations

$$\begin{aligned} \alpha &= k \frac{\sinh(\beta d) \cosh(\beta d)}{\cos^2(\alpha d) \cosh^2(\beta d) + \sin^2(\alpha d) \sinh^2(\beta d)}, \\ \beta &= -k \frac{\sin(\alpha d) \cos(\alpha d)}{\cos^2(\alpha d) \cosh^2(\beta d) + \sin^2(\alpha d) \sinh^2(\beta d)} \end{aligned} \quad (1.14)$$

for  $k_1 = \alpha + i\beta$ . Numerically, the system (1.14) may be solved by an iterative Newton method. From (1.13) follows by comparison of coefficients

$$A = \frac{\hbar^2}{m_*} \alpha \beta,$$

$$W = \frac{(k^2 - \alpha^2 + \beta^2)\hbar^2}{2m_*}$$

for  $V(x) = W - iA$ ,  $x \in (0, d)$ .

ABCs of this type only work well for travelling waves which pass the artificial boundary  $x = X$  in an orthogonal angle. In this case the penalty potential is calculated for the mono-energetic wave function.

### 1.3.3 Example 1: Travelling Gaussian waves

First we will show some rather mathematical examples of travelling Gaussian waves on the two dimensional domain  $\Omega = \mathbb{R} \times (0, 1)$ . Therefore we choose the  $y$ -periodic initial function

$$\psi^I(x, y) = \sum_{\ell \in \mathbb{Z}} (-1)^\ell e^{-\frac{\alpha}{2} \left[ \left(x - \frac{3}{4}\right)^2 + \left(y - \frac{1}{4} + \ell\right)^2 \right] + ik_x x + ik_y y}, \quad (x, y) \in \Omega \quad (1.15)$$

with given wavenumbers  $k_x = k_y = 100$  and  $\alpha = 240$ . Let the computational domain be  $\Omega_{comp} = (0, 1) \times (0, 1)$ . Exact DTBCs according to (1.7), (1.8) are implemented at  $x = 0$ ,  $x = 1$ . We consider the discretization parameters  $\Delta x = \Delta y = 1/120$ ,  $\Delta t = 2 \cdot 10^{-5}$ . In Figure 1.2(a) we show the absolute value of the initial function (1.15). The evolution of this initial function according to the scaled Schrödinger equation ((1.3) with  $\hbar = m_* = 1$ ) is presented in Figure 1.2 (b), (c) for some times  $t_n$ . The Gaussian beam leaves the computational domain through the artificial boundary  $x = 1$  without being reflected back.

For the same discretization we calculate the solution to the Schrödinger equation ((1.3) again with  $\hbar = m_* = 1$ ) with the initial data (1.15) along with approximated DTBCs (1.9) using the parameter  $r = 2$ . The results for the time step  $t_n = 240\Delta t$  are presented in Figure 1.3 for the value  $L = 5$  (Fig. 1.3(a)) and the value  $L = 10$  (Fig. 1.3(b)). For  $L = 5$  there are some unphysical reflections at the artificial boundary which are significantly reduced for  $L = 10$ .

In a third calculation we again assume the initial function (1.15) and compute the solution  $\psi$  to the Schrödinger equation ((1.3) with  $\hbar = m_* = 1$ ) with DTBCs at  $x = 0$  and ABCs (c.f. §1.3.2) at  $x = 1$ . We use the same discretization parameters as before and let  $X_d = 2$ . Hence, the computational domain is chosen twice big as the domain of interest, which is used for the calculation with the DTBCs. The absolute value of the solution  $\psi$  is plotted on the domain of interest  $(0, 1) \times (0, 1)$  in Figure 1.4 for some time steps  $t_n$ . Since the wave function crosses the artificial boundary in a non-orthogonal angle, there are some unphysical reflections at the artificial boundary.

# 1 Transparent boundary conditions for quantum-waveguide simulations

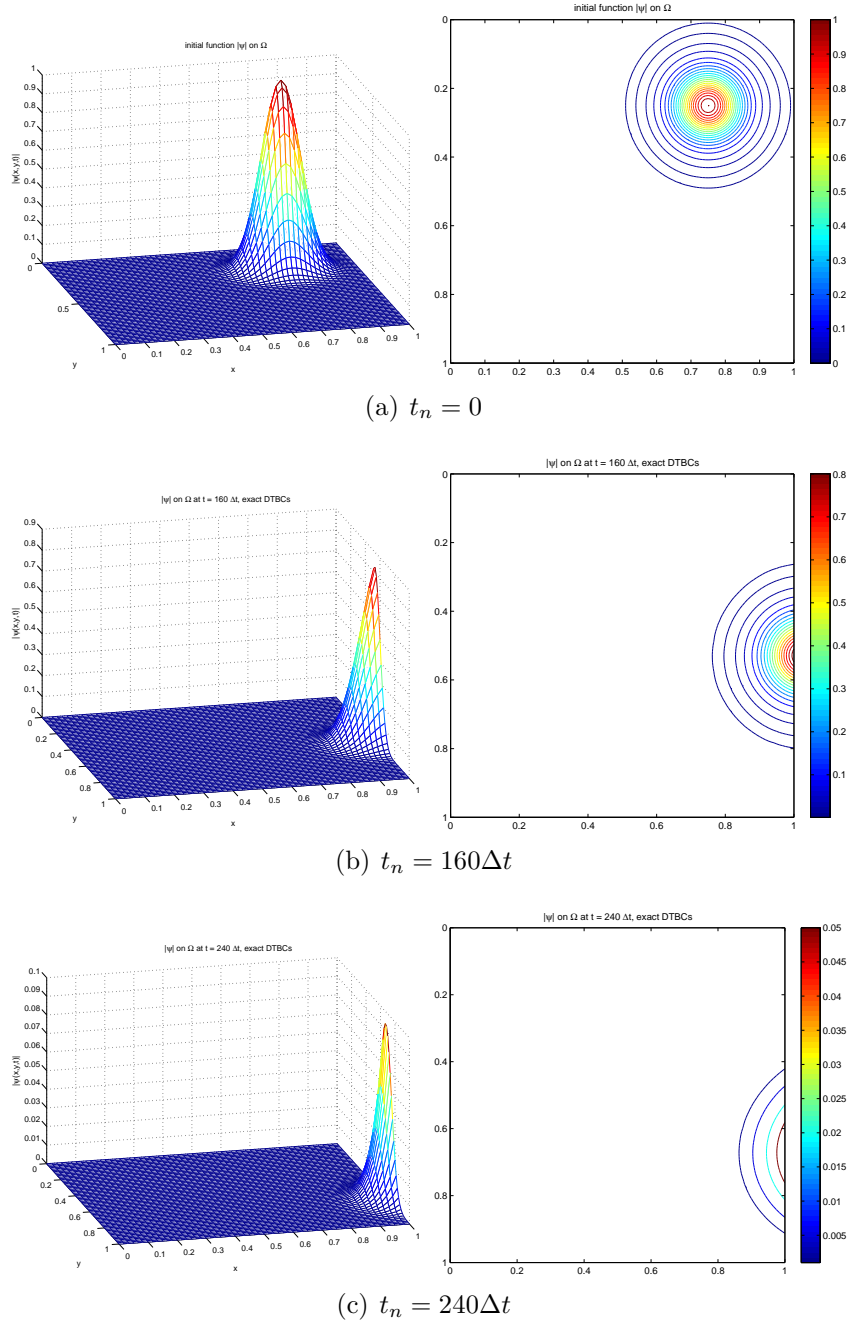
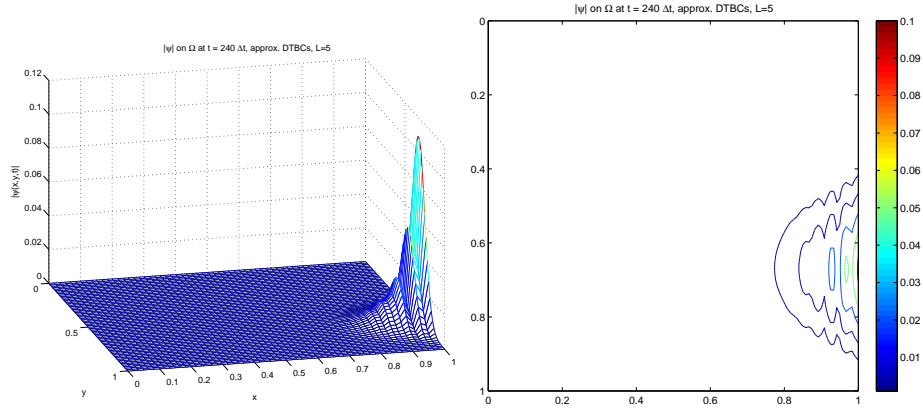
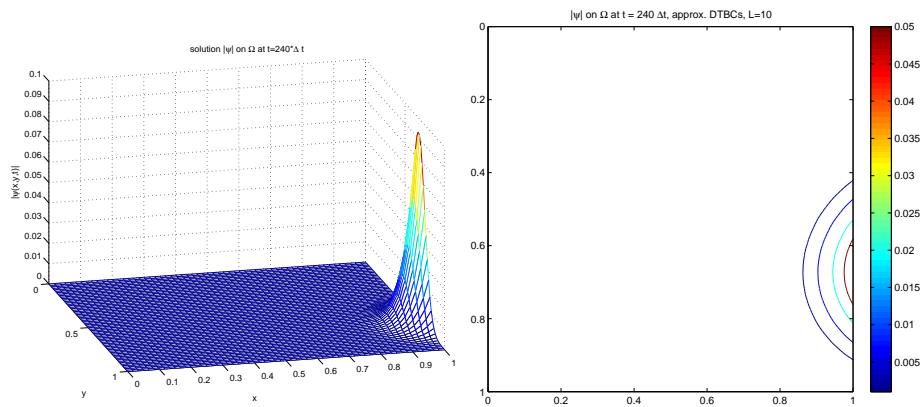


Figure 1.2: Absolute value of the initial function (1.15) and the absolute value of the solution to the Schrödinger equation at some time steps  $t_n$  calculated with exact DTBCs at  $x = 0$  and  $x = 1$ . We choose the discretization parameters  $\Delta x = \Delta y = 1/120$  and  $\Delta t = 2 \cdot 10^{-5}$ . On the right hand side we plotted the same values as on the left hand side but as contour plots.



(a)  $L = 5$



(b)  $L = 10$

Figure 1.3: Absolute value the solution to the Schrödinger equation at the time step  $t_n = 240\Delta t$  calculated with exact DTBCs at  $x = 0$  and approximated DTBCs at  $x = 1$  with (a):  $L = 5$  and (b):  $L = 10$  terms in the sum of exponentials. On the right hand side we plotted the same values as on the left hand side but as contour plots.

# 1 Transparent boundary conditions for quantum-waveguide simulations

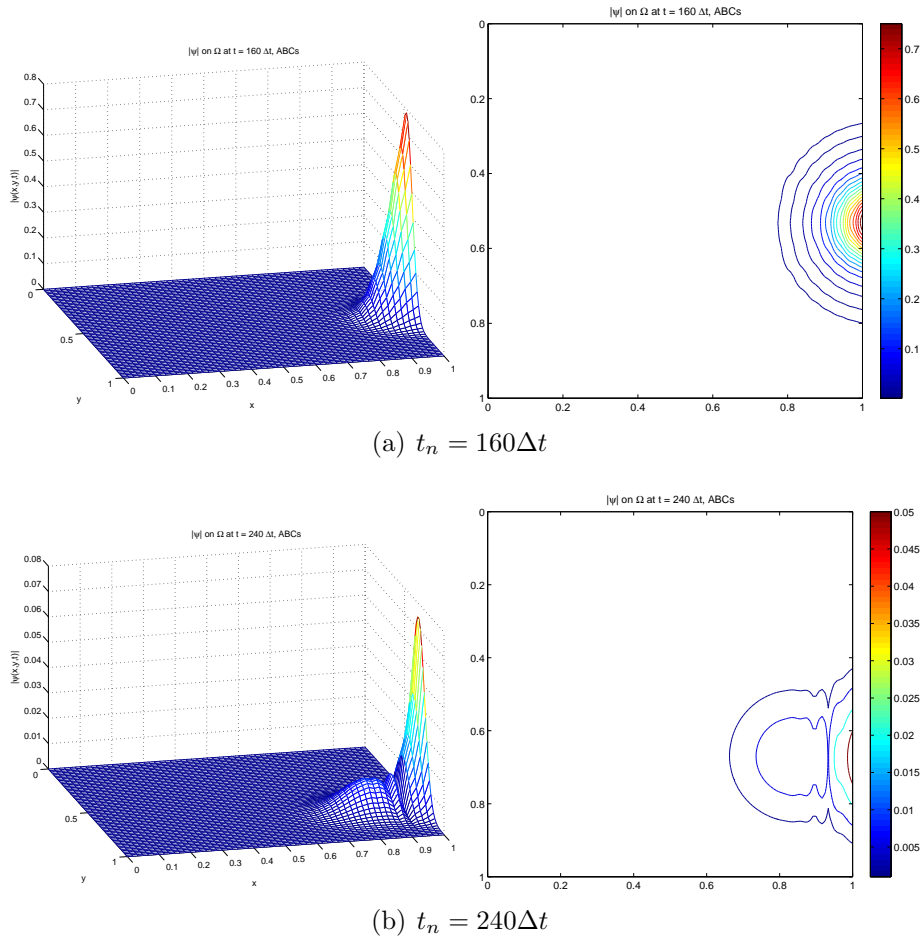


Figure 1.4: Absolute value the solution to the Schrödinger equation at some time steps calculated with DTBCs at  $x = 0$  and ABCs at  $x = 1$ . The enlarged computational domains equals  $\Omega_{comp} = (0, X_d) \times (0, Y) = (0, 2) \times (0, 1)$ . On the right hand side we plotted the same values as on the left hand side but as contour plots. The solutions are plotted on the domain of interest  $(0, 1) \times (0, 1)$ .

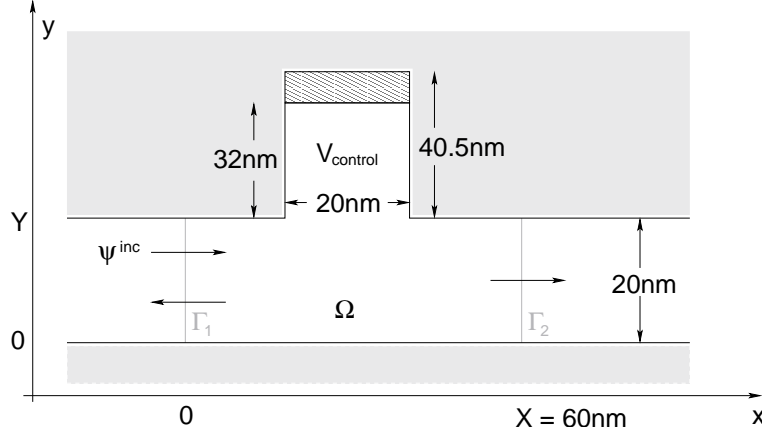


Figure 1.5: T-shaped structure  $\Omega$  with length  $X = 60\text{nm}$ , a channel width  $Y = 20\text{nm}$ , and a stub width  $w = 20\text{nm}$ . It is possible to switch the stub length from  $32\text{nm}$  to  $40.5\text{nm}$ . Inhomogeneous DTBCs are implemented at  $x = 0$  and homogeneous DTBCs at  $x = X$ . The inflow is modeled by the function  $\varphi$  given in equation (1.16).

### 1.3.4 Example 2: Simulation of quantum waveguides

Following the simulation of a GaAs-waveguide in [Bu97], we choose the T-shaped geometry shown in Figure 1.5 to simulate a quantum waveguide transistor. In  $x$ -direction the channel has a length of  $X = 60\text{nm}$ ; the channel width  $Y$  and the stub width  $w$  are  $20\text{nm}$ . In order to control the current through the channel, the stub length can be changed from  $L_1 = 32\text{nm}$  to  $L_2 = 40.5\text{nm}$ . Homogeneous DTBCs (1.7) are implemented at  $x = X$ , and inhomogeneous DTBCs (1.12) at  $x = 0$ . All other boundaries are considered as hard walls, i.e. we use homogeneous Dirichlet boundary conditions for  $\psi$ . A (discrete) time harmonic incoming wave function

$$\varphi_{j,k}^n = \sin\left(\frac{\pi k}{K}\right) e^{ik_x j \Delta x} e^{-\frac{iEn\Delta t}{\hbar}}, \quad k = 0, \dots, K, n \in \mathbb{N}_0 \quad (1.16)$$

is modeling the mono-energetic constant incoming current at  $x = 0$ . Here,  $\varphi$  includes only the lowest transversal mode. But any linear combination of higher modes would work equally well, which is a great advantage compared to other artificial boundary conditions (e.g. [Bu97]). In our example the energy  $E$  of the incoming wave equals  $29.9\text{meV}$  and the effective electron mass has the value  $m^* = 0.067m_0$ , which corresponds to GaAs. The value of  $k_x$  can be derived from the discrete dispersion relation

$$E = \frac{\hbar^2}{m^*} \left( \frac{1 - \cos(\Delta x k_x)}{\Delta x^2} \right) + \frac{\hbar^2}{m^*} \left( \frac{1 - \cos\left(\frac{\pi \Delta y}{K}\right)}{\Delta y^2} \right)$$

## 1 Transparent boundary conditions for quantum-waveguide simulations

---

of the Schrödinger equation with  $V_0 = 0$  for an incoming wave (1.16).

For the subsequent simulation we solve the Schrödinger equation (1.1) by the difference equation (1.3) without external potential, i.e.  $V = 0$ . For realistic simulations of MOSFET-channels, (1.1) should be coupled to the self-consistent Coulomb potential inside the channel. Since we focus on DTBCs, we shall not include this here. But a coupling to the Poisson equation *inside* the computational domain does *not* change the derivation or discretization of our open boundary conditions (cf. §3 for more details concerning the Schrödinger-Poisson system). Since we are mostly interested in the switching and the large time behavior of this waveguide, we choose the following (somewhat arbitrary) initial function

$$\psi^I(x, y) = \begin{cases} \sin\left(\frac{y\pi}{Y}\right) e^{ik_x x} & : 0 \leq x < x_1 \\ \frac{1}{2} \sin\left(\frac{y\pi}{Y}\right) e^{ik_x x} \left[1 + \cos\left(\pi \frac{x-x_1}{x_2-x_1}\right)\right] & : x_1 \leq x < x_2 \\ 0 & : x \geq x_2 \end{cases}$$

with  $x_1 = 25\text{nm}$  and  $x_2 = 38\text{nm}$ , which is consistent with the incoming wave.

Figure 1.6 shows the absolute value of the temporal evolution of the numerical solution  $\psi$ . In this simulation the stub length is first fixed to  $L_1 = 32\text{nm}$ . After 1.68ps the solution reaches (essentially) a steady state (*off-state* of the waveguide). Phenomenologically speaking, in this case only  $1\frac{1}{2}$  wave packets “fit” into the stub (cf. Fig. 1.6(c)). Hence, they block the current flow through the waveguide. Then, at  $t = 1.68\text{ps}$  the stub is enlarged at once to  $L_2 = 40.5\text{nm}$ . After some transient phase, the solution converges to a new steady state (*on-state* of the waveguide, cf. Fig. 1.6(f)). Here, two wave packets “fit” into the stub, and the current can flow almost unblocked through the device. At  $t = 3.60\text{ps}$  the current is already almost constant in  $x$  and at its maximum level.

### 1.3 Numerical results

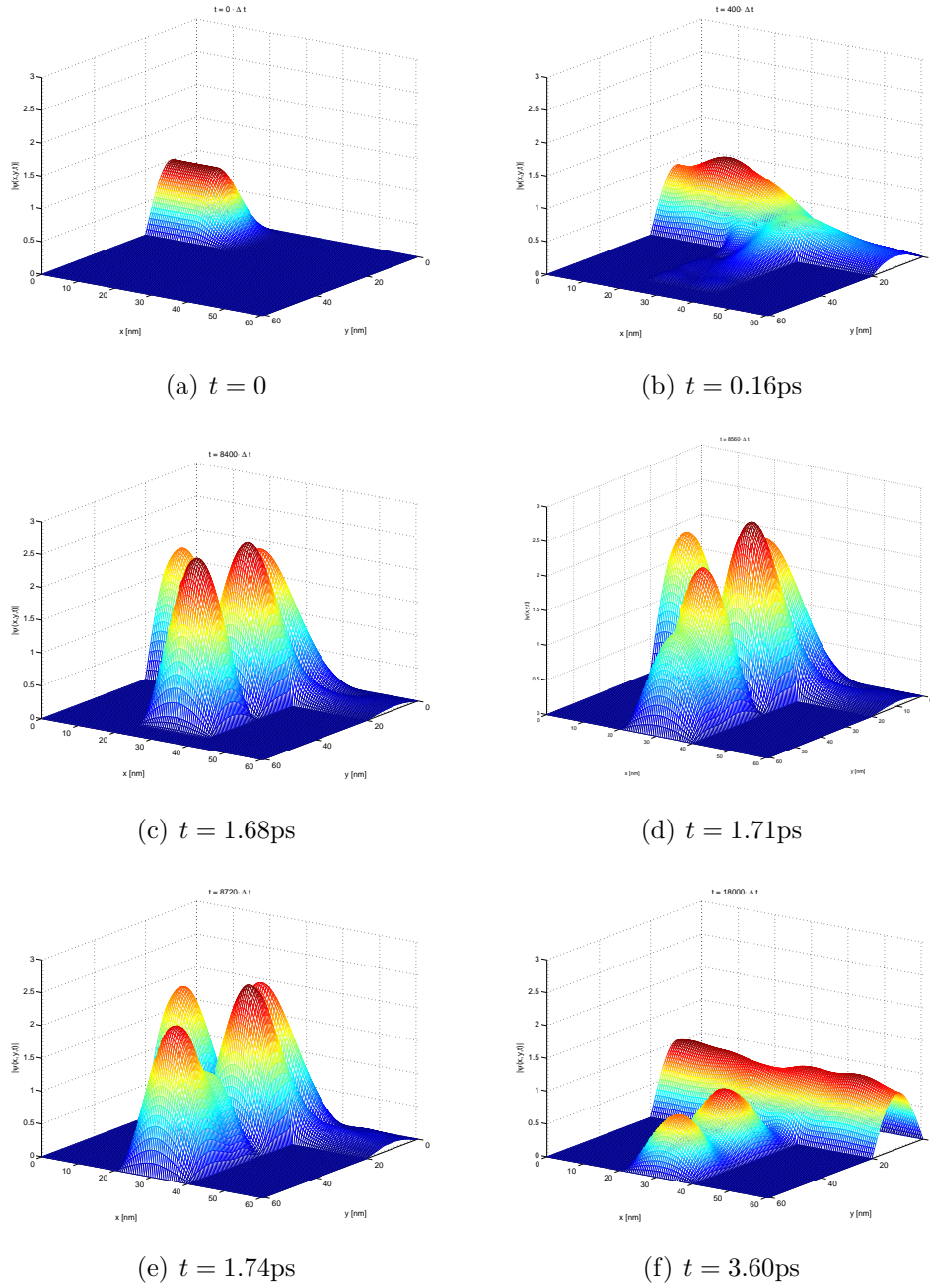


Figure 1.6: Absolute value of the numerical solution  $\psi$  to the time-dependent Schrödinger equation on the T-shaped structure of Figure 1.5. The discretization parameters are chosen as  $\Delta x = \Delta y = 0.5\text{nm}$ ,  $\Delta t = 0.0002\text{ps}$ ,  $V = 0\text{meV}$ ,  $m^* = 0.067m_0$ ,  $E = 29.9\text{meV}$ .

# Bibliography

- [AABES07] X. Antoine, A. Arnold, C. Besse, M. Ehrhardt and A. Schädle: *A Review of Transparent and Artificial Boundary Conditions Techniques for Linear and Nonlinear Schrödinger Equations*, submitted to Appl. Num. Mathem. (2007)
- [Ar98] A. Arnold: *Numerically Absorbing Boundary Conditions for Quantum Evolution Equations*, VLSI Design **6** (1998) 313–319
- [ArEhSo03] A. Arnold, M. Ehrhardt and I. Sofronov: *Approximation, stability and fast calculation of non-local boundary conditions for the Schrödinger equation*, Comm. Math. Sc. **1** (2003) 501–556
- [BaPo91] V.A. Basakov and A.V. Popov: *Implementation of transparent boundaries for numerical solution of the Schrödinger equation*, Wave Motion **14** (1991) 123–128
- [BeMePi05] N. Ben Abdallah, F. Méhats and O. Pinaud: *On an open transient Schrödinger-Poisson system*, Math. Models Methods Appl. Sci. **15**, no. 5 (2005) 667–688
- [Bu97] L. Burgnies: *Mécanismes de conduction en régime ballistique dans les dispositifs électroniques quantiques*, Ph. D. thesis, Université des Sciences et Technologies de Lille (1997)
- [EhAr01] M. Ehrhardt and A. Arnold: *Discrete Transparent Boundary Conditions for the Schrödinger Equation*, Rivista di Matematica della Università di Parma **6** (2001) 57–108
- [Pa82] J.S. Papadakis: *Impedance formulation of the bottom boundary condition for the parabolic equation model in underwater acoustics*, NORDA Parabolic Equation Workshop, NORDA Tech. Note **143** (1982)
- [ScAr07] M. Schulte and A. Arnold: *Discrete transparent boundary conditions for the Schrödinger equation – a compact higher order scheme*, to appear in Kinetic and related models **1** (2008)

# 2 Discrete transparent boundary conditions for the Schrödinger equation – a higher compact order scheme

In this chapter we consider the two dimensional time-dependent Schrödinger equation with the new compact nine-point scheme in space and the Crank-Nicolson difference scheme in time. For the resulting difference equation we derive discrete transparent boundary conditions in order to get highly accurate solutions for open boundary problems. Numerical experiments illustrate the perfect absorption of outgoing waves independently of their impact angle at the boundary. Finally, we apply inhomogeneous discrete transparent boundary conditions to the transient simulation of quantum waveguides.

## 2.1 Introduction

The development of novel semiconductor devices (like diodes or transistors) is usually supported by computer simulations to optimize the desired operating features. Schrödinger models describe the purely ballistic transport of electrons and holes, and they are employed e.g. for simulations of quantum waveguides and nano-scale semiconductor heterostructures. The time-dependent two dimensional Schrödinger equation describes the time evolution of the complex-valued wave function  $\psi$ . It reads

$$\begin{aligned} i\frac{\partial}{\partial t}\psi(x, y, t) &= -\frac{1}{2}\Delta\psi(x, y, t) + V(x, y, t)\psi(x, y, t), \quad (x, y) \in \Omega \subset \mathbb{R}^2, t > 0 \\ \psi(x, y, 0) &= \psi^I(x, y) \in L^2(\Omega) \end{aligned} \tag{2.1}$$

with the real-valued given potential  $V(x, y, t)$ .

As in [ArEhSo03], we assume that  $\Omega$  is an infinitely long stripe, i.e.  $\Omega = \mathbb{R} \times (0, Y)$ , with  $\psi$  satisfying homogeneous Dirichlet boundary conditions at  $y = 0$  and  $y = Y$ . For computational purposes it is necessary to reduce the simulations to some finite subdomain, say  $\Omega_{comp} := (0, X) \times (0, Y) \subset \Omega$  by introducing (artificial) open boundary conditions at  $x = 0$  and  $x = X$ . As it is common practice, we

## 2 DTBCs for the Schrödinger equation – a higher compact order scheme

---

assume  $\text{supp } \psi^I \subset \Omega_{\text{comp}}$ , and that the potential is constant in the two exterior domains  $\mathbb{R}^- \times (0, Y)$  and  $(X, \infty) \times (0, Y)$ . Note that an only time-dependent exterior potential can be dealt with by the transformation  $\psi(x, t) = \varphi(x, t) \exp \left[ \int_0^t V(\tau) d\tau \right]$  (cf. §3).

Open boundary conditions are called *transparent*, if they yield identical solutions both on the original large domain  $\Omega$  and the reduced domain  $\Omega_{\text{comp}}$ . In the 1D case the transparent boundary condition (TBC) takes the form

$$\frac{\partial}{\partial \eta} \psi = -\sqrt{2} e^{-i\pi/4} e^{-iV_{\text{ext}}t} \sqrt{\partial_t} (e^{iV_{\text{ext}}t} \psi), \quad x = 0 \text{ or } x = X, \quad (2.2)$$

where  $\eta$  denotes the unit outward normal vector at each interface and  $V_{\text{ext}}$  is the constant exterior potential.  $\sqrt{\partial_t}$  is the fractional time derivative of order  $\frac{1}{2}$  with the Fourier symbol  $\sqrt{-i\omega}$ , and it can be rewritten as a time-convolution of the boundary data

$$(\sqrt{\partial_t} \psi)(x, t) = \frac{1}{\sqrt{\pi}} \frac{d}{dt} \int_0^t \frac{\psi(x, \tau)}{\sqrt{t-\tau}} d\tau. \quad (2.3)$$

When carrying out the  $t$ -derivative, one sees that the resulting kernel behaves like  $\mathcal{O}(t^{-3/2})$  for  $t \rightarrow \infty$ . The one dimensional TBC (2.2) has been derived by several authors, e.g. in [Pa82], [BaPo91]. Its extension to rectangular geometries in 2D is based on taking the partial Fourier series of  $\psi$  w.r.t.  $y$ :

$$\psi(x, y, t) = \sum_{m \in \mathbb{N}} \hat{\psi}_m(x, t) \sin \left( \frac{m\pi y}{Y} \right).$$

Since  $V$  is constant in each of the two exterior domains, the time evolution of the modes  $\hat{\psi}_m(x, t)$ ,  $m \in \mathbb{N}$  is decoupled there. Hence, each mode satisfies at  $x = 0$  and  $x = X$  a one dimensional TBC

$$\frac{\partial}{\partial \eta} \hat{\psi}_m(x, t) = -\sqrt{2} e^{-i\pi/4} e^{-iV_m t} \sqrt{\partial_t} \left( e^{iV_m t} \hat{\psi}_m(x, t) \right), \quad m \in \mathbb{N}, \quad (2.4)$$

with the potentials  $V_m := V_{\text{ext}} + \frac{1}{2} \left( \frac{m\pi}{Y} \right)^2$ .

The goal of this chapter is to derive and analyze a discrete analogue of (2.4) in conjunction with a fourth order finite difference scheme of the Schrödinger equation. Discretizations of TBCs are delicate even in the 1D case, as they may lead to unphysical reflections at the boundaries (cf. [Ma89], [BaPo91], [Sc02]). Here we shall follow the “philosophy” of [Ar98], [EhAr01], [ArEhSo03] and derive *discrete transparent boundary conditions* (DTBCs), instead of discretizing the analytic TBC (2.4). We shall now first review several popular discretization schemes

for the Schrödinger equation as well as existing strategies for treating absorbing boundary conditions (ABCs) for it. An ABC is a *local* approximation to the exact, but *nonlocal* TBC (2.2).

A popular spatial discretization of the Schrödinger equation is based on the second order finite difference scheme. Together with a Crank-Nicolson scheme in time, this yields an unconditionally stable scheme (cf. §1 or [EhAr01]). In many applications compact higher order finite difference schemes are used (e.g. the fourth order *Numerov scheme*, cf. [KaMoSi05], [Mo04]). And this will be the starting point for this chapter. Another approach is given in [BaShMa02], where a time-splitting spectral approximation is developed for the Schrödinger equation. This strategy is very efficient for smooth solutions, but it has no advantage for heterostructures (with discontinuous potentials), since the potential is assumed to be periodic in space and  $C^\infty(\mathbb{R})$  in [BaShMa02]. In [BoDe06] Borzi and Decker combined a pseudospectral method for the space discretization with a leap-frog time-propagation scheme, which is second order accurate in time and yields spectral accuracy in space.

The simplest possibility to implement ABCs for Schrödinger-type equations is to enlarge the computational domain and to add some complex-valued potential just outside the domain of interest in order to damp the solution there. This approach was first presented in [KoKo86], [NeBa89] and is also often used in physical applications (e. g. [Bu97], [HePfSt07]). However, like seen in §1, it only works well for one tunable wavenumber of the wave function  $\psi$ . Pseudodifferential techniques, like in the seminal works of Engquist and Majda in [EnMa77], [EnMa79] for the wave equation have been used by Shibata [Sh91] and Kuska [Ku92]. Since their analytical approaches lead to non-local (in time) boundary conditions (cf. (2.2)), they used approximations of the square root symbol by low order rational functions. In [FeJi99] Fevens and Jiang derived ABCs for the Schrödinger equation which depend on the group velocity of the travelling wave package. Only the parts with a positive velocity are admitted to pass the right boundary. But the discretization of these ABCs leads to weakly ill-posed problems, as shown in [AlRe02]. Furthermore, one has to know the (main) velocity of the solution a-priori. So, these ABCs are not practical either. In [AlRe04] Alonso-Mallo and Reguera calculated ABCs for the semidiscrete Schrödinger equation in space, the fully discrete model is described in [AlRe03]. Both approaches are weakly unstable and show increasing instabilities for higher order ABCs. In [AnBe01] Antoine and Besse derived ABCs on a curved artificial boundary. Their well-posedness and discretization is studied in [AnBeMo04]. A generalization of the 2D-result of Antoine and Besse is formulated by Szeftel in [Sz04a] for both linear and non-linear Schrödinger equations in  $\mathbb{R}^d$ . Here, the author used also a pseudodifferential approach and obtained the boundary operator based on a reflection-of-singularities-

## 2 DTBCs for the Schrödinger equation – a higher compact order scheme

---

theory for the Schrödinger equation (cf. [Sz04b]). In order to get local ABCs both in space and time, he adapted the approximation strategy from [EnMa79]. The results are good for the linear case, but poor in the non-linear case. For a more detailed review of ABCs and TBCs we refer to [AABES07].

Exact DTBCs were developed in [ArEhSo03] for the five-point finite difference scheme (of second order) for (2.1), along with the Crank-Nicolson time discretization. But the numerical tests of [ArEhSo03] were only for the 1D case. In §1 and in [ArSc07] we presented some simulations concerning DTBCs for the 2D Schrödinger equation which is discretized with the standard five-point Crank-Nicolson finite difference scheme. Here we shall follow the same strategy for a fourth order spatial discretization and present two dimensional simulation results.

This chapter is organized as follows: In §2.2 we derive the compact fourth order scheme for the Schrödinger equation, and in §2.3 we construct the corresponding DTBCs, which are of convolution form. Their highly oscillatory convolution coefficients are analyzed and finally replaced by nicely decaying coefficients in §2.4. In the last section we present some numerical simulations to illustrate the effectiveness and accuracy of our DTBCs. Finally we give an application of inhomogeneous DTBCs to a 2D waveguide simulation with a T-shaped quantum transistor.

### 2.2 A fourth order difference scheme for the Schrödinger equation

In this section we consider the time-dependent Schrödinger equation on the whole space  $\mathbb{R}^2$ . Let  $\Omega_{\Delta x, \Delta y}$  be an equidistant grid with the nodes  $x_j = j\Delta x$ ,  $y_k = k\Delta y$  for  $j, k \in \mathbb{Z}$ . In time we use the discretization  $t_n = n\Delta t$ ,  $n \in \mathbb{N}_0$ , such that  $\psi_{j,k}^n \sim \psi(x_j, y_k, t_n)$  denotes an approximation of the solution  $\psi(x, y, t)$  of the Schrödinger equation (2.1) on the space-time-grid. For the discretization of (2.1), we recall the standard finite difference operators

$$\begin{aligned}
 D_t^+ \psi_{j,k}^n &:= \frac{\psi_{j,k}^{n+1} - \psi_{j,k}^n}{\Delta t}, \\
 D_x^2 \psi_{j,k}^n &:= \frac{\psi_{j-1,k}^n - 2\psi_{j,k}^n + \psi_{j+1,k}^n}{\Delta x^2}, \\
 D_y^2 \psi_{j,k}^n &:= \frac{\psi_{j,k-1}^n - 2\psi_{j,k}^n + \psi_{j,k+1}^n}{\Delta y^2},
 \end{aligned} \tag{2.5}$$

and the abbreviations

$$\psi_{j,k}^{n+\frac{1}{2}} := \frac{1}{2} (\psi_{j,k}^{n+1} + \psi_{j,k}^n),$$

## 2.2 A fourth order difference scheme for the Schrödinger equation

---

$$V_{j,k}^{n+\frac{1}{2}} := V\left(x_j, y_k, t_{n+\frac{1}{2}}\right).$$

With these notations the second order finite difference Crank-Nicolson discretization of the two dimensional Schrödinger equation reads

$$iD_t^+ \psi_{j,k}^n = -\frac{1}{2}D_x^2 \psi_{j,k}^{n+\frac{1}{2}} - \frac{1}{2}D_y^2 \psi_{j,k}^{n+\frac{1}{2}} + V_{j,k}^{n+\frac{1}{2}} \psi_{j,k}^{n+\frac{1}{2}}, \quad j, k \in \mathbb{Z}, n \in \mathbb{N}_0. \quad (2.6)$$

This scheme preserves in time the discrete  $L^2$ -norm, which has been shown in [EhAr01].

Higher order finite difference schemes for the Schrödinger equation have been developed for example in [AvKoSi00], [KaMoSi05] and the references therein. Now we briefly recall the derivation of compact, higher order schemes and prove their discrete  $L^2$ -conservation for the Schrödinger equation. Consider first the differential equation

$$\psi''(x) = f(x, \psi), \quad x \in \mathbb{R}, \psi : \mathbb{R} \rightarrow \mathbb{C}. \quad (2.7)$$

The difference equation

$$D_x^2 \psi_j = \frac{1}{12}(f_{j+1} + 10f_j + f_{j-1}), \quad j \in \mathbb{Z} \quad (2.8)$$

yields a fourth order approximation of (2.7) (see [Co66]). In the physical literature this scheme is often called *Numerov's method*. Applying this scheme to the 1D time-dependent Schrödinger equation leads to the discretization

$$D_x^2 \psi_j^{n+\frac{1}{2}} = \frac{1}{6} \left( V_{j-1}^{n+\frac{1}{2}} \psi_{j-1}^{n+\frac{1}{2}} - iD_t^+ \psi_{j-1}^n + 10V_j^{n+\frac{1}{2}} \psi_j^{n+\frac{1}{2}} - 10iD_t^+ \psi_j^n + V_{j+1}^{n+\frac{1}{2}} \psi_{j+1}^{n+\frac{1}{2}} - iD_t^+ \psi_{j+1}^n \right), \quad j \in \mathbb{Z}, n \in \mathbb{N}_0 \quad (2.9)$$

as described in [Mo04].

Consider now the two dimensional Schrödinger equation. With the semidiscretization  $\psi(x, y, t_n) \sim \psi^n(x, y)$  in time, the usual Crank-Nicolson scheme reads

$$\Delta \psi^{n+\frac{1}{2}}(x, y) = 2V^{n+\frac{1}{2}}(x, y) \psi^{n+\frac{1}{2}}(x, y) - 2iD_t^+ \psi^n(x, y), \quad n \in \mathbb{N}_0. \quad (2.10)$$

In order to derive a higher order spatial discretization, the compact nine-point scheme (cf. [St04], e.g.) is applied to equation (2.10). With the finite difference operator

$$\tilde{D}^2 := D_x^2 + D_y^2 + \frac{\Delta x^2 + \Delta y^2}{12} D_x^2 D_y^2$$

## 2 DTBCs for the Schrödinger equation – a higher compact order scheme

and the identity operator  $I$ , this yields a new generalization of in the 1D case from [Mo04]:

$$\tilde{D}^2 \psi_{j,k}^{n+\frac{1}{2}} = \left( I + \frac{\Delta x^2}{12} D_x^2 + \frac{\Delta y^2}{12} D_y^2 \right) \left[ 2V_{j,k}^{n+\frac{1}{2}} \psi_{j,k}^{n+\frac{1}{2}} - 2iD_t^+ \psi_{j,k}^n \right],$$

$$j, k \in \mathbb{Z}, n \geq 0. \quad (2.11)$$

It approximates the solution of the Schrödinger equation (2.1) with the order  $\mathcal{O}(\Delta x^4 + \Delta y^4 + \Delta t^2)$ .

It is well known that the Schrödinger equation (in whole space or with homogeneous Dirichlet boundary conditions) preserves the  $L^2(\Omega)$ -norm in time. Like the usual second order finite-difference Crank-Nicolson method, the fourth order scheme (2.11) preserves the discrete  $L^2$ -norm:

**Definition 2.1** For  $f$  either in  $\ell^2(\mathbb{Z})$  or  $\ell^2(\mathbb{Z}^2)$ , we put the positive definite, bounded and self-adjoint operator

$$A := I + \frac{\Delta x^2}{12} D_x^2$$

or

$$A := I + \frac{\Delta x^2}{12} D_x^2 + \frac{\Delta y^2}{12} D_y^2,$$

respectively.

To show that  $A$  is positive, we write  $A = \frac{2}{3}I + \frac{1}{12}S_j^+ + \frac{1}{12}S_j^- + \frac{1}{12}S_k^+ + \frac{1}{12}S_k^-$  with the shift operators  $S_{j/k}^{+/-}$ . The shift operators have the  $\mathcal{B}(\ell^2(\mathbb{Z}^2))$ -norm 1 and  $S_{j/k}^+$  is the adjoint operator to  $S_{j/k}^-$ ,  $\langle f, S_{j/k}^+ f \rangle = \overline{\langle f, S_{j/k}^- f \rangle}$ ,  $f \in \ell^2(\mathbb{Z}^2)$ :

$$\begin{aligned} \langle f, S_j^+ f \rangle &= \sum_{j,k \in \mathbb{Z}} \bar{f}_{j,k} (S_j^+ f)_{j,k} = \sum_{j,k \in \mathbb{Z}} \bar{f}_{j,k} f_{j+1,k} \\ &= \sum_{j,k \in \mathbb{Z}} \bar{f}_{j-1,k} f_{j,k} = \sum_{j,k \in \mathbb{Z}} \overline{(S_j^- f)_{j,k}} f_{j,k} \\ &= \overline{\langle f, S_j^- f \rangle}. \end{aligned}$$

We estimate  $\langle f, Af \rangle$  with the help of  $Re(z) \geq -|z|$ ,  $z \in \mathbb{C}$  and the Cauchy-Schwarz inequality:

$$\begin{aligned} \langle f, Af \rangle &= \frac{2}{3} \langle f, If \rangle + \frac{1}{12} (\langle f, S_j^+ f \rangle + \langle f, S_j^- f \rangle + \langle f, S_k^+ f \rangle + \langle f, S_k^- f \rangle) \\ &= \frac{2}{3} \|f\|_{\ell^2(\mathbb{Z}^2)}^2 + \frac{1}{12} (\overline{\langle f, S_j^- f \rangle} + \langle f, S_j^- f \rangle + \overline{\langle f, S_k^- f \rangle} + \langle f, S_k^- f \rangle) \end{aligned}$$

$$\begin{aligned}
 &\geq \frac{2}{3} \|f\|_{\ell^2(\mathbb{Z}^2)}^2 - \frac{1}{6} |\langle f, S_j^- f \rangle + \langle f, S_k^- f \rangle| \\
 &\geq \frac{2}{3} \|f\|_{\ell^2(\mathbb{Z}^2)}^2 - \frac{1}{6} (\|f\|_{\ell^2(\mathbb{Z}^2)} \|S_j^- f\|_{\ell^2(\mathbb{Z}^2)} + \|f\|_{\ell^2(\mathbb{Z}^2)} \|S_k^- f\|_{\ell^2(\mathbb{Z}^2)}) \\
 &\geq \frac{2}{3} \|f\|_{\ell^2(\mathbb{Z}^2)}^2 - \frac{1}{6} (\|f\|_{\ell^2(\mathbb{Z}^2)}^2 + \|f\|_{\ell^2(\mathbb{Z}^2)}^2) \\
 &\geq \frac{1}{3} \|f\|_{\ell^2(\mathbb{Z}^2)}^2 \geq 0.
 \end{aligned}$$

**Lemma 2.2 (preservation of  $\ell^2$ -norm)** *Let the grid function  $V^{n+\frac{1}{2}}$  be bounded for all  $n \in \mathbb{N}_0$ . For the whole space problems of the 1D and 2D time-dependent Schrödinger equation the schemes (2.9) and (2.11) then preserve the  $\ell^2$ -norm in time.*

**Proof:** To unify the proof for both cases we use the positive definite, bounded, and self-adjoint operators  $A$  from Definition 2.1. Also, we set  $\tilde{D}^2 := D_x^2$  for the 1D case (i.e.  $d = 1$ ). Hence, (2.9) and (2.11) both have the form

$$\tilde{D}^2 \psi^{n+\frac{1}{2}} = A \left[ 2V^{n+\frac{1}{2}} \psi^{n+\frac{1}{2}} - 2iD_t^+ \psi^n \right],$$

or

$$iD_t^+ \psi^n = V^{n+\frac{1}{2}} \psi^{n+\frac{1}{2}} - \frac{1}{2} A^{-1} \tilde{D}^2 \psi^{n+\frac{1}{2}}, \quad (2.12)$$

since  $A$  is invertible.

It remains to show that the r.h.s. of (2.12) is self-adjoint on  $\ell^2(\mathbb{Z}^d)$ , as this implies the preservation of the  $\ell^2$ -norm. Defining the operator  $B := I - A$  yields  $\|B\| \leq \frac{2}{3}$ . We apply the *von Neumann series* to achieve

$$\sum_{n=0}^{\infty} B^n = (I - B)^{-1} = A^{-1}.$$

Since  $B$  commutes with  $\tilde{D}$ , also  $A^{-1}$  does. Hence,  $V^{n+\frac{1}{2}} - \frac{1}{2} A^{-1} \tilde{D}^2$  is self-adjoint and the assertion follows. □

## 2.3 Discrete transparent boundary conditions for the fourth order difference scheme

As in §2.1, we consider here the Schrödinger equation

$$i \frac{\partial}{\partial t} \psi(x, y, t) = -\frac{1}{2} \Delta \psi(x, y, t) + V(x, y, t) \psi(x, y, t), \quad (x, y) \in \Omega, t > 0,$$

## 2 DTBCs for the Schrödinger equation – a higher compact order scheme

$$\begin{aligned}\psi(x, y, 0) &= \psi^I(x, y), & (x, y) \in \Omega, \\ \psi(x, 0, t) &= \psi(x, Y, t) = 0, & x \in \mathbb{R}, t > 0,\end{aligned}\tag{2.13}$$

on the infinite stripe  $\Omega = \mathbb{R} \times (0, Y)$  with some  $Y > 0$ . We assume that the initial function  $\psi^I \in L^2(\Omega)$  has compact support

$$\text{supp } \psi^I(x, y) \subset (0, X) \times (0, Y) =: \Omega_{\text{comp}}\tag{2.14}$$

which will be our computational domain. The potential  $V(x, y, t)$  is assumed to be an  $L^\infty(\Omega_{\text{comp}} \times \mathbb{R}^+)$  function in space and time, and constant on each of the two exterior domains.

In this section we shall derive at  $x = 0$  and  $x = X$  discrete transparent boundary conditions for (2.13), discretized by scheme (2.11). With the equidistant grid  $\Omega_{\Delta x, \Delta y} = (j\Delta x, k\Delta y)$  for  $j \in \mathbb{Z}; k = 0, \dots, K \in \mathbb{N}; t_n = n\Delta t, n \in \mathbb{N}_0$  and the abbreviations

$$D := \frac{\Delta x^2}{\Delta y^2},$$

$$C := \frac{\Delta x^2 + \Delta y^2}{12\Delta y^2},$$

$$W := \frac{i\Delta x^2}{3\Delta t},$$

$$\alpha_{j,k}^n := 2C - W + \frac{\Delta x^2}{6} V_{j,k}^{n+\frac{1}{2}},$$

$$\beta_{j,k}^n := -2 - 2D - 8\alpha_{j,k}^n + 20C$$

the discretization of (2.13) with scheme (2.11) reads explicitly:

$$\begin{aligned}& (1 - \alpha_{j+1,k}^n) \psi_{j+1,k}^{n+1} + (1 - \alpha_{j-1,k}^n) \psi_{j-1,k}^{n+1} + (D - \alpha_{j,k+1}^n) \psi_{j,k+1}^{n+1} \\ & + (D - \alpha_{j,k-1}^n) \psi_{j,k-1}^{n+1} + \beta_{j,k}^n \psi_{j,k}^{n+1} \\ & + C \left[ \psi_{j-1,k-1}^{n+1} + \psi_{j-1,k+1}^{n+1} + \psi_{j+1,k-1}^{n+1} + \psi_{j+1,k+1}^{n+1} \right] \\ & = (2W - 1 + \alpha_{j+1,k}^n) \psi_{j+1,k}^n + (2W - 1 + \alpha_{j-1,k}^n) \psi_{j-1,k}^n \\ & + (2W - D + \alpha_{j,k+1}^n) \psi_{j,k+1}^n + (2W - D + \alpha_{j,k-1}^n) \psi_{j,k-1}^n \\ & + (16W - \beta_{j,k}^n) \psi_{j,k}^n - C \left[ \psi_{j-1,k-1}^n + \psi_{j-1,k+1}^n + \psi_{j+1,k-1}^n + \psi_{j+1,k+1}^n \right], \\ & \quad j \in \mathbb{Z}; k = 1, \dots, K; n \in \mathbb{N}_0.\end{aligned}\tag{2.15}$$

### 2.3 DTBCs for the fourth order difference scheme

The idea of deriving DTBCs is to eliminate the exterior problem by using the explicit solution on the outer domain  $\Omega_{comp}^C := \Omega \setminus \Omega_{comp}$ . This is the reason for assuming a uniform grid on  $\Omega_{comp}^C$ . On  $\Omega_{comp}$ , however, the grid can be non-uniform, or even adaptive in time. Following the strategy of [ArEhSo03], this is done with a  $\mathcal{Z}$ -transformation in time and a discrete sine-transformation in  $y$ -direction. The outer grid domain  $\Omega_{\Delta x, \Delta y}^C = (j\Delta x, k\Delta y)$  for  $j \leq 0, j \geq J, 0 \leq k \leq K, j, k \in \mathbb{Z}$  is divided into  $K - 1$  stripes. Hence, we get  $K - 1$  linearly independent modes, because the potential is assumed to be constant on  $\Omega_{\Delta x, \Delta y}^C$ . The DTBCs in [ArEhSo03] were obtained for the Schrödinger equation discretized with a second order difference scheme. Recently in [Mo04] and [Mo06] the author adapted the DTBCs from [ArEhSo03] for the 1D Schrödinger equation discretized with the higher order scheme (2.9) – in [Mo04] for the time-dependent and in [Mo06] for the steady-state case.

With the discrete sine-transform in  $y$ -direction on  $\Omega_{\Delta x, \Delta y}^C$

$$\widehat{\psi}_{j,m}^n := \frac{2}{K} \sum_{k=1}^{K-1} \psi_{j,k}^n \sin\left(\frac{\pi k m}{K}\right), \quad m = 1, \dots, K-1, \quad (2.16)$$

a new system for the modes  $\widehat{\psi}_{j,m}^n, m = 1, \dots, K-1, j \leq 0$  and  $j \geq J$  follows:

$$\begin{aligned} \gamma_m \widehat{\psi}_{j+1,m}^{n+1} + \gamma_m \widehat{\psi}_{j-1,m}^{n+1} + \rho_m \widehat{\psi}_{j,m}^{n+1} \\ = (2W - \gamma_m) \widehat{\psi}_{j+1,m}^n + (2W - \gamma_m) \widehat{\psi}_{j-1,m}^n + (\kappa_m - \rho_m) \widehat{\psi}_{j,m}^n, \end{aligned} \quad (2.17)$$

with the abbreviations

$$\begin{aligned} \gamma_m &:= 1 + 2C \left( \cos\left(\frac{\pi m}{K}\right) - 1 \right) + W - \frac{\Delta x^2}{6} V, \\ \kappa_m &:= 4 \left( \cos\left(\frac{\pi m}{K}\right) + 4 \right) W, \\ \rho_m &:= -2 - 2D + 4C + 8W - \frac{4\Delta x^2}{3} V \\ &\quad + \left( 2D - 4C + 2W - \frac{\Delta x^2}{3} V \right) \cos\left(\frac{\pi m}{K}\right), \quad m = 1, \dots, K-1. \end{aligned} \quad (2.18)$$

While the potential may take different constant values on each semiinfinite, exterior stripe, we skipped this dependence in the above constants to simplify the notation. Next we  $\mathcal{Z}$ -transform the system (2.17) using

$$\mathcal{Z}\left(\widehat{\psi}_{j,m}^n\right) := \Phi_{j,m}(z) := \sum_{n=0}^{\infty} \widehat{\psi}_{j,m}^n z^{-n} \quad \text{with } z \in \mathbb{C}, |z| > 1.$$

## 2 DTBCs for the Schrödinger equation – a higher compact order scheme

We shall discuss here the derivation of the DTBCs at the right boundary, i.e.  $j = J$ ; the case  $j = 0$  is completely analogous. We choose the initial function  $\psi_{j,k}^0$  such that  $\psi_{j,k}^0 = 0$  for all  $j \geq J - 1$ ,  $j \leq 1$  and all  $k$ . Hence,

$$\widehat{\psi}_{J+1,m}^0 = \widehat{\psi}_{J-1,m}^0 = \widehat{\psi}_{J,m}^0 = 0, \quad m = 1, \dots, K - 1.$$

The  $\mathcal{Z}$ -transformed system (2.17) reads

$$\Phi_{j+1,m}(z) + \left[ \frac{\rho_m(z+1) - \kappa_m}{\gamma_m(z+1) - 2W} \right] \Phi_{j,m}(z) + \Phi_{j-1,m}(z) = 0, \\ j \geq J, m = 1, \dots, K - 1. \quad (2.19)$$

This is a this second order finite difference equation (in the  $j$ -variable). Its characteristic equation

$$(\nu_m(z))^2 + \left[ \frac{\rho_m(z+1) - \kappa_m}{\gamma_m(z+1) - 2W} \right] \nu_m(z) + 1 = 0$$

has two solutions  $\nu_m^{(1)}(z)$ ,  $\nu_m^{(2)}(z)$ . For each mode  $m = 1, \dots, K - 1$  we shall only consider the one solution satisfying  $|\nu_m(z)| < 1$ . The corresponding, decaying solution  $\Phi_{j,m}(z) = (\nu_m(z))^j$ ,  $j \geq J$  of (2.19) then yields the  $\mathcal{Z}$ -transformed DTBCs at  $j = J$  for each mode:

$$\Phi_{J,m}(z) = \nu_m(z) \Phi_{J-1,m}(z)$$

with

$$\nu_{J,m}(z) = \frac{-\rho_{J,m}(z+1) + \kappa_m + \sqrt{\zeta_{J,m}z^2 - 2\xi_{J,m}z + \theta_{J,m}}}{2\gamma_{J,m}(z - \eta_{J,m})}. \quad (2.20)$$

Here, we use the constants

$$\eta_{J,m} := \frac{2W}{\gamma_{J,m}} - 1, \\ \zeta_{J,m} := (\rho_{J,m})^2 - 4(\gamma_{J,m})^2, \\ \theta_{J,m} := (\kappa_m - \rho_{J,m})^2 - 4(\gamma_{J,m}\eta_{J,m})^2, \\ \xi_{J,m} := -(\rho_{J,m})^2 - 4(\gamma_{J,m})^2\eta_{J,m} + \rho_{J,m}\kappa_m \quad (2.21)$$

for  $m = 1, \dots, K - 1$ , and analogously for  $j \leq 0$ . With some work one can calculate analytically the  $\mathcal{Z}$ -inverse of (2.20):  $\mathcal{Z}^{-1}(\nu_{J,m}(z))^{(n)} =: \ell_{J,m}^{(n)}$ . We use the auxiliary function

$$F(z, \mu_{J,m}) := \frac{z}{\sqrt{z^2 - 2\mu_{J,m}z + 1}}$$

### 2.3 DTBCs for the fourth order difference scheme

---

with

$$\mu_{J,m} := \frac{\xi_{J,m}}{\sqrt{\zeta_{J,m}}\sqrt{\theta_{J,m}}}, \quad m = 1, \dots, K-1. \quad (2.22)$$

Using the abbreviations

$$\begin{aligned} \lambda_{J,m} &:= \frac{\sqrt{\zeta_{J,m}}}{\sqrt{\theta_{J,m}}}, \\ \tau_{J,m} &:= \frac{\theta_{J,m}}{\eta_{J,m}} - \zeta_{J,m}\eta_{J,m} - 2\xi_{J,m}, \quad m = 1, \dots, K-1, \end{aligned} \quad (2.23)$$

we obtain by comparison of coefficients

$$\begin{aligned} \frac{1}{z - \eta_{J,m}} \sqrt{\zeta_{J,m}z^2 - 2\xi_{J,m}z + \theta_{J,m}} \\ = \frac{1}{\sqrt{\zeta_{J,m}}} \left( \zeta_{J,m} - \frac{\theta_{J,m}}{z\eta_{J,m}} + \frac{\tau_{J,m}}{z - \eta_{J,m}} \right) F(z, \mu_{J,m}). \end{aligned}$$

Now we can calculate the inverse  $\mathcal{Z}$ -transformation  $(\mathcal{Z}^{-1}[\nu_{1,2}(z)])_n = \ell_{J,m}^{(n)}$  of

$$\begin{aligned} \nu_{J,m}(z) &= -\frac{\rho_{J,m}}{2\gamma_{J,m}} \frac{z}{z - \eta_{J,m}} - \frac{\rho_{J,m} - \kappa_m}{2\gamma_{J,m}} \frac{1}{z - \eta_{J,m}} \\ &\quad + \frac{1}{2\gamma_{J,m}} \frac{1}{\sqrt{\zeta_{J,m}}} \left( \zeta_{J,m} - \frac{\theta_{J,m}}{z\eta_{J,m}} + \frac{\tau_{J,m}}{z - \eta_{J,m}} \right) F(z, \mu_{J,m}) \end{aligned}$$

by

$$\begin{aligned} \ell_{J,m}^{(n)} &= -\frac{\rho_{J,m}}{2\gamma_{J,m}} \eta_{J,m}^n - \frac{\rho_{J,m} - \kappa_m}{2\gamma_{J,m}} \left( \eta_{J,m}^{n-1} - \frac{1}{\eta_{J,m}} \delta_n^0 \right) + \frac{\sqrt{\theta_{J,m}}}{2\gamma_{J,m}} \left[ \lambda_{J,m}^{1-n} P_n(\mu_{J,m}) \right. \\ &\quad \left. - \frac{1}{\eta_{J,m}} \lambda_{J,m}^{-n} P_{n-1}(\mu_{J,m}) + \frac{\tau_{J,m}}{\eta_{J,m} \sqrt{\theta_{J,m}} \zeta_{J,m}} \sum_{k=0}^{n-1} (\lambda_{J,m} \eta_{J,m})^n P_k(\mu_{J,m}) \right]. \end{aligned}$$

**Theorem 2.3 (DTBCs for the 2D Schrödinger equation)** *The sine-transformed DTBCs at  $j = 0$  and  $j = J$  for the discretization scheme (2.15) read*

$$\widehat{\psi}_{1,m}^n - \ell_{0,m}^{(0)} \widehat{\psi}_{0,m}^n = \sum_{k=1}^{n-1} \ell_{0,m}^{(n-k)} \widehat{\psi}_{0,m}^k, \quad n \geq 1, \quad (2.24)$$

$$\widehat{\psi}_{J-1,m}^n - \ell_{J,m}^{(0)} \widehat{\psi}_{J,m}^n = \sum_{k=1}^{n-1} \ell_{J,m}^{(n-k)} \widehat{\psi}_{J,m}^k, \quad n \geq 1. \quad (2.25)$$

## 2 DTBCs for the Schrödinger equation – a higher compact order scheme

The coefficients  $\ell_{j,m}^{(n)}$  for  $j = 0, J$ ,  $m = 1, \dots, K - 1$  and  $n \geq 0$  are given by

$$\begin{aligned} \ell_{j,m}^{(n)} = & -\frac{\rho_{j,m}}{2\gamma_{j,m}}\eta_{j,m}^n + \frac{\kappa_m - \rho_{j,m}}{2\gamma_{j,m}} \left( \eta_{j,m}^{n-1} - \frac{1}{\eta_{j,m}}\delta_n^0 \right) \\ & + \frac{\sqrt{\theta_{j,m}}}{2\gamma_{j,m}}\lambda_{j,m}^{1-n} \left[ P_n(\mu_{j,m}) - \frac{P_{n-1}(\mu_{j,m})}{\eta_{j,m}\lambda_{j,m}} \right. \\ & \left. + \frac{\tau_{j,m}}{\zeta_{j,m}\eta_{j,m}} \sum_{k=0}^{n-1} (\lambda_{j,m}\eta_{j,m})^{n-k} P_k(\mu_{j,m}) \right] \end{aligned} \quad (2.26)$$

with the Legendre polynomials  $P_n$  ( $P_{-1} \equiv 0$ ), the Kronecker symbol  $\delta_n^0$ , and the abbreviations used in (2.18), (2.21), (2.22) and (2.23). For all  $j, m$  holds  $\theta_{j,m} = \bar{\zeta}_{j,m}$ , thus one can verify  $|\lambda_{j,m}| = 1$ .

**Remark 2.1** In (2.24), (2.25) the DTBCs are written in the sine-transformed space. Since they are local in the  $y$ -Fourier space, this is the efficient way to implement them. A direct implementation in position space would necessitate much bigger numerical costs. Thus the discrete convolution

$$\hat{C}_{J,m}^{(n-1)} := \frac{1}{K} \sum_{\nu=1}^{n-1} \ell_{J,m}^{(n-\nu)} \hat{\psi}_{J,m}^{\nu}, \quad m = 1, \dots, K - 1$$

for the right boundary  $x_J = J\Delta x$  is calculated in Fourier space and inverse transformed. The left hand sides of (2.24), (2.25) have to be transformed back also into position space. Hence, we get a coupling between all boundary points (cf. §1).

## 2.4 Asymptotic behaviour of the convolution coefficients

Just like for the one-dimensional case [EhAr01] and for the standard five-point finite difference scheme for the two dimensional Schrödinger equation [ArEhSo03], the convolution coefficients (2.26) are highly oscillatory as a function of  $n \in \mathbb{N}_0$ . Figure 2.1(a) shows the real part of the convolution coefficients  $\ell_{j,m}^{(n)}$  of the DTBCs for the Schrödinger equation calculated on the domain  $\Omega_{comp} = (0, 1) \times (0, 1)$  with the parameters  $\Delta x = \Delta y = 0.02$ ,  $\Delta t = 2 \cdot 10^{-5}$ ,  $V = 0$  as a function of the time steps  $n = 0, \dots, 1000$ .

**Lemma 2.4** For large  $n$ , the convolution coefficients  $\ell_{j,m}^{(n)}$  given in (2.26) have the asymptotic behaviour

$$\ell_{j,m}^{(n)} \sim \sigma_{j,m} e^{i\vartheta_{j,m}n} \quad (2.27)$$

## 2.4 Asymptotic behaviour of the convolution coefficients

---

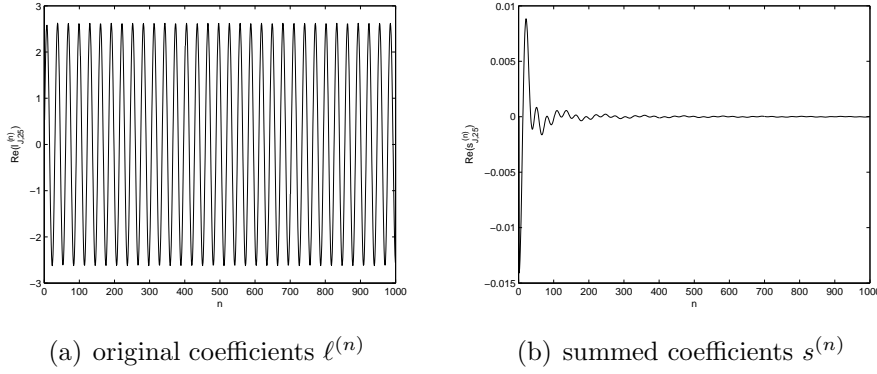


Figure 2.1: Time dependence of the convolution coefficients. For both plots we have taken  $\Delta x = \Delta y = 0.02$ ,  $V = 0$ , and  $\Delta t = 2 \cdot 10^{-5}$ . (a) shows the real part of the convolution coefficients  $\ell_{J,m}^{(n)}$  for the mode  $m = 25$  as a function of the time step  $n = 0, \dots, 1000$ . The real part of modified convolution coefficients  $s_{J,m}^{(n)} := \ell_{J,m}^{(n)} - \eta_{J,m} \ell_{J,m}^{(n-1)}$  for  $n \geq 2$  is plotted in (b).

as  $n \rightarrow \infty$ , with

$$\sigma_{j,m} := -\frac{\rho_{j,m}}{2\gamma_{j,m}} + \frac{\kappa_m - \rho_{j,m}}{2\gamma_{j,m}\eta_{j,m}} + \frac{\sqrt{\tau_{j,m}}}{2\gamma_{j,m}\sqrt{\eta_{j,m}}}, \quad \vartheta_{j,m} = \arg(\eta_{j,m})$$

for  $j = 0, J$  and  $m = 1, \dots, K - 1$ .

**Proof:** For all  $j = 0, J$ ;  $m = 1, \dots, K - 1$  it holds  $|\eta_{j,m}| = |\lambda_{j,m}| = 1$  and  $\mu_{j,m} \in \mathbb{R}$ . One easily obtains

$$|\eta_{j,m}| = \left| \frac{2W}{1 + 2C \left( \cos\left(\frac{\pi m}{K}\right) - 1\right) - \frac{\Delta x^2 V_j}{6} + W} - 1 \right| = 1,$$

because  $W \in \mathbb{C} \setminus \mathbb{R}$  and  $1 + 2C \left( \cos\left(\frac{\pi m}{K}\right) - 1\right) - \frac{\Delta x^2 V_j}{6} \in \mathbb{R}$ . Since  $\zeta_{j,m} = \bar{\theta}_{j,m}$  for  $j = 0, J$ ;  $m = 1, \dots, K - 1$ , we obtain  $|\lambda_{j,m}| = 1$ . Additionally one can verify (with Maple, e. g.) that  $|\mu_{j,m}| < 1$  for all  $j = 0, J$ ;  $m = 1, \dots, K - 1$ . Hence, there exists the representations

$$\begin{aligned} \lambda_{j,m} &= e^{i\varphi_{j,m}}, & \varphi_{j,m} &\in \mathbb{R}, \\ \eta_{j,m} &= e^{i\vartheta_{j,m}}, & \vartheta_{j,m} &\in \mathbb{R}, \\ \mu_{j,m} &= \cos(\omega_{j,m}), & 0 < \omega_{j,m} < \pi. \end{aligned}$$

## 2 DTBCs for the Schrödinger equation – a higher compact order scheme

With the formula of Laplace (cf. [Sz75]) follows

$$P_n(\cos(\omega_{j,m})) = \frac{\sqrt{2}}{\sqrt{\pi \sin(\omega_{j,m})}} \frac{\cos \left[ \left(n + \frac{1}{2}\right) \omega_{j,m} - \frac{\pi}{4} \right]}{\sqrt{n}} + \mathcal{O}(n^{-3/2}), \quad (2.28)$$

where the bound of the error term holds uniformly in the interval  $\epsilon \leq \omega_{j,m} \leq \pi - \epsilon$  for all  $\epsilon > 0$ . Hence we have

$$\lim_{n \rightarrow \infty} P_n(\cos(\omega_{j,m})) = 0$$

uniformly on  $\epsilon \leq \omega_{j,m} \leq \pi - \epsilon$  for any  $\epsilon > 0$ , and (from (2.26))

$$\begin{aligned} \ell_{j,m}^{(n)} = & -\frac{\rho_{j,m}}{2\gamma_{j,m}} e^{i\vartheta_{j,m}n} + \frac{\kappa_{j,m} - \rho_{j,m}}{2\gamma_{j,m}} e^{i\vartheta_{j,m}(n-1)} \\ & + \frac{\sqrt{\theta_{j,m}} \tau_{j,m}}{2\gamma_{j,m} \zeta_{j,m}} e^{i\vartheta_{j,m}(n-1)} e^{i\varphi_{j,m}} \sum_{k=0}^{n-1} e^{-i(\varphi_{j,m} + \vartheta_{j,m})k} P_k(\mu_{j,m}) + \mathcal{O}\left(\frac{1}{\sqrt{n}}\right) \end{aligned}$$

for  $n$  large. For  $|2r\mu - r^2| < 1$  it holds

$$\sum_{k=0}^{\infty} r^k P_k(\mu) = \frac{1}{\sqrt{1 - 2r\mu + r^2}}$$

(cf. [Do51]). One can verify (again with Maple, e. g.) that

$$\left| \frac{2\mu_{j,m}}{\eta_{j,m} \lambda_{j,m}} - \frac{1}{(\eta_{j,m} \lambda_{j,m})^2} \right| < 1, \quad j = 0, J; m = 1, \dots, K-1.$$

This yields

$$\lim_{n \rightarrow \infty} \sum_{k=0}^{n-1} e^{-i(\varphi_{j,m} + \vartheta_{j,m})k} P_k(\mu_{j,m}) = \sqrt{\frac{\zeta_{j,m} \eta_{j,m}}{\tau_{j,m}}},$$

and finally

$$\lim_{n \rightarrow \infty} e^{-i\vartheta_{j,m}n} \ell_{j,m}^{(n)} = -\frac{\rho_{j,m}}{2\gamma_{j,m}} - \frac{\rho_{j,m} - \kappa_{j,m}}{2\gamma_{j,m} \eta_{j,m}} + \frac{\sqrt{\tau_{j,m}}}{2\gamma_{j,m} \sqrt{\eta_{j,m}}}.$$

□

Figure 2.2 shows plots of the asymptotic behaviour of the convolution coefficients. The free Schrödinger equation is discretized with  $J = K = 50$ ,  $\Delta x = \Delta y = 0.02$  and  $\Delta t = 2 \cdot 10^{-5}$ . A solution  $\psi$  is calculated for  $n = 1, \dots, 250$  time steps. In Figure 2.2(a) we present the real part of  $\ell_{J,m}^{(n)}$  and the absolute value  $|\ell_{J,m}^{(n)}|$  in

## 2.4 Asymptotic behaviour of the convolution coefficients

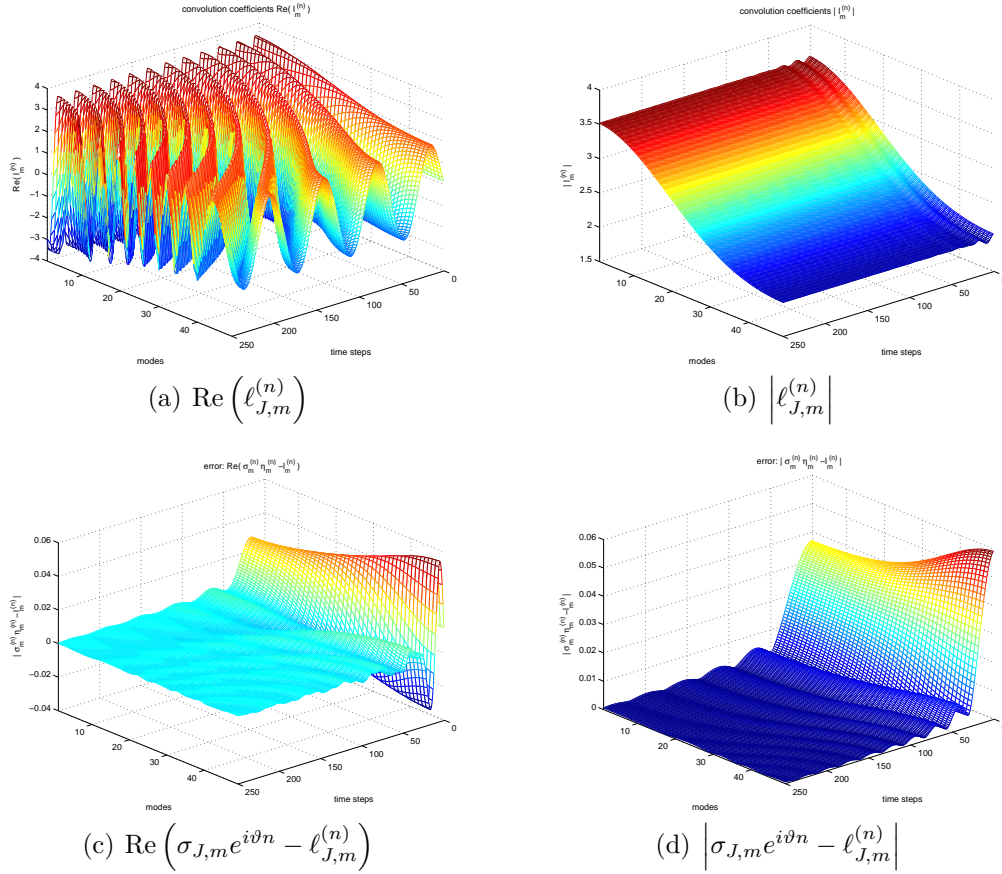


Figure 2.2: Real part (a) and absolute value (b) of the convolution coefficients  $\ell_{J,m}^{(n)}$  and real part (c) and absolute value (d) of the error  $\sigma_{J,m} e^{i\vartheta n} - \ell_{J,m}^{(n)}$  between the asymptotics (2.27) and the convolution coefficients for the modes  $m = 1, \dots, K-1$  as a function of the time steps  $n = 1, \dots, 250$ . We consider the computational domain  $\Omega_{comp} = (0, 1) \times (0, 1)$  and choose the discretization parameters  $J = K = 50$ ,  $\Delta x = \Delta y = 0.02$  and  $\Delta t = 2 \cdot 10^{-5}$ .

## 2 DTBCs for the Schrödinger equation – a higher compact order scheme

Figure 2.2(b) for all modes  $m = 1, \dots, K - 1$ . The errors  $Re(\sigma_{J,m}e^{i\vartheta n} - \ell_{J,m}^{(n)})$  and  $|\sigma_{J,m}e^{i\vartheta n} - \ell_{J,m}^{(n)}|$  between the convolution coefficients and the asymptotics (2.27) – which are converging to zero – are shown in Figure 2.2(c) and Figure 2.2(d).

Lemma 2.4 shows, that the convolution coefficients  $\ell_{j,m}^{(n)}$  are asymptotically an oscillatory sequence. Moreover, this behaviour deviates from the  $\mathcal{O}(t^{-3/2})$ -decay of the continuous convolution kernel in (2.3). Hence, it may lead to numerical cancellations in the calculation of the convolution sum (2.24), (2.25). As an alternative we shall derive coefficients that decay like  $\mathcal{O}(n^{-3/2})$ . For the left DTBCs we therefore add equation (2.24) for  $n$  and  $n + 1$  with the corresponding weighting factor 1 and  $-e^{i\vartheta 1,m} = -\eta_{1,m}$  (the case  $j = J$  is analogous) and proceed like in [EhAr01]. This gives the following reformulated DTBCs

$$\widehat{\psi}_{1,m}^n - s_{0,m}^{(0)} \widehat{\psi}_{0,m}^n = \sum_{k=1}^{n-1} s_{0,m}^{(n-k)} \widehat{\psi}_{0,m}^k + \eta_{1,m} \widehat{\psi}_{1,m}^{n-1}, \quad (2.29)$$

$$\widehat{\psi}_{J-1,m}^n - s_{J,m}^{(0)} \widehat{\psi}_{J,m}^n = \sum_{k=1}^{n-1} s_{J,m}^{(n-k)} \widehat{\psi}_{J,m}^k + \eta_{J-1,m} \widehat{\psi}_{J-1,m}^{n-1} \quad (2.30)$$

for  $n \geq 1$  with the *summed coefficients*

$$s_{j,m}^{(n)} := \begin{cases} \ell_{j,m}^{(n)} - \eta_{j,m} \ell_{j,m}^{(n-1)}, & n \geq 1, \\ \ell_{j,m}^{(0)}, & n = 0, \end{cases} \quad (2.31)$$

for  $m = 1, \dots, K - 1$ ;  $j = 0$  and  $j = J$ .

**Lemma 2.5** *For  $n \geq 2$ , the summed coefficients (2.31) can be calculated by the formula*

$$s_{j,m}^{(n)} = -\frac{\sqrt{\theta_{j,m}}}{2\gamma_{j,m}} \lambda_{j,m}^{1-n} \frac{P_n(\mu_{j,m}) - P_{n-2}(\mu_{j,m})}{2n-1}$$

or by the recursion

$$s_{j,m}^{(n+1)} = \frac{2n-1}{n+1} \frac{\mu_{j,m}}{\lambda_{j,m}} s_{j,m}^{(n)} - \frac{n-2}{n+1} (\lambda_{j,m})^{-2} s_{j,m}^{(n-1)} \quad (2.32)$$

for  $j = 0, J$  and  $m = 1, \dots, K - 1$ . These new coefficients have the asymptotic behaviour

$$s_{j,m}^{(n)} \sim \mathcal{O}(n^{-3/2}). \quad (2.33)$$

## 2.4 Asymptotic behaviour of the convolution coefficients

---

**Proof:** Using (2.26), the summed coefficients read for  $n \geq 2$

$$s_{j,m}^{(n)} = \frac{\sqrt{\theta_{j,m}}}{2\gamma_{j,m}} \lambda_{j,m}^{1-n} \left[ P_n(\mu_{j,m}) + P_{n-2}(\mu_{j,m}) - \frac{1}{\lambda_{j,m}\eta_{j,m}} P_{n-1}(\mu_{j,m}) \right. \\ \left. - \eta_{j,m}\lambda_{j,m} P_{n-1}(\mu_{j,m}) + \frac{\tau_{j,m}\lambda_{j,m}}{\zeta_{j,m}} P_{n-1}(\mu_{j,m}) \right].$$

With the recursion for the Legendre polynomials,

$$\frac{n}{2n-1} P_n(\mu_{j,m}) + \frac{n-1}{2n-1} P_{n-2}(\mu_{j,m}) = \mu_{j,m} P_{n-1}(\mu_{j,m}) \quad (2.34)$$

for  $n \geq 2$  then follows

$$s_{j,m}^{(n)} = -\frac{\sqrt{\theta_{j,m}}}{2\gamma_{j,m}} \lambda_{j,m}^{1-n} \frac{P_n(\mu_{j,m}) - P_{n-2}(\mu_{j,m})}{2n-1}. \quad (2.35)$$

This representation of the convolution coefficients is analogous to the DTBCs for the one dimensional Schrödinger equation [EhAr01] and for the five-point stencil in the two dimensional case [ArEhSo03]. Hence, the recurrence formula of §3.3 in [EhAr01] applies also here, and it gives (2.32). For the same reason, also the asymptotic behaviour  $s_{j,m}^{(n)} \sim \mathcal{O}(n^{-3/2})$  carries over from [EhAr01]. There, it is derived by applying equation (2.28) to the Legendre recursion (2.34) for  $P_n(\mu_{j,m}) - P_{n-2}(\mu_{j,m})$ .

□

**Remark 2.2** *The decay rate (2.33) of the summed convolution coefficients coincides with the decay  $\mathcal{O}(t^{-3/2})$  of the convolution kernel in the analytical TBC in (2.3) (cf. Figure 2.3). Figure 2.1(b) shows the absolute value of the summed coefficients (2.31) corresponding to the ones presented in Figure 2.1(a). Figure 2.3 shows the algebraic decay rate of the real part of the new coefficients  $s_{j,m}^{(n)}$ .*

**Remark 2.3** *Like the analytical TBC (2.2), the DTBCs (2.29), (2.30) are non-local in time. For the calculation of the solution  $\psi_{j,m}^n$  of the discretized Schrödinger equation (2.11), it is necessary to compute a convolution of the size  $n$  in the  $n$ -th time step, which leads to a quadratically growing numerical effort. In [ArEhSo03] the authors derived an approximation of the convolution coefficients by a sum of exponentials. Since we have the same recursion formulas for the summed convolution coefficients (2.31) for the higher order difference scheme like the coefficients in [ArEhSo03] for the second order scheme, we can use their results on the approximation of the convolution coefficients. It is shown there, that the convolution*

## 2 DTBCs for the Schrödinger equation – a higher compact order scheme

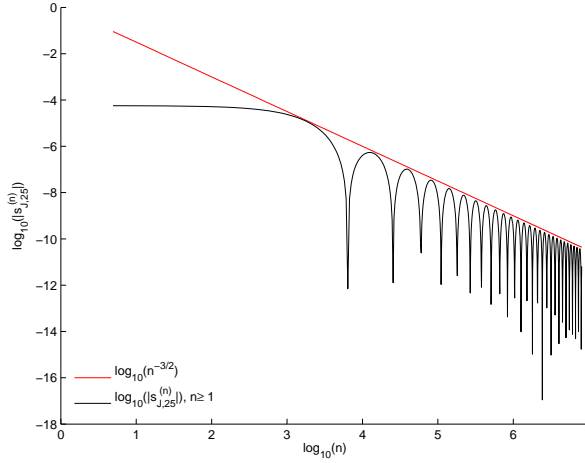


Figure 2.3: Algebraic decay rate of the new summed coefficients. The figure presents  $|s_{J,m}^{(n)}|$  as a function of the time step  $n = 1, \dots, 1000$ .  $|s_{J,25}^{(n)}|$  is plotted for  $\Delta t = 2 \cdot 10^{-5}$ ,  $\Delta x = \Delta y = 0.02$  and  $V = 0$  (black line) and compared to  $\log_{10}(n^{-3/2})$  (red line).

*coefficients can be approximated very efficiently by the sum of exponentials. With this approach, the numerical costs of the discrete convolutions in our DTBCs can be reduced from  $\mathcal{O}(KN^2)$  to  $\mathcal{O}(KLN)$ , where  $K$  denotes the number of modes,  $N$  the total number of time steps and  $L$  the number of exponential terms in the approximation. Typical values to obtain good results are  $L = 10-20$  (cf. §1). This is a very important result for long-time simulations or even the calculation of steady-states via a time-stepping approach.*

## 2.5 Numerical tests

In this section we present some numerical results and applications of DTBCs in two dimensions. First, we verify numerically the accuracy of the DTBCs for the free Schrödinger equation. Then we apply DTBCs to the simulation of the electron transport through a quantum waveguide.

### 2.5.1 Example 1: Travelling Gaussian wave functions

In the first example we study the time evolution of a Gaussian wave in a two dimensional channel  $\Omega = \mathbb{R} \times (0, 1)$ . Since the analytical solution is known here, this is a good example to test the DTBCs.

To get homogeneous Dirichlet boundary conditions at the channel walls  $y = 0$  and  $y = 1$ , we consider the  $y$ -periodic initial function

$$\psi^I(x, y) = \sum_{\ell \in \mathbb{Z}} (-1)^\ell e^{-\frac{\alpha}{2} \left[ \left(x - \frac{1}{2}\right)^2 + \left(y - \frac{1}{2} + \ell\right)^2 \right]} e^{-ik_x \left(x - \frac{1}{2}\right)} \quad (2.36)$$

on the domain  $\Omega$  with some  $\alpha > 0$ . Using the computational domain  $\Omega_{comp} = (0, 1)^2$  we consider DTBCs at  $x = 0$  and  $x = 1$ . The wave will travel along the channel in  $x$ -direction with the velocity given by the wavenumber  $k_x > 0$  and it will cross the transparent boundary at  $x = 1$  without any reflections. The solution of the time-dependent Schrödinger equation with the initial function (2.36) can be expressed analytically by

$$\psi_{ex}(x, y, t) = \frac{1}{1 + i\alpha t} \sum_{\ell \in \mathbb{Z}} (-1)^\ell e^{\frac{-1}{2 + 2i\alpha t} \left( \alpha \left[ \left(x - \frac{1}{2}\right)^2 + \left(y - \frac{1}{2} + \ell\right)^2 \right] - 2ik_x \left(x - \frac{1}{2}\right) + ik_x^2 t \right)}$$

for  $t > 0$  such that it is possible to compare the calculated solution  $\psi$  with the exact solution  $\psi_{ex}$ . Figure 2.4 shows the absolute value and Figure 2.5 the contour plots of the absolute value of the calculated solution  $\psi(x, y, t)$  at some times  $t_n$ . We use the discretization parameters  $J = K = 120$ ,  $\Delta x = \Delta y = 1/120$ ,  $\Delta t = 2 \cdot 10^{-4}$ ,  $\alpha = 120$  and the wavenumber  $k_x = 50$ . The wave leaves  $\Omega_{comp}$  without reflections. For these discretization parameters we compare in Figure 2.6(a) the relative error

$$L_1(t) = \frac{\|\psi(\cdot, \cdot, t) - \psi_{ex}(\cdot, \cdot, t)\|_{\ell^2(\Omega_{\Delta x, \Delta y})}}{\|\psi^I(\cdot, \cdot)\|_{\ell^2(\Omega_{\Delta x, \Delta y})}} \quad (2.37)$$

of the standard five-point scheme with the nine-point scheme. As expected the higher order scheme has a much smaller error. We remark that the wave packet has essentially crossed the artificial boundary at  $T = 200\Delta t$ .

In order to satisfy the assumption that  $\psi^I$  is compactly supported in  $\Omega_{comp}$  (cf. §2.3) we used a small cut-off close to  $x = 0$  and  $x = 1$ . This amounted to a relative  $\ell^2$ -error on  $\mathbb{R} \times (0, 1)$  of  $\mathcal{O}(10^{-8})$ .

Next we compare the calculated solution  $\psi$  on  $(0, 1) \times (0, 1)$  with a (more exact) reference solution  $\psi_2$  calculated on  $(0, 2) \times (0, 1)$  using DTBCs at  $x = 0$  and  $x = 2$  in order to distinguish between the error due to the difference scheme and to the DTBCs. Figure 2.6(b) shows the relative error

$$L_2(t) = \frac{\|\psi(\cdot, \cdot, t) - \psi_2(\cdot, \cdot, t)\|_{\ell^2(\Omega_{\Delta x, \Delta y})}}{\|\psi^I(\cdot, \cdot)\|_{\ell^2(\Omega_{\Delta x, \Delta y})}} \quad (2.38)$$

as a logarithmic plot for the same discretization parameters as before. Both  $\psi$  and  $\psi_2$  were calculated with the compact nine-point difference scheme. With

## 2 DTBCs for the Schrödinger equation – a higher compact order scheme

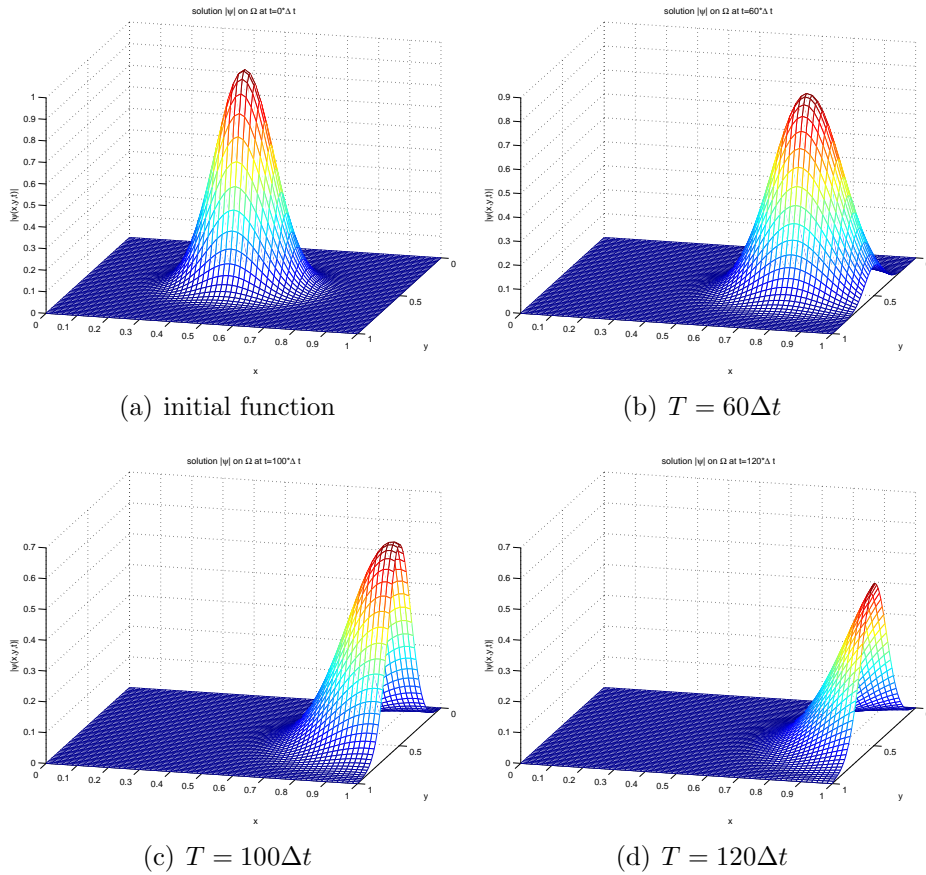


Figure 2.4: Orthogonal incidence at the boundary: absolute value of the calculated solution to the time-dependent Schrödinger equation with the initial function (2.36) on the computational domain  $(0, 1) \times (0, 1)$  with  $\Delta x = \Delta y = 1/120$ ,  $\Delta t = 2 \cdot 10^{-4}$ , and the wavenumber  $k_x = 50$ . The potential equals 0; DTBCs are implemented at  $x = 0$  and  $x = 1$ .

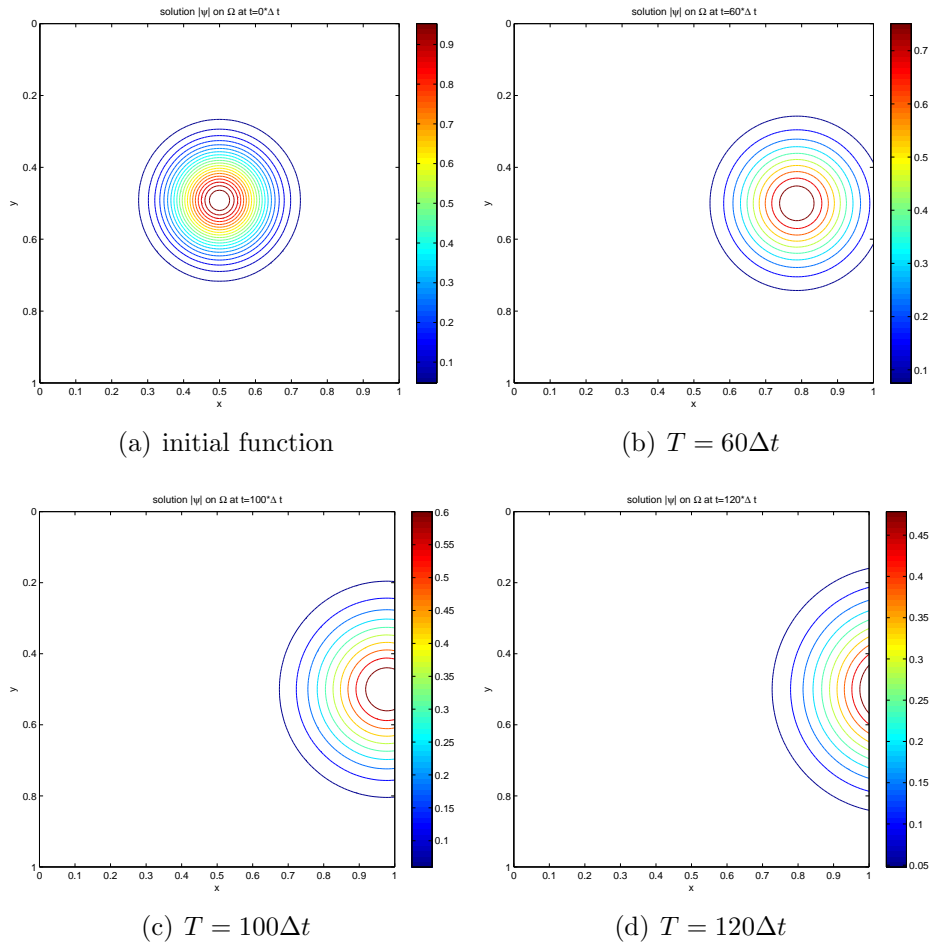


Figure 2.5: Orthogonal incidence at the boundary: absolute value of the calculated solution to the time-dependent Schrödinger equation with the initial function (2.36) on the computational domain  $(0, 1) \times (0, 1)$  as a contour plot for the same parameter set as used for Figure 2.4.

## 2 DTBCs for the Schrödinger equation – a higher compact order scheme

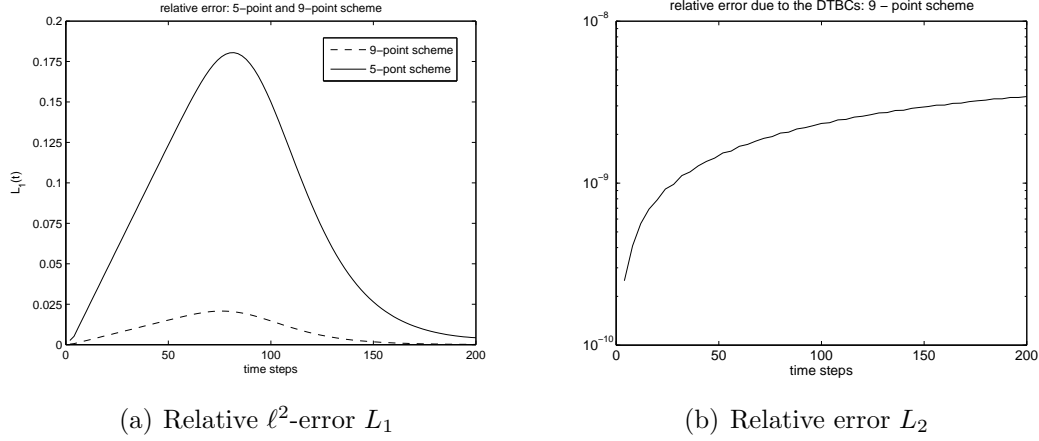


Figure 2.6: Relative errors of a travelling wave solution with the initial value (2.36) as a function of the time steps  $n = 0, \dots, 200$ . (a): relative error  $L_1$  of the finite difference scheme for the standard five-point scheme (solid line) and for the nine-point scheme (dashed line). (b): relative error  $L_2$  of the DTBCs for the nine-point scheme. In all cases we used the parameters  $\Delta x = \Delta y = 1/120$ ,  $\Delta t = 2 \cdot 10^{-4}$ ,  $\alpha = 120$ ,  $k_x = 50$ .

$L_2 \in \mathcal{O}(10^{-9})$ , the error due to the DTBC is much smaller than the error  $L_1$  of the interior PDE-scheme.

The first example has shown a Gaussian wave travelling only in  $x$ -direction and hitting the artificial boundary orthogonally. Now we modify this example and consider the initial function

$$\psi^I(x, y) = \sum_{\ell \in \mathbb{Z}} (-1)^\ell e^{-120 \left[ \left(x - \frac{1}{4}\right)^2 + \left(y - \frac{1}{4} + \ell\right)^2 \right] - ik_x x - ik_y y}, \quad k_x, k_y \in \mathbb{R} \quad (2.39)$$

on the same computational domain  $\Omega_{comp} = (0, 1) \times (0, 1)$  with  $k_x = -k_y = 100$ . As shown in Figure 2.7 and in 2.8, the wave packet passes the boundary  $x = 1$  in a non-orthogonal angle ( $45^\circ$  here) without any reflections. This example illustrates the *angular independence* of our DTBCs. In contrast to this situation here, local TBCs as introduced for wave-type equations in [EnMa77] and ABCs calculated with the potential ansatz [Bu97] show a strong dependence on the impact angle at the artificial boundary (cf. §1.3.2, §1.3.3).

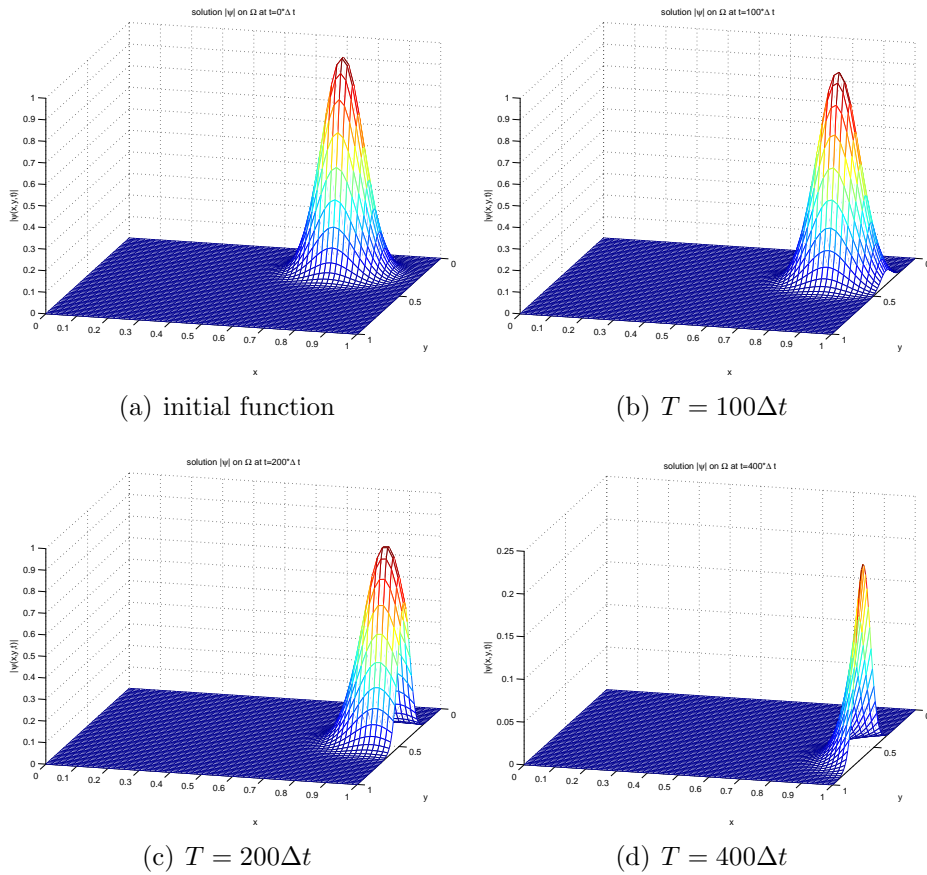


Figure 2.7: Non-orthogonal incidence at the boundary: absolute value of the calculated discrete solution to the time-dependent Schrödinger equation with the initial function (2.39) on the computational domain  $(0, 1) \times (0, 1)$  with  $J = K = 120$ ,  $\Delta x = \Delta y = 1/120$ ,  $\Delta t = 2 \cdot 10^{-5}$  and the wavenumber  $k = (100, -100)$ . The potential equals 0; DTBCs are implemented at  $x = 0$  and  $x = 1$ .

## 2 DTBCs for the Schrödinger equation – a higher compact order scheme

---

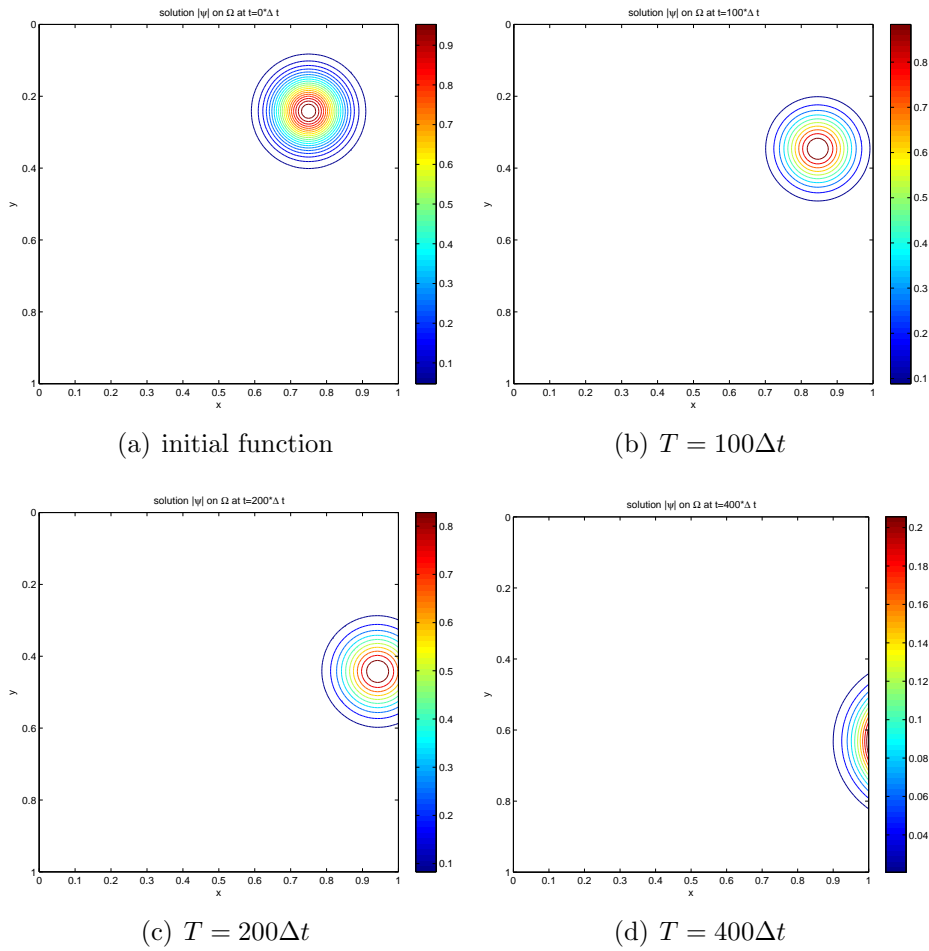


Figure 2.8: Non-orthogonal incidence at the boundary: absolute value of the calculated solution to the time-dependent Schrödinger equation with the initial function (2.39) as a contour plot for the same parameter set as used for Figure 2.7.

### 2.5.2 Example 2: Simulation of quantum waveguides

Next we turn to a physical application of DTBCs. Open boundary conditions are a crucial ingredient for Schrödinger based simulations of the electron transport through quantum semiconductor devices. Typical examples include the ballistic transport along the channel of MOSFETs (cf. [JiLu02], [WaPo04]) or quantum waveguides (cf. [Bu97] or §13.4 of [Ra02] for an analysis of *T*-shaped *quantum interference transistors*). These are novel electronic switches of nano-scale dimensions. They are made of several different layers of semiconductor materials such that the electron flow is confined to small channels or waveguides. Due to their sandwiched structure the relevant geometry for the electron current is essentially two dimensional. Following the simulation of a GaAs-waveguide in [Bu97], we choose the *T*-shaped *quantum interference transistor* shown in Figure 2.9. The actual structure can be realized as an etched layer of GaAs between two layers of doped AlGaAs. Applying an external potential at the gate (i.e. above the shaded portion of the stub), the “allowed region” for the electrons, and hence the geometry (in particular the stub length) can be modified (cf. [AiYaMi93], [ASSHLL96] for experimental realizations). This allows to control the current flow through such an electronic device. This causes a switch, which resembles a transistor on a nano-scale. With respect to small changes in the applied potential and the geometry, such a device shows sharp peaks in conductance that are due to the presence of bound states in the stub. It is expected that these novel devices will operate at low power and high speed.

The electron flow in these devices is modeled by the 2D Schrödinger equation

$$i\hbar \frac{\partial}{\partial t} \psi = -\frac{\hbar^2}{2m_*} \Delta \psi + V(x, y, t) \psi, \quad (x, y) \in \Omega, t > 0 \quad (2.40)$$

with the Planck constant  $\hbar$  and  $m_*$ , the effective mass of electrons in the semiconductor material of  $\Omega$ . To model a constant inflow of electrons at the device contacts, we use inhomogeneous TBCs. In the 1D analytical case they read (cf. [Ar01])

$$\partial_\eta (e^{iV_{ext}t} \psi - \psi^{Inc}) = -\sqrt{\frac{2m_*}{\hbar}} e^{-i\pi/4} \sqrt{\partial_t} (e^{iV_{ext}t} \psi - \psi^{Inc}),$$

$$x_0 = 0 \text{ or } x_0 = X$$

with the constant external potential  $V_{ext}$  and the incoming wave function  $\psi^{Inc}(x_0, y, t)$ . In 2D this TBC has to be applied to each Fourier mode  $\hat{\psi}_m(x, t)$ , analogously to the homogeneous case (2.4), cf. [BeMePi05].

In  $x$ -direction the channel shown in Figure 2.9 has a length of  $X = 60\text{nm}$ , the channel width  $Y_1$  and the stub width  $w$  are both  $20\text{nm}$ . In order to control the

## 2 DTBCs for the Schrödinger equation – a higher compact order scheme

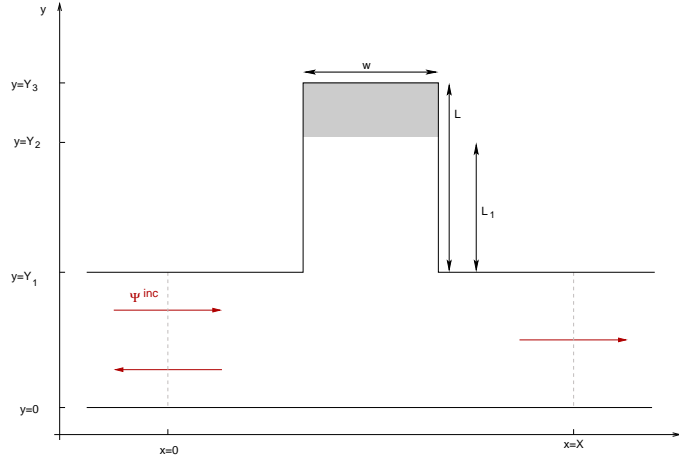


Figure 2.9: T-shaped structure  $\Omega$  with the length  $X = 60\text{nm}$ , a channel width  $Y_1 = 20\text{nm}$ , and a stub width  $w = 20\text{nm}$ . It is possible to switch the stub length from  $L_1 = 32\text{nm}$  to  $L_2 = 40.5\text{nm}$ . Inhomogeneous DTBCs are implemented at  $x = 0$  and  $x = X$ , the inflow is modeled by the function  $\psi^{Inc}$  given in equation (2.41).

current through the channel, the stublength can be changed from  $L_1 = 32\text{nm}$  to  $L_2 = 40.5\text{nm}$ . DTBCs are implemented at  $x = 0$  and  $x = X$ . All other boundaries are considered as hard walls, i.e. we use Dirichlet boundary conditions for  $\psi$ . Using  $V_{ext} = 0$ , a time harmonic incoming function

$$\psi^{Inc}(x = 0, y, t) := \sin\left(\frac{y\pi}{Y_1}\right) e^{-\frac{iEt}{\hbar}}, \quad y \in [0, Y_1] \quad (2.41)$$

is modelling the mono-energetic, constant-in-time incoming current at  $x = 0$ . Here,  $\psi^{Inc}$  includes only the lowest  $y$ -mode. But any linear combination of higher modes would work equally well, which is a great advantage compared to other artificial boundary conditions (e.g. [Bu97]). In our example the energy  $E$  of the incoming wave equals  $29.9\text{meV}$  and the effective electron mass has the value  $m_* = 0.067m_0$  ( $m_0$  being the electron mass in vacuum), which corresponds to GaAs.

For the subsequent simulation we solve the Schrödinger equation (2.40) without external potential, i.e.  $V = 0$ . For realistic simulations of MOSFET-channels (2.40) should be coupled to the self-consistent Coulomb potential inside the channel. Since we focus on DTBCs, we shall not include this here. But a coupling to the Poisson equation *inside* the computation domain does *not* change the derivation or discretization of our open boundary conditions (cf. §3).

In the following simulations we are mostly interested in the switching and the large time behaviour of this waveguide. Therefore we first need to compute a stationary state corresponding to a given incoming plane wave function  $\psi^{Inc}$ . To this end we choose the following (somewhat arbitrary) initial function

$$\psi^I(x, y) = \begin{cases} \sin\left(\frac{y\pi}{Y_1}\right) e^{ik_x x} & : 0 \leq x < x_1 \\ \frac{1}{2} \sin\left(\frac{y\pi}{Y_1}\right) e^{ik_x x} \left[1 + \cos\left(\pi \frac{x-x_1}{x_2-x_1}\right)\right] & : x_1 \leq x < x_2 \\ 0 & : x \geq x_2 \end{cases} \quad (2.42)$$

with  $x_1 = 5\text{nm}$  and  $x_2 = 15\text{nm}$ , which is consistent with the incoming wave.

In the analytical case the dispersion relation for (2.40) with a plane wave solution in the first orthogonal mode (cf. (2.41)) in the channel  $\mathbb{R} \times (0, Y_1)$  reads

$$\epsilon(k_x) = \frac{\hbar^2 k_x^2}{2m_*} + \frac{\hbar^2 \pi^2}{2m_* Y_1^2}, \quad (2.43)$$

which needs to be modified for the discretized Schrödinger equation. For a given inflow energy  $E$ , the value of  $k_x$  appearing in (2.42) can be derived from the *discrete dispersion relation*. To derive it, we first put the ansatz  $\psi_{j,1} = e^{ik_x j \Delta x} \sin\left(\frac{\pi \Delta y}{Y_1}\right)$ ,  $j \in \mathbb{Z}$  into the spatial semi-discretization (by the compact nine-point scheme) analogous to (2.11). With

$$\begin{aligned} D_x^2 \left( e^{ik_x j \Delta x} \sin\left(\frac{\pi \Delta y}{Y_1}\right) \right) &= \frac{2}{\Delta x^2} (\cos(k_x \Delta x) - 1) e^{ik_x j \Delta x} \sin\left(\frac{\pi \Delta y}{Y_1}\right), \\ D_y^2 \left( e^{ik_x j \Delta x} \sin\left(\frac{\pi \Delta y}{Y_1}\right) \right) &= \frac{2}{\Delta y^2} \left( \cos\left(\frac{\pi \Delta y}{Y_1}\right) - 1 \right) e^{ik_x j \Delta x} \sin\left(\frac{\pi \Delta y}{Y_1}\right), \end{aligned}$$

we yield

$$\begin{aligned} E_{space}(k_x) &= \left[ -\frac{\hbar^2}{m_* \Delta x^2} (\cos(k_x \Delta x) - 1) - \frac{\hbar^2}{m_* \Delta y^2} \left( \cos\left(\frac{\pi \Delta y}{Y_1}\right) - 1 \right) \right. \\ &\quad \left. - \frac{\hbar^2 (\Delta x^2 + \Delta y^2)}{6m_* \Delta x^2 \Delta y^2} (\cos(k_x \Delta x) - 1) \left( \cos\left(\frac{\pi \Delta y}{Y_1}\right) - 1 \right) \right] \\ &\quad \times \left[ 1 + \frac{1}{6} (\cos(k_x \Delta x) - 1) + \frac{1}{6} \left( \cos\left(\frac{\pi \Delta y}{Y_1}\right) - 1 \right) \right]^{-1}. \end{aligned} \quad (2.44)$$

This is the dispersion relation modified due to the spatial discretization. For the correction due to the Crank-Nicolson time discretization we use the discrete equation

$$i\hbar D_t^+ \psi_{j,k}^n = E_{time}(k_x) \psi_{j,k}^{n+\frac{1}{2}}, \quad j, k \in \mathbb{Z}, n \in \mathbb{N}_0,$$

## 2 DTBCs for the Schrödinger equation – a higher compact order scheme

---

which yields

$$\psi_{j,k}^{n+1} = \frac{2i\hbar + E_{time}(k_x)\Delta t}{2i\hbar - E_{time}(k_x)\Delta t} \psi_{j,k}^n. \quad (2.45)$$

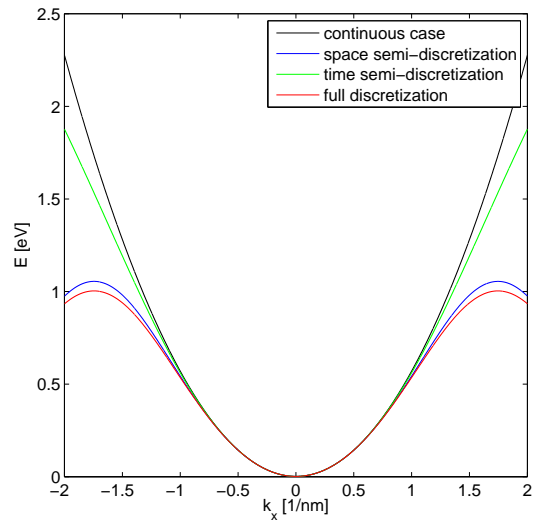
We inject incoming time-harmonic plane wave functions and therefore we set

$$e^{-\frac{iE(k_x)\Delta t}{\hbar}} = \frac{2i\hbar + E_{time}(k_x)\Delta t}{2i\hbar - E_{time}(k_x)\Delta t}. \quad (2.46)$$

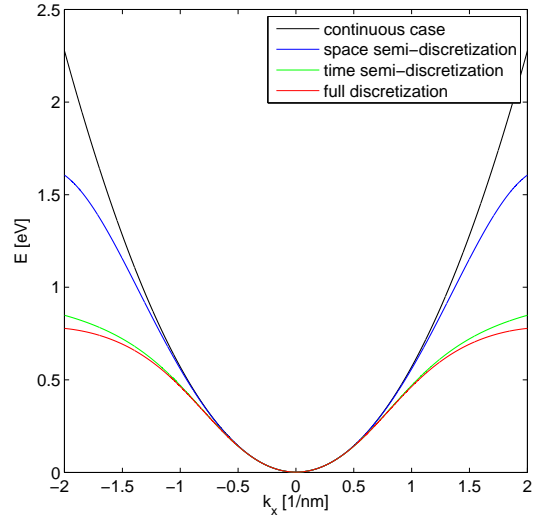
Adding this correction of the discretization due to the Crank-Nicolson time semi-discretization yields the dispersion relation

$$E(k_x) = \frac{\hbar}{i\Delta t} \ln \left( \frac{2i\hbar - \Delta t E_{space}(k_x)}{2i\hbar + \Delta t E_{space}(k_x)} \right) \quad (2.47)$$

for the discrete Schrödinger equation (analogous to (2.11)) with a time-harmonic plane wave solution. Figure 2.10 shows these different dispersion relations as functions of the wavenumber  $k_x \in [-2\text{nm}^{-1}, 2\text{nm}^{-1}]$  for three different sets of discretization parameters. For the first numerical test presented in Figure 2.10(a) we choose with  $\Delta x = 1.8\text{nm}$  and  $\Delta t = 0.5\text{fs}$  a coarse space discretization compared to the time discretization. In Figure 2.10(b) we change the parameters to  $\Delta x = 1.44\text{nm}$  and  $\Delta t = 2\text{fs}$ , and for the calculations shown in Figure 2.10(c) we choose both discretizations fine and set  $\Delta x = 1.44\text{nm}$  and  $\Delta t = 0.5\text{fs}$ . For each set of parameters we calculated and plotted the continuous dispersion relation (equation (2.43); plotted in black colour), the space semidiscrete (equation (2.44); plotted in blue colour), the time semidiscrete (equation (2.47) with  $\epsilon(k_x)$  instead of  $E_{space}$ ; plotted in green), and the fully discrete dispersion relation (equation (2.47); plotted in red) as a function of the wavenumber  $k_x \in [-2\text{nm}^{-1}, 2\text{nm}^{-1}]$ . For the coarse space discretization the values of space corrected and therefore also for the both space and time corrected energies differ clearly from the ones obtained by the continuous relation and the time corrected relations. By contrast with a fine space and a coarse time discretization the values of the time corrected and the both time and space corrected energy distinguish from the values calculated with the continuous relation and the space corrected relations. Choosing all discretization parameters  $\Delta x$ ,  $\Delta t$  small yield better approximations for all dispersion relations. But also for the parameters selected here, the continuous, the time-discretization-corrected, the space-discretization-corrected and the discrete dispersion relation are close to each other only for small values of  $k_x$ . Otherwise corrections due to  $E(k_x)$  from (2.47) are necessary.

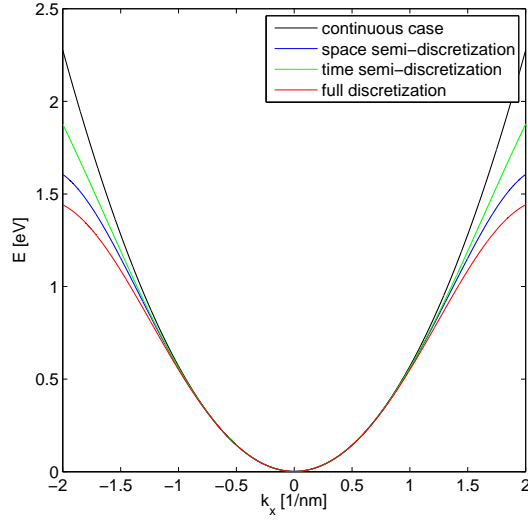


(a) coarse space discretization, fine time discretization



(b) fine space discretization, coarse time discretization

## 2 DTBCs for the Schrödinger equation – a higher compact order scheme



(c) fine space and time discretization

Figure 2.10: Dispersion relations for the Schrödinger equation (2.40) for three sets of parameters. (a) shows the relations for a discretization  $\Delta x = 1.8\text{nm}$  and  $\Delta t = 0.5\text{fs}$ , (b) for a discretization  $\Delta x = 1.44\text{nm}$  and  $\Delta t = 2\text{fs}$ , and for the calculations presented in (c) we use the discretization  $\Delta x = 1.44\text{nm}$  and  $\Delta t = 0.5\text{fs}$ . For each set of parameters we have plotted the continuous (black), space corrected (blue), time corrected (green) and the space and time corrected discrete dispersion relation (red) as a function of the wavenumber  $k_x \in [-2\text{nm}^{-1}, 2\text{nm}^{-1}]$ .

Numerical tests have shown that the real and imaginary parts of the solution to the Schrödinger equation (2.40) with constant inflow (2.41) are highly oscillatory in time, such that a fine time discretization seems necessary. Figure 2.11(a) shows the highly oscillatory evolution of the real part at one spatial grid point in the T-shaped structure with constant inflow  $\psi^{Inc}$ . For this plot we considered 50 000 time steps with  $\Delta t = 0.2\text{fs}$ ,  $V = 0$ , and  $\Delta x = \Delta y = 0.5\text{nm}$  ( $J = K = 120$ ). After 10 000 time steps the stub length is switched from  $L_1 = 32\text{nm}$  to  $L_2 = 40.5\text{nm}$ . In order to use a coarser time discretization (in spite of these oscillations), we consider the simple transformation

$$\varphi(x, y, t) := e^{-i\omega t}\psi(x, y, t), \quad (2.48)$$

with the dominant time frequency  $\omega = -\frac{E}{\hbar}$ .  $\varphi$  then satisfies the modified Schrödinger equation

$$i\hbar\varphi_t = -\frac{\hbar^2}{2m_*}(\varphi_{xx} + \varphi_{yy}) + (V - \omega\hbar)\varphi, \quad (2.49)$$

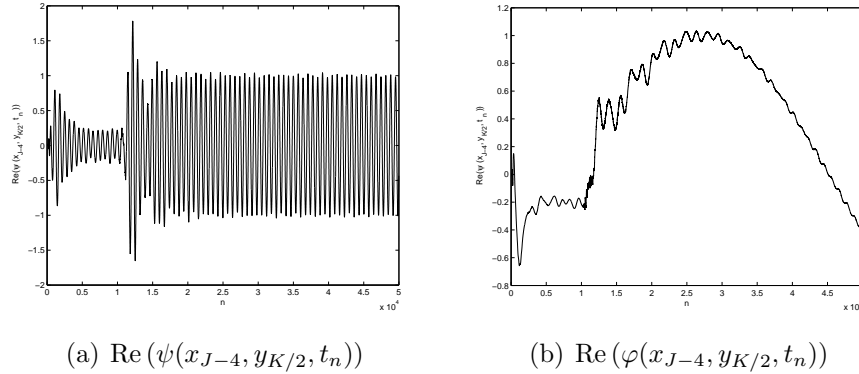


Figure 2.11: Time evolution of the real part to the solution of the Schrödinger equation in the T-shaped device at the one grid point  $(x_{J-4}, y_{K/2})$ . (a) shows  $\text{Re}(\psi(x_{J-4}, y_{K/2}, t_n))$  for time steps  $n = 1, \dots, 50\,000$  with  $V = 0$ . (b) shows the evolution of  $\text{Re}(\varphi(x_{J-4}, y_{K/2}, t_n))$  under the assumption  $V = -E$ . After 10 000 time steps the stub length is switched from  $L_1 = 32\text{nm}$  to  $L_2 = 40.5\text{nm}$ .

with  $\varphi^I = \psi^I$  and an incoming plane wave

$$\varphi^{Inc}(x = 0, y, t) = \sin\left(\frac{y\pi}{Y_1}\right). \quad (2.50)$$

As expected, its solution is much “smoother” in time (cf. Figure 2.11(b)). Hence, we expect that  $\varphi$  allows for a much more accurate numerical solution. To verify this claim numerically, we discretize both versions of the Schrödinger equation on the fixed time interval  $[0, 10\text{ps}]$ .  $\psi_1$  is obtained from (2.40) with the parameters  $N = 12\,500$ ,  $\Delta t = 0.8\text{fs}$  and  $V = 0$ .  $\psi_2(t_n) := e^{i\omega t_n}\varphi(t_n)$  is obtained from discretizing (2.49) with the parameters  $N = 12\,500$ ,  $\Delta t = 0.8\text{fs}$ , and  $V = -E$ . As an even more accurate reference solution we use  $\psi_3(t_n) := e^{i\omega t_n}\varphi(t_n)$  with the parameters  $N = 100\,000$ ,  $\Delta t = 0.1\text{fs}$ , and  $V = -E$ . In Figure 2.12 we show the evolution of the spatial-error-norms  $\|\psi_1(\cdot, \cdot, t_n) - \psi_3(\cdot, \cdot, t_{8n})\|_2$  and  $\|\psi_2(\cdot, \cdot, t_n) - \psi_3(\cdot, \cdot, t_{8n})\|_2$  for the time steps  $n = 0, \dots, 12\,500$ . At the time  $T = 2\text{ps}$  we switched the stub length from  $L_1 = 32\text{nm}$  to  $L_2 = 40.5\text{nm}$ . As expected, the function  $\psi_2$  is more accurate than function  $\psi_1$  with respect to the function  $\psi_3$ . Therefore, the transformed equation (2.49) shall be used for the subsequent simulations.

Figure 2.13 shows some temporal snapshots of the solution to the modified Schrödinger equation (2.49). And Figure 2.14 shows the corresponding longitudi-

## 2 DTBCs for the Schrödinger equation – a higher compact order scheme

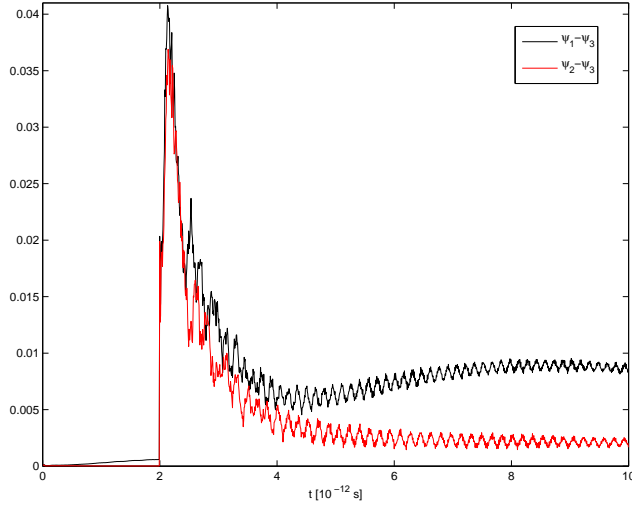


Figure 2.12: Time evolution of the spatial  $\ell^2$ -error of  $\psi_1$  and  $\psi_2$  w.r.t. the reference solution  $\psi_3$ ;  $\|\psi_1(t_n) - \psi_3(t_n)\|_2$  is plotted in black;  $\|\psi_2(t_n) - \psi_3(t_n)\|_2$  is plotted in red.

nal current density

$$j(x, t) = \int_0^{Y_3} J_x(x, y, t) dy, \quad (2.51)$$

where the  $x$ -component of the current density is defined as

$$J_x(x, y, t) = \frac{\hbar}{2m_*} \text{Im} \left( \psi(x, y, t) \frac{\partial}{\partial x} \bar{\psi}(x, y, t) \right).$$

In this simulation the stub length is first fixed to  $L_1 = 32\text{nm}$ . After about 2ps the solution reaches a steady state and the current inside the device is already almost constant in  $x$  at the low value  $0.03\text{nm}^2/\text{ps}$  (“off-state” of the waveguide, cf. 2.14(c)). Phenomenologically speaking, in this case only  $1\frac{1}{2}$  wave packets “fit” into the stub (cf. Figure 2.13(c)). Hence, they block the current flow through the waveguide. Then, at  $t = 2\text{ps}$  the stub is enlarged at once to  $L_2 = 40.5\text{nm}$ . After some transient phase, the solution converges to another steady state (“on-state” of the waveguide, cf. Figure 2.13(f), 2.14(f)). Here two wave packets “fit” into the stub. Hence, the current can flow almost unblocked through the device, so that the current is reaching an almost constant maximum level. Note that for a two dimensional channel of width 20nm (same as for the  $T$ -shaped geometry), but

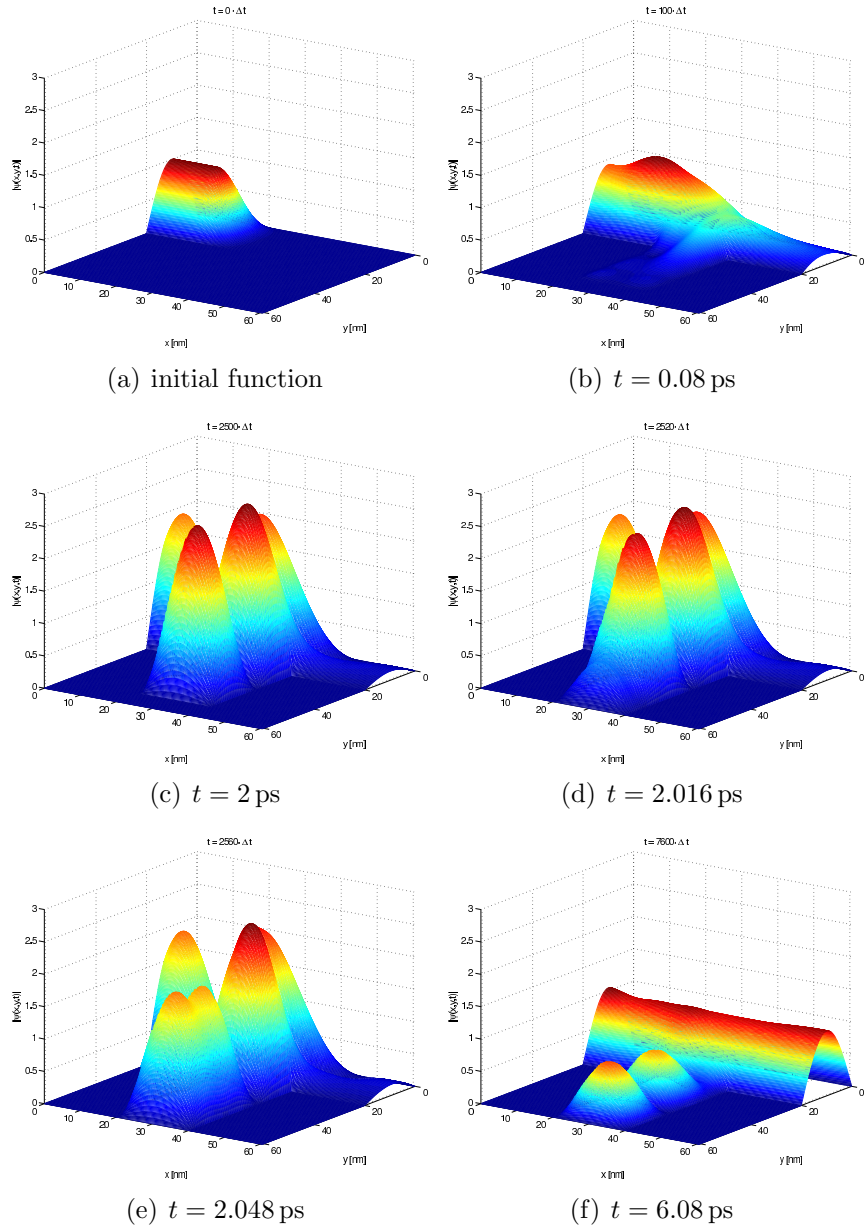


Figure 2.13: Absolute value of the solution  $\psi(x,y,t)$  of the time-dependent Schrödinger equation (2.40) on the T-shaped structure from Figure 2.9. The discretization parameters are chosen as  $\Delta x = \Delta y = 0.25\text{nm}$  ( $J = K = 242$ ),  $\Delta t = 0.8\text{fs}$ ,  $V = -E = -29.9\text{meV}$ ,  $m_* = 0.067m_0$ . (c) shows the steady state corresponding to the short stub with  $L_1 = 32\text{nm}$ . (f) is the steady state for the long stub with  $L = 40.5\text{nm}$ .

## 2 DTBCs for the Schrödinger equation – a higher compact order scheme

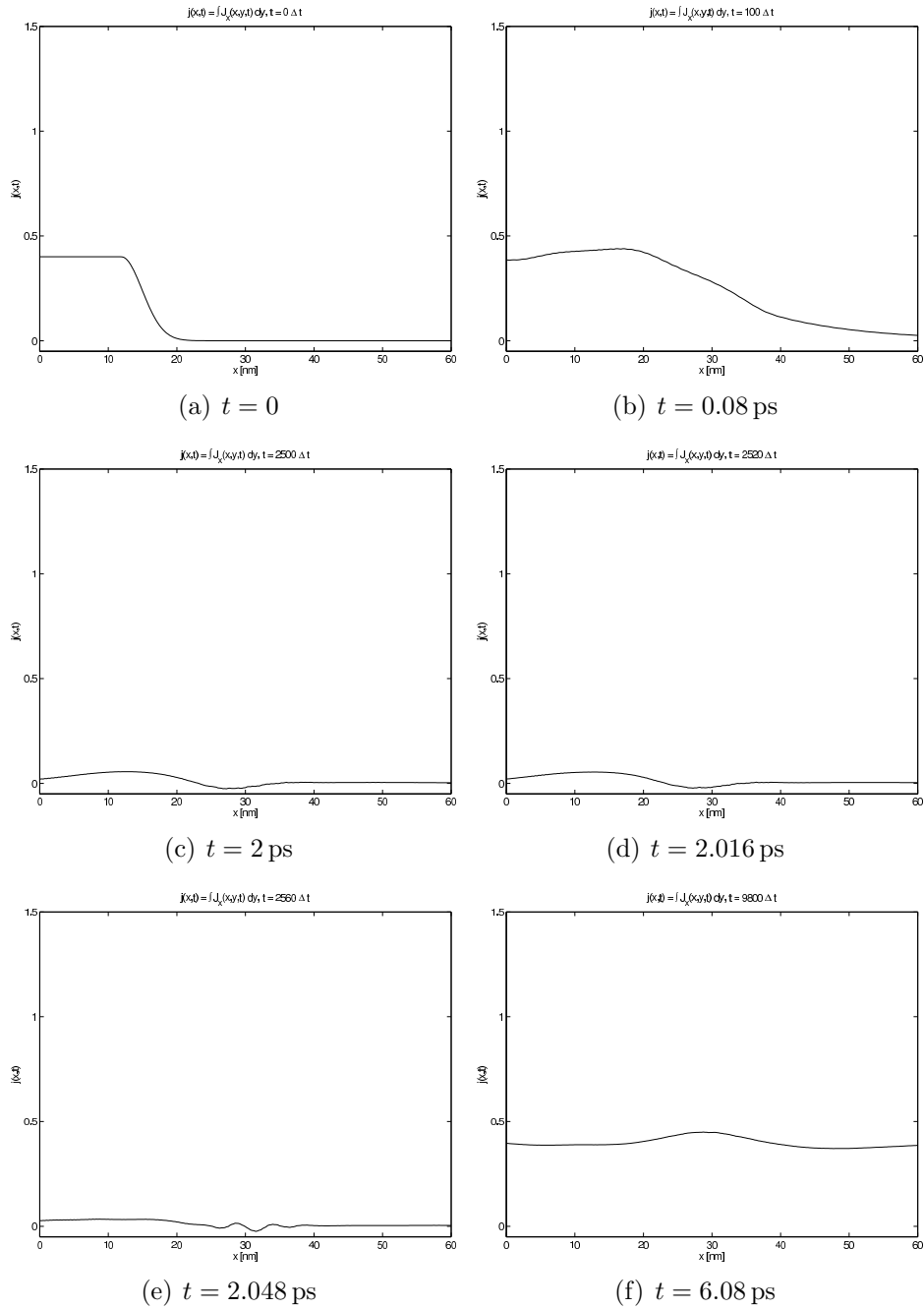


Figure 2.14: Current density  $j(x,t)$  (in  $\text{nm}^2/\text{ps}$ ) in the T-shaped device for the same example as in Figure 2.13. In (c) and (f) the current is (almost) constant in  $x$  – a requirement for a steady state.

without any barriers and stubs, and for the given energy inflow  $E = 29.9\text{meV}$ , the constant current  $j(x, t)$  equals  $0.4\text{nm}^2/\text{ps}$ .

## 2.6 Conclusion

We have generalized the fourth order *Numerov finite difference scheme* to the transient two dimensional Schrödinger equation and derived the corresponding *discrete transparent boundary conditions*. Its numerical efficiency is demonstrated in numerical tests on a rectangular geometry as well as for quantum waveguide simulations.

# Bibliography

- [AiYaMi93] K. Aihara, M. Yamamoto and T. Mizutani: *Three-terminal conductance modulation of a quantum interference device using a quantum wire with a stub structure*, Appl. Phys. Lett. **63** (1993) 3595–3597
- [AlRe02] I. Alonso-Mallo and N. Reguera: *Weak ill-posedness of spatial discretizations of absorbing boundary conditions for Schrödinger-type equations*, SIAM J. Numer. Anal. **40** (2002) 134–158
- [AlRe03] I. Alonso-Mallo and N. Reguera: *Discrete absorbing boundary conditions for Schrödinger-type equations, construction and error analysis*, SIAM J. Numer. Anal. **41** (2003) 1824–1850
- [AlRe04] I. Alonso-Mallo and N. Reguera: *Discrete Absorbing Boundary Conditions for Schrödinger-type equations. Practical Implementation*, Math. Comp. **73** (2004) 127–142
- [AABES07] X. Antoine, A. Arnold, C. Besse, M. Ehrhardt and A. Schädle: *A Review of Transparent and Artificial Boundary Conditions Techniques for Linear and Nonlinear Schrödinger Equations*, submitted to Appl. Numer. Math.
- [AnBe01] X. Antoine and C. Besse: *Construction, structure and asymptotic approximations of a microdifferential transparent boundary condition for the linear Schrödinger equation*, J. Math. Pures Appl. **80** (2001) 701–738
- [AnBeMo04] X. Antoine, C. Besse and V. Mouysset: *Numerical schemes for the simulation of the two-dimensional Schrödinger equation using non-reflecting boundary conditions*, Math. Comp. **73**, no. 248 (2004) 1779–1799
- [ASSHFLL96] J. Appenzeller, C. Schroer, T. Schäpers, A. v.d. Hart, A. Förster, B. Lengler and H. Lüth: *Electron interference in a T-shaped quantum transistor based on Schottky-gate technology*, Phys. Rev. B **53**, no. 15 (1996) 9959–9963
- [Ar98] A. Arnold: *Numerically absorbing boundary conditions for quantum evolution equations*, VLSI Design **6**, no. 1-4 (1998) 313–319

- [Ar01] A. Arnold: *Mathematical concepts of open quantum boundary conditions*, Transp. Theory Stat. Phys. **30**, no. 4-6 (2001) 561–584
- [ArEhSo03] A. Arnold, M. Ehrhardt and I. Sofronov: *Approximation, stability and fast calculation of non-local boundary conditions for the Schrödinger equation*, Commun. Mathematical Sciences **1**, no. 3 (2003) 501–556
- [ArSc07] A. Arnold and M. Schulte: *Transparent boundary conditions for quantum-waveguide simulations*, to appear in Mathematics and Computers in Simulation (2007), Proceedings of MATHMOD 2006, Vienna, Austria
- [AvKoSi00] G. Avdelas, A. Konguetsof and T.E. Simos: *A generalization of Numerov's method for the numerical solution of the Schrödinger equation in two dimensions*, Computers and Chemistry **24** (2000) 577–584
- [BaShMa02] W. Bao, J. Shi and P.A. Markowich: *On time-splitting spectral approximation for the Schrödinger equation in the semiclassical regime*, J. Comput. Phys. **175**, no. 2 (2002) 487–524
- [BaPo91] V.A. Basakov and A.V. Popov: *Implementation of transparent boundaries for numerical solution of the Schrödinger equation*, Wave Motion **14** (1991) 123–128
- [BeMePi05] N. Ben Abdallah, F. Méhats and O. Pinaud: *On an open transient Schrödinger-Poisson system*, Math. Models Methods Appl. Sci. **15**, no. 5 (2005) 667–688
- [BoDe06] A. Borzi and E. Decker: *Analysis of a leap-frog pseudospectral scheme for the Schrödinger equation*, J. Comp. Appl. Math. **193**, no. 1 (2006) 65–88
- [Bu97] L. Burgnies: *Mécanismes de conduction en régime ballistique dans les dispositifs électroniques quantiques*, Ph. D. thesis, Université des Sciences et Technologies de Lille (1997)
- [Co66] L. Collatz: *The numerical treatment of differential equations*, Springer Verlag, New York (1960)
- [Do51] H. Doerrie: *Unendliche Reihen*, Oldenbourg Verlag, München (1951)
- [EhAr01] M. Ehrhardt and A. Arnold: *Discrete Transparent Boundary Conditions for the Schrödinger Equation*, Revista di Matematica della Università di Parma **6**, no. 4 (2001) 57–108
- [EnMa77] B. Engquist and A. Majda: *Absorbing boundary conditions for the numerical simulation of waves*, Math. Comp. **31** (1977) 629–651

## Bibliography

---

- [EnMa79] B. Engquist and A. Majda: *Radiation boundary conditions for acoustic and elastic wave calculations* Comm. Pure Appl. Math. **32** (1979) 314–358
- [FeJi99] T. Fevens and H. Jiang: *Absorbing boundary conditions for the Schrödinger equation*, SIAM J. Sci. Comp. **21**, no. 1 (1999) 255–282
- [HePfSt07] B. Heubeck, C. Pflaum and G. Steinle: *New Finite Elements for Large-Scale Simulation of Optical Waves*, Preprint (2007)
- [JiLu02] G. Jing and M.S. Lundstrom: *A computational study of thin-body, double-gate, Schottky barrier MOSFETs*, IEEE Tran. on Elec. Dev. **49**, no. 11 (2002) 1897–1902
- [KaMoSi05] Z. Kalogiratou, T. Monovasilis and T. E. Simos: *Numerical solution of the two-dimensional time independent Schrödinger equation with Numerov-type methods*, J. Math. Chem. **37**, no. **3** (2005) 271–279
- [KoKo86] R. Kosloff and D. Kosloff: *Absorbing boundaries for wave propagation problems*, J. Comp. Phys. **63** (1986) 363–376
- [Ku92] J.-P. Kuska: *Absorbing boundary conditions for the Schrödinger equation on finite intervals*, Physical Review B **46**, no. 8 (1992) 5000–5003
- [Ma89] B. Mayfield: *Non-local boundary conditions for the Schrödinger equation*, Ph. D. thesis, University Rhode Island, Providence, RI (1989)
- [Mo04] C.A. Moyer: *Numerov extension of transparent boundary conditions for the Schrödinger equation in one dimension*, Am. J. Phys. **72**, no. 3 (2004) 351–358
- [Mo06] C.A. Moyer: *Numerical Solution of the Stationary State Schrödinger Equation Using Discrete Transparent Boundary Conditions*, Computing in Science and Engineering **8**, no. 4 (2006) 32–40
- [NeBa89] D. Neuhauser and M. Baer: *The time-dependent Schrödinger equation: Application of absorbing boundary conditions*, J. Chem. Phys. **90**, no. 8 (1989) 4351–4355
- [Pa82] J. S. Papadakis: *Impedance formulation of the bottom boundary condition for the parabolic equation model in underwater acoustics*, NORDA Parabolic Equation Workshop, NORDA Tech. Note **143** (1982)
- [Ra02] L. Ramdas Ram-Mohan: *Finite element and boundary element applications in quantum mechanics*, Oxford Texts in Applied and Engineering Mathematics **5**, Oxford Univ. Press, (2002)

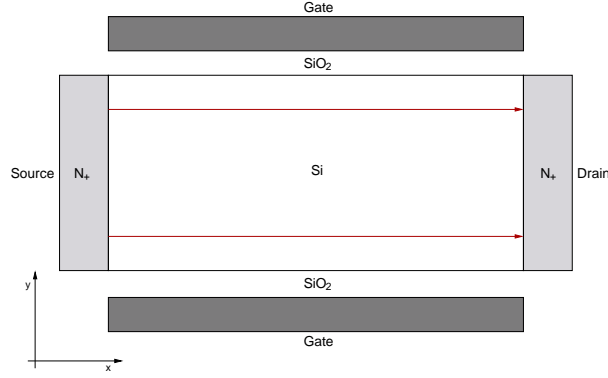
- [Sc02] A. Schädle: *Non-reflecting boundary conditions for the two dimensional Schrödinger equation*, Wave Motion **35** (2002) 181–188
- [Sh91] T. Shibata: *Absorbing boundary conditions for the finite-difference time-domain calculation of the one-dimensional Schrödinger equation*, Physical Review B **43**, no. 8 (1991) 6760–6763
- [St04] J. C. Strikwerda: *Finite Difference Schemes And Partial Differential Equations*, Society for Industrial and Applied Mathematics (2004)
- [StBu90] J. Stoer and R. Bulirsch: *Numerische Mathematik 2*, Springer Verlag Berlin (1990)
- [Sz04a] J. Szeftel: *Design of Absorbing Boundary Conditions for Schrödinger equations in  $\mathbb{R}^d$* , SIAM J. Numer. Anal. **42**, no. 4 (2004) 1527–1551
- [Sz04b] J. Szeftel: *Refléxion des singularités pour l'équation de Schrödinger*, Comm. Partial Differential Equations **29**, no. 5-6 (2004) 707–761
- [Sz75] G. Szegő: *Orthogonal Polynomials*, 4<sup>th</sup> edition, Vol. XXIII. AMS (1975)
- [WaPo04] J. Wang, E. Polizzi and M. Lundstrom: *A Three-Dimensional Quantum Simulation of Silicon Nanowire Transistors with the Effective-Mass Approximation*, J. Appl. Phys. **96**, no. 4 (2004) 2192–2203

# 3 Transient quantum simulations for the double gate MOSFET

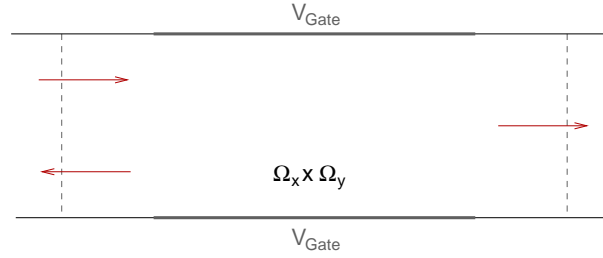
In this section we will extend the DTBCs for the 2D time-dependent Schrödinger equation to more arbitrary geometries and potentials. This gives a more accurate physical model for quantum transport in nanostructures. For the modelling of ballistic quantum transport devices we furthermore obtain a self-consistent solution between the Schrödinger and the Poisson equation. We propose a very efficient *subband decomposition algorithm* and show numerical results for simulations of the Schrödinger-Poisson system. With the new method proposed here it is possible to simulate the *double gate metal oxide semiconductor field-effect transistor (double gate MOSFET or DGMOS)*, which is today's dominant device in integrated circuits.

## 3.1 Introduction

Today's semiconductor devices like transistors and nanoscale split-gate devices are rapidly shrinking in their size. In this context, modeling and numerical simulations play an important role in the development and design of new devices. We focus on devices with ballistic electron transport, such as electron quantum waveguide devices. Their functionality depends on the formation of a 2D electron gas and on wave interference effects (cf. [FeGo97], e.g.). Speaking of ballistic transport means that electrons are assumed to not suffer any collision during their transit through the device (e.g. high-purity materials and at low temperatures). A schematic view of such a device, a DGMOS, is shown in Figure 3.1(a). At the gates there is an applied external potential and the electron transport takes place from source to drain. We consider the *effective mass approximation*, where the mass  $m_*$  is assumed to be constant in homogenized parts of the device. The different materials (e.g. Si, SiO<sub>2</sub>) have different effective masses. We simplify this model like it is presented in Figure 3.1(b), where only one effective mass is introduced and external potentials  $V_{Gate}$  could be applied at the gates. But regarding different materials and therefore different effective masses won't change the derivation of the open boundary conditions and the model in principle. The electron flow through the device is modeled by a superposition of incoming plane waves.



(a) Schematic view of a DG MOS. The electron transport takes place from source to drain in  $x$ -direction (red arrows). An external potential is applied at the gates.



(b) Simplified model of a DG MOS

Figure 3.1: Schematic view and simplified model of a DG MOS.

A suitable way to simulate the electron transport through a quantum waveguide in good approximation is given by the 3D time-dependent Schrödinger equation coupled with the Poisson equation. The electrons in the device are in a mixed state with given statistics, where each pure state  $\Psi_{\lambda_{x,y,z}}$  is a solution of the Schrödinger equation

$$i\hbar \frac{\partial \Psi_{\lambda_{x,y,z}}(x, y, z, t)}{\partial t} = -\frac{\hbar^2}{2m_*} \Delta \Psi_{\lambda_{x,y,z}}(x, y, z, t) + V(x, y, z, t) \Psi_{\lambda_{x,y,z}}(x, y, z, t), \quad (x, y, z) \in \mathbb{R}^3, t > 0. \quad (3.1)$$

The complex valued wave function  $\Psi_{\lambda_{x,y,z}}$  depends on a continuous wavenumber index  $\lambda_{x,y,z} \in \Lambda \subseteq \mathbb{R}$ . The potential  $V = V_e + V_s$  splits into a given, external part  $V_e$  and a self-consistent part  $V_s$  caused by electrostatic interaction of the electrons.

### 3 Transient quantum simulations for the double gate MOSFET

---

The self-consistent potential solves the Poisson equation

$$-\Delta V_s(x, y, z, t) = n(x, y, z, t) := \int_{\Lambda} |\Psi_{\lambda_{x,y,z}}(x, y, z, t)|^2 d\lambda_{x,y,z},$$

$$(x, y, z) \in \mathbb{R}^3, t > 0. \quad (3.2)$$

The nonlinear Schrödinger-Poisson system (3.1), (3.2) has been widely studied analytically in whole space settings (e.g. [Ca89], [Ca97], [IIZwLa94]). For numerical simulations we have to choose a bounded domain  $\Omega \subset \mathbb{R}^3$ , in which we solve the system (3.1), (3.2).  $\Omega$  is the active region of the device. Our aim is to use the highly efficient algorithm of the *subband decomposition* for solving the coupled Schrödinger-Poisson system. Furthermore we want to derive discrete open boundary conditions for the Schrödinger equation (3.1), which is nonlinearly coupled to the Poisson equation (3.2) inside the active region, in case of a continuous particle injection into the device. In the analytical case this has been studied in 1D in [BePi02], [Pi02] and in the 2D, 3D case in [BeMePi05].

## 3.2 Overview of the analytical model

Let  $\Omega = \Omega_x \times \Omega_y \times \Omega_z$  be a 3D box, as it is shown in Figure 3.2. The model proposed here is not a fully 3D model with open boundary conditions. The  $z$ -direction is assumed to be the infinite direction, where the wave functions are defined as plane waves. Furthermore the direction  $x \in \Omega_x = (0, X)$  denotes the transport direction, where we shall obtain open boundaries at  $x = 0$  and  $x = X$ .  $y \in \Omega_y = (0, Y)$  is a confined direction with closed boundary conditions (e.g. zero Dirichlet boundary conditions at  $y = 0$  and  $y = Y$ ). Therefore we let the potential  $V$  be independent of  $z \in \Omega_z = (-\infty, \infty)$ . We assume that the system is invariant w.r.t. the  $z$ -direction such that the wave function is a plane wave in this direction. The full wave function  $\Psi_{\lambda_{x,y,z}}$  can be separated as

$$\Psi_{\lambda_{x,y,z}}(x, y, z, t) = \vartheta_{E_z, k_z}(z, t) \psi_{\lambda_{x,y}}(x, y, t), \quad (x, y) \in \Omega_x \times \Omega_y, z \in \Omega_z, t > 0,$$

with a complex-valued plane wave  $\vartheta_{E_z, k_z} : \mathbb{R} \times \mathbb{R}^+ \rightarrow \mathbb{C}$ , the energy

$$E_z = \frac{\hbar^2 k_z^2}{2m_*}, \quad k_z \in \mathbb{R},$$

and  $\Psi_{\lambda_{x,y,z}}$  has the energy  $E = E_z + E_{x,y}$ . This results from the translation invariance of the 3D problem in  $z$ -direction.  $E_{x,y}$  denotes the energy of the 2D wave function  $\psi_{\lambda_{x,y}} : \mathbb{R}^2 \times \mathbb{R}^+ \rightarrow \mathbb{C}$  and  $\lambda_{x,y}$  the real-valued wavenumbers. The domain  $\Omega_x \times \Omega_y$  is considered to be the active region of the device. Electrons

## 3.2 Overview of the analytical model

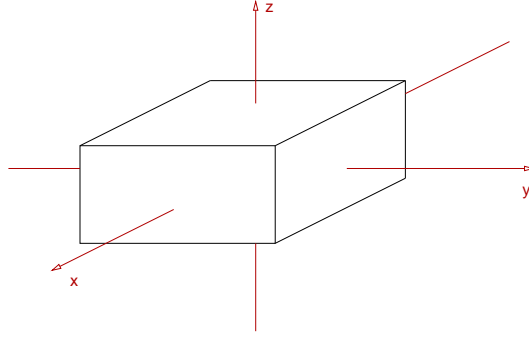


Figure 3.2: Bounded domain  $\Omega \subset \mathbb{R}^3$ .

are fed into the device by a superposition of plane waves  $\psi_{\lambda_{x,y}}^{inc}(x, y, t)$ . The wave function  $\psi_{\lambda_{x,y}}$  solves the 2D time-dependent Schrödinger equation

$$\begin{aligned}
 i\hbar \frac{\partial \psi_{\lambda_{x,y}}}{\partial t}(x, y, t) &= -\frac{\hbar^2}{2m_*} \Delta \psi_{\lambda_{x,y}}(x, y, t) + V(x, y, t) \psi_{\lambda_{x,y}}(x, y, t), \\
 &\quad (x, y) \in \Omega_x \times \Omega_y, t > 0, \\
 \psi_{\lambda_{x,y}}(x, 0, t) &= \psi_{\lambda_{x,y}}(x, Y, t) = 0, \quad x \in \Omega_x, t > 0, \\
 V(x, y, t) &= V_e(x, y, t) + V_s(x, y, t), \quad (x, y) \in \Omega_x \times \Omega_y, t > 0 \quad (3.3)
 \end{aligned}$$

with open boundary conditions at  $x = 0, x = X$ . Inside the active region we suppose a self-consistent potential. In the previous analysis in §1 and §2 we neglected the self-consistent part of the potential and assumed the external potential to be constant in the left and right leads of the waveguide, i.e. for  $x \leq 0, x \geq X$ . Here we relax these assumptions and allow external potentials

$$V_e(x, y, t) = \begin{cases} \tilde{V}_e(x, y, t) & : (x, y) \in \Omega_x \times \Omega_y, t > 0, \\ V_0(y) + V^1(t) & : x \leq 0, y \in \Omega_y, t > 0, \\ V_X(y) + V^2(t) & : x \geq X, y \in \Omega_y, t > 0, \\ \infty & : x \in \Omega_x, y \leq 0 \text{ or } y \geq Y, t > 0 \end{cases} \quad (3.4)$$

with  $V_e \in L^\infty(\Omega_x \times \Omega_y \times \mathbb{R}^+)$ . The  $y$ -dependence of the potential in the exterior domains allows much more realistic models. With this choice for  $V_e$  it is possible to build waveguides of different shapes by applying external potentials. In former models the walls of electronic devices were realized by zero Dirichlet boundary conditions in the confined direction. Due to the DTBCs it was necessary that the computational domain had to end in rectangular leads. The potential in the outer domains was assumed to be constant, in particular on the lines  $x = 0$  and  $x = X$ .

### 3 Transient quantum simulations for the double gate MOSFET

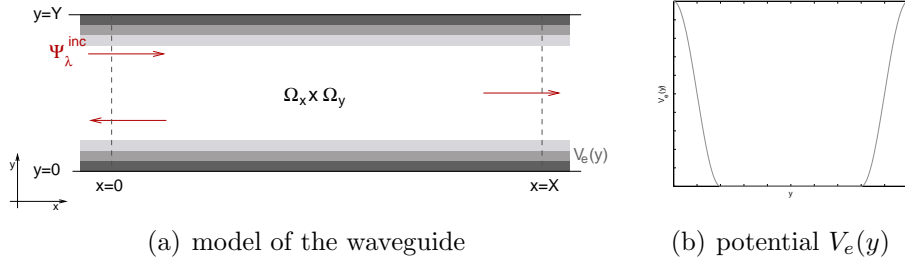


Figure 3.3: More realistic model of a quantum waveguide. In (a) we plotted a part of the channel  $\mathbb{R} \times (0, Y)$ . A potential  $V_e(y)$ , which acts like a confinement, is applied in  $y$ -direction. The grey-coloured domains illustrate the external potential in this direction. Dark colour values correspond to high values for the potential. A cross-section of an example of such a potential is presented in (b).

Hence it was not possible to shape the full geometry of a device by  $y$ -dependent external potentials with the methods presented in §1 and §2. An example of a more realistic model of a quantum waveguide channel built by applying a  $y$ -dependent potential is shown in Figure 3.3. With an external potential which is increasing for  $y \rightarrow 0$  and  $y \rightarrow Y$  we obtain a potential that acts like a barrier at the channel walls  $y = 0$  and  $y = Y$ . This is a more natural model since industrial devices are also built by applied potentials. We will give also some numerical examples for the choice of  $V_e$  in §3.4.1.

**Remark 3.1** *Without loss of generality we can drop the time-dependence  $V^1(t)$ ,  $V^2(t)$  of the potential in (3.4) in the outer domains for the further calculations. We introduce the transformation*

$$\tilde{\psi}_{\lambda,x,y}(x, y, t) = e^{-\frac{i}{\hbar} \int_0^t V^1(\tau) d\tau} \psi_{\lambda,x,y}(x, y, t) \quad (3.5)$$

for the left outer domain  $x \leq 0$  (and analogously for  $x \geq X$ ). Then,  $\tilde{\psi}_{\lambda,x,y}$  fulfills the modified Schrödinger equation

$$i\hbar \frac{\partial \tilde{\psi}_{\lambda,x,y}}{\partial t}(x, y, t) = -\frac{\hbar^2}{2m_*} \Delta \tilde{\psi}_{\lambda,x,y}(x, y, t) + V_0(y) \tilde{\psi}_{\lambda,x,y}(x, y, t), \quad (x, y) \in \Omega_x \times \Omega_y, t > 0 \quad (3.6)$$

without any time-dependent potential.

Hence, we consider in the following analysis only given external potentials  $V_0(y)$ ,  $x \leq 0$ ,  $V_X(y)$ ,  $x \geq X$  depending on  $y \in \Omega_y$  in the outer domains. In the numerical simulations we assume also time-dependent external potentials in the outer

## 3.2 Overview of the analytical model

---

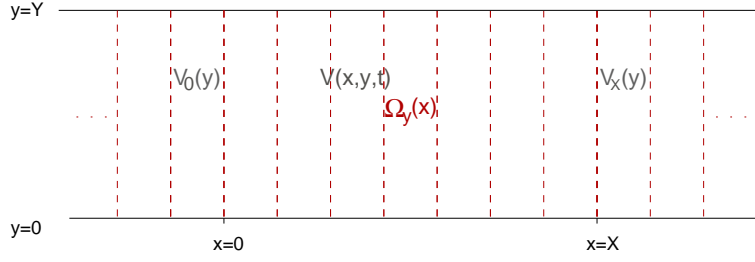


Figure 3.4: The computational domain  $\Omega_x \times \Omega_y$  is divided into slices  $\Omega_y(x)$ . Inside  $\Omega_x \times \Omega_y$  the external potential is a function of the variables  $x, y, t$ ; in the leads  $x \leq 0, x \geq X$  it only depends on  $y$ .

domains. The following calculations are only made for the left outer domain, the case of the right outer domain is completely analogous.

### 3.2.1 Subband decomposition of the analytical 2D Schrödinger equation

The idea of the subband decomposition is to reduce the dimension of the 2D time-dependent Schrödinger equations (3.3) and (3.6), firstly on the infinite channel  $\mathbb{R} \times \Omega_y$ , to 1D by projecting the solution onto the Schrödinger eigenfunctions in  $y$ -direction. This approach was presented in [Po05] for the stationary Schrödinger equation. Therefore the domain  $\Omega_x \times \Omega_y$  is divided into slices  $\Omega_y(x)$  along the transport direction like shown in Figure 3.4. The potential located in the active domain is supposed to be a function of  $x, y, t$ . Outside the active region, for  $x \leq 0$  and  $x \geq X$ , the external potential (and hence also the self-consistent) depends only on the confined direction  $y$ . On each slice  $\Omega_y(x)$  we calculate the eigenfunctions  $\chi_m(x, y, t)$  as a solution of the 1D stationary Schrödinger equation with Dirichlet boundary conditions:

$$\begin{aligned}
 -\frac{\hbar^2}{2m_*} \frac{\partial^2}{\partial y^2} \chi_m(x, y, t) + V(x, y, t) \chi_m(x, y, t) &= \epsilon_m(x, t) \chi_m(x, y, t), \\
 & \quad (x, y) \in \Omega_y(x), t > 0, m \in \mathbb{N}, \\
 \chi_m(x, 0, t) = \chi_m(x, Y, t) &= 0, \quad t > 0, x \in \mathbb{R}, m \in \mathbb{N}.
 \end{aligned}$$

We normalize the eigenmodes by

$$\int_0^Y \chi_m(x, y, t) \chi_q(x, y, t) dy = \delta_{m,q}, \quad \forall q, m \in \mathbb{N}, x \in \mathbb{R}, t > 0. \quad (3.7)$$

### 3 Transient quantum simulations for the double gate MOSFET

The wave function  $\psi_{\lambda_{x,y}}(x, y, t)$  can be uniquely decomposed in terms of the eigenfunctions

$$\psi_{\lambda_{x,y}}(x, y, t) = \sum_{m=1}^{\infty} \varphi_{\lambda_{x,y},m}(x, t) \chi_m(x, y, t), \quad (x, y) \in \Omega_y(x), t > 0 \quad (3.8)$$

with

$$\varphi_{\lambda_{x,y},m}(x, t) = \langle \psi_{\lambda_{x,y}}(x, y, t), \chi_m(x, y, t) \rangle := \int_0^Y \psi_{\lambda_{x,y}}(x, y, t) \chi_m(x, y, t) dy.$$

Inserting representation (3.8) into equation (3.3), multiplying with  $\chi_q(x, y, t)$ , integrating over  $\Omega_y$  and using the orthonormality (3.7) yields the coupled 1D equations

$$\begin{aligned} i\hbar \frac{\partial}{\partial t} \varphi_{\lambda_{x,y},m}(x, t) &= -\frac{\hbar^2}{2m_*} \frac{\partial^2}{\partial x^2} \varphi_{\lambda_{x,y},m}(x, t) + \epsilon_m(x, t) \varphi_{\lambda_{x,y},m}(x, t) \\ &\quad - i\hbar \sum_{q=1}^{\infty} \left\langle \frac{\partial}{\partial t} \chi_q(x, y, t), \chi_m(x, y, t) \right\rangle \varphi_{\lambda_{x,y},q}(x, t) \\ &\quad - \frac{\hbar^2}{m_*} \sum_{q=1}^{\infty} \left\langle \frac{\partial}{\partial x} \chi_q(x, y, t), \chi_m(x, y, t) \right\rangle \frac{\partial}{\partial x} \varphi_{\lambda_{x,y},q}(x, t) \\ &\quad - \frac{\hbar^2}{2m_*} \sum_{q=1}^{\infty} \left\langle \frac{\partial^2}{\partial x^2} \chi_q(x, y, t), \chi_m(x, y, t) \right\rangle \varphi_{\lambda_{x,y},q}(x, t), \end{aligned} \quad x \in \mathbb{R}, t > 0, m \in \mathbb{N}. \quad (3.9)$$

The subband decomposition algorithm follows by truncating the sums  $\sum_{q=1}^{\infty}$  in (3.9) to  $\sum_{q=1}^M$  for a fixed number  $M \in \mathbb{N}$  and solving the coupled 1D equations (3.9) for  $m = 1, \dots, M$  instead of solving the 2D Schrödinger equation (3.3). Additionally we will solve uncoupled 1D equations (cf. §3.3).

**Remark 3.2** *On the leads  $x \leq 0$ ,  $x \geq X$  of the waveguide we calculate eigenfunctions  $\chi_m$  and eigenvalues  $\epsilon_m$  which do not depend on the variables  $t, x$ . They are different in both outer domains, since we assume different  $y$ -dependent potentials there. The coupling terms vanish in (3.9) for  $x \leq 0$ ,  $x \geq X$ .*

#### 3.2.2 Adding the self-consistent potential

The given external potentials  $V_0(y)$ ,  $x \leq 0$ ,  $V_X(y)$ ,  $x \geq X$  cause self-consistent potentials  $V_{0,s}(y)$ ,  $V_{X,s}(y)$ ,  $y \in \Omega_y$  in each outer domain which are constant in time and can be obtained by solving the 1D Poisson equation

$$\begin{aligned} -\frac{\partial^2}{\partial y^2} V_{0,s}(y) &= n_{1D}(y) - n_D, \quad y \in \Omega_y \\ \frac{\partial}{\partial y} V_{0,s}(0) &= \frac{\partial}{\partial y} V_{0,s}(Y) = 0 \end{aligned} \quad (3.10)$$

### 3.2 Overview of the analytical model

with a given constant doping profile  $n_D$  for each outer domain. In this 1D case the electron density  $n_{1D}$  takes the form

$$n_{1D}(y) = \sum_m \int_{-\infty}^{\infty} \int_{-\infty}^{\infty} |\psi_{\lambda_{x,y}}(0, y, 0)|^2 f(E_m(k_x, k_z) - \mu) \frac{dk_x dk_z}{2\pi}, \quad (3.11)$$

where  $\mu$  denotes the unknown chemical potential in the actual lead (here  $x \leq 0$ ) of the waveguide at equilibrium.  $f$  is the given statistical distribution, e.g. the Boltzmann distribution

$$f_B(E) = e^{-\frac{E}{k_B T}}, \quad E \in \mathbb{R}$$

or the Fermi-Dirac distribution

$$f_{FD}(E) = \frac{1}{1 + e^{\frac{E}{k_B T}}}, \quad E \in \mathbb{R}$$

with the Boltzmann's constant  $k_B$  and the temperature  $T$ .  $\psi_{\lambda_{x,y}}(0, y, 0)$  corresponds to the initial wave function at  $x = 0$ . Since we inject plane waves into the waveguide, (3.11) can be simplified (with (3.8)) to

$$n_{1D}(y) = \sum_m |\chi_m(0, y, 0)|^2 \int_{-\infty}^{\infty} \int_{-\infty}^{\infty} f(E_m(k_x, k_z) - \mu) \frac{dk_x dk_z}{2\pi}. \quad (3.12)$$

The energy  $E_m(k_x, k_z)$  describes the energy  $\epsilon_m(x)$  of the injected mode (at  $x = 0$  for the left exterior domain) plus the energies given by the dispersion relations for wavenumbers  $k_x, k_z$ :

$$E_m(k_x, k_z) = \epsilon_m(0) + \frac{\hbar^2 k_x^2}{2m_*} + \frac{\hbar^2 k_z^2}{2m_*}, \quad m \in \mathbb{N}, k_x, k_z \in \mathbb{R}.$$

In case of Boltzmann statistics, i.e.  $f(E) = f_B(E)$ , the integral appearing in (3.12) can be calculated analytically and we obtain

$$n_{1D}(y) = \frac{k_B T m_*}{\hbar^2} \sum_m |\chi_m(0, y, 0)|^2 e^{-\frac{\epsilon_m(0) - \mu}{k_B T}}, \quad y \in \Omega_y. \quad (3.13)$$

The chemical potential  $\mu$  will also appear in the Poisson equation in the active domain  $\Omega_x \times \Omega_y$  and has to be calculated such that

$$\int_0^Y (n_{1D}(y) - n_D) dy = 0. \quad (3.14)$$

### 3 Transient quantum simulations for the double gate MOSFET

---

With this information the electron density  $n_{1D}(y)$  can be computed and the Poisson equation (3.10) has a unique solution. The self-consistent potential  $V_s$  inside the active region  $\Omega_x \times \Omega_y$  satisfies the 2D Poisson equation

$$\begin{aligned} -\Delta V_s(x, y, t) &= n_{2D}(x, y, t) - n_D, & (x, y) \in \Omega_x \times \Omega_y, t > 0, \\ \frac{\partial}{\partial y} V_s(x, 0, t) &= \frac{\partial}{\partial y} V_s(x, Y, t) = 0, & x \in \Omega_x, t > 0, \\ V_s(0, y, t) &= V_{0,s}(y), V_s(X, y, t) = V_{X,s}(y), & y \in \Omega_y, t > 0 \end{aligned} \quad (3.15)$$

with the 2D electron density (cf. [Po02])

$$n_{2D}(x, y, t) = \sum_m \int_{\mathbb{R}^2} |\psi_{\lambda_{x,y}}(x, y, t)|^2 f \left( \epsilon_m(0) + \frac{\hbar^2 k_x^2}{2m_*} + \frac{\hbar^2 k_z^2}{2m_*} - \mu \right) \frac{dk_x dk_z}{2\pi},$$

where  $f$  denotes again the statistical distribution and  $n_D$  the given constant doping profile. The solutions  $\psi_{\lambda_{x,y}}(x, y, t)$  of the 2D time-dependent Schrödinger equation depend on the continuous wavenumber  $k_x$  and have to be calculated for all  $k_x \in \mathbb{R}$ . Since the incoming functions do not depend on  $k_z$  the electron density can be simplified in case of Boltzmann statistics to

$$\begin{aligned} n_{2D}(x, y, t) &= \sum_m \int_{-\infty}^{\infty} \int_{-\infty}^{\infty} |\psi_{\lambda_{x,y}}(x, y, t)|^2 e^{\left( \epsilon_m(0) + \frac{\hbar^2 k_x^2}{2m_*} + \frac{\hbar^2 k_z^2}{2m_*} - \mu \right) / (k_B T)} \frac{dk_x dk_z}{2\pi} \\ &= \frac{\sqrt{k_B T}}{4\hbar\sqrt{\pi}} \sum_m e^{-\frac{\epsilon_m(0) - \mu}{k_B T}} \int_{-\infty}^{\infty} |\psi_{\lambda_{x,y}}(x, y, t)|^2 e^{-\frac{\hbar^2 k_x^2}{2m_* k_B T}} dk_x, \\ & \hspace{15em} (x, y) \in \Omega_x \times \Omega_y, t > 0 \end{aligned} \quad (3.16)$$

with  $\mu$  given indirectly by the equality (3.14).

**Remark 3.3** *In practice  $\psi_{\lambda_{x,y}}(x, y, t)$  and the integral (3.16) cannot be calculated analytically for all real values of  $k_x$ . But  $\psi_{\lambda_{x,y}}(x, y, t)$  is bounded w.r.t.  $k_x$  and  $\exp\left(-\frac{\hbar^2 k_x^2}{2m_* k_B T}\right)$  tends to zero very fast with  $k_x \rightarrow \infty$ , such that the integral over  $\mathbb{R}$  can be approximated well by a definite integral over  $[-c, c]$  with some  $c \in \mathbb{R}^+$ .*

In the following section we will derive a discrete system corresponding to the analytical model of the Schrödinger-Poisson system (3.3), (3.15) with suitable boundary conditions and use the subband decomposition algorithm for the efficient computation of the discrete solution. Numerical results on 2D domains  $\Omega_x \times \Omega_y$  will be presented in §3.4.

### 3.3 Discretization of the Schrödinger-Poisson system

For the derivation of a discrete model of the Schrödinger-Poisson system on the channel  $\Omega_x \times \Omega_y$  with DTBCs in transport direction we first discretize the Schrödinger equation (3.3), derive DTBCs which take the given potential (3.4) into account and use the subband decomposition for solving the discrete Schrödinger equation. Afterwards we extend the model by including the self-consistence of the potential as a solution to the discretized Poisson equation.

#### 3.3.1 Extended DTBCs for the discretized Schrödinger equation

We discretize the Schrödinger equation (3.3) again with the Crank-Nicolson standard five-point finite difference scheme with the equidistant grid points  $x_j = j\Delta x$ ,  $j \in \mathbb{Z}$ ,  $y_k = k\Delta y$ ,  $k = 0, \dots, K$ ,  $t_n = n\Delta t$ ,  $n \in \mathbb{N}$  with  $X = J\Delta x$ ,  $Y = K\Delta y$  like mentioned in §1.2 and obtain for  $\psi_{j,k}^n \sim \psi_{\lambda_{x,y}}(x_j, y_k, t_n)$  the difference equations

$$\begin{aligned} \frac{i\hbar}{\Delta t} (\psi_{j,k}^{n+1} - \psi_{j,k}^n) &= -\frac{\hbar^2}{2m_*\Delta x^2} (\psi_{j-1,k}^{n+1/2} - 2\psi_{j,k}^{n+1/2} + \psi_{j+1,k}^{n+1/2}) \\ &\quad - \frac{\hbar^2}{2m_*\Delta y^2} (\psi_{j,k-1}^{n+1/2} - 2\psi_{j,k}^{n+1/2} + \psi_{j,k+1}^{n+1/2}) + V_{j,k}^{n+1/2}\psi_{j,k}^{n+1/2} \end{aligned} \quad (3.17)$$

for  $j \in \mathbb{Z}$ ,  $k = 0, \dots, K$ ,  $n \in \mathbb{N}_0$  with the abbreviations

$$\begin{aligned} \psi_{j,k}^{n+1/2} &= \frac{1}{2} (\psi_{j,k}^{n+1} + \psi_{j,k}^n), \\ V_{j,k}^{n+1/2} &= V(x_j, y_k, t_{n+1/2}), \end{aligned}$$

and  $V(x, y, t) = V_e(x, y, t)$  from (3.4) with  $V^1(t) = V^2(t) = 0$  (see Remark 3.1). The potential reduces to  $V_{j,k}^{n+1/2} = V_k$  for all  $k = 0, \dots, K$ ,  $n \geq 1$  in the outer leads  $j \leq 0$ ,  $j \geq J$  of the waveguide. For each interior grid point  $x_j$  and each time step  $n$  we solve the eigenvalue problems

$$\begin{aligned} -\frac{1}{2\Delta y^2} (\chi_{j,k-1}^{m,n+1/2} - 2\chi_{j,k}^{m,n+1/2} + \chi_{j,k+1}^{m,n+1/2}) + V_{j,k}^{n+1/2}\chi_{j,k}^{m,n+1/2} \\ = \epsilon_j^{m,n+1/2}\chi_{j,k}^{m,n+1/2}, \quad 0 \leq j \leq J, 1 \leq k, m \leq K-1, n \in \mathbb{N}_0, \\ \chi_{j,0}^{m,n+1/2} = \chi_{j,K}^{m,n+1/2} = 0, \quad 0 \leq j \leq J, 1 \leq m \leq K-1, n \in \mathbb{N}_0, \end{aligned} \quad (3.18)$$

### 3 Transient quantum simulations for the double gate MOSFET

---

and normalize the eigenmodes:

$$\Delta y \sum_{k=1}^{K-1} \left| \chi_{j,k}^{m,n+1/2} \right|^2 = 1, \quad 0 \leq j \leq J, 1 \leq m \leq K-1, n \in \mathbb{N}_0.$$

**Remark 3.4** *To avoid numerical errors we need to be sure, that the eigenfunctions have the same orientation. Therefore we define the discrete scalar product*

$$\langle g_k, f_k \rangle := \Delta y \sum_{k=1}^{K-1} g_k f_k$$

*w.r.t. the discrete direction  $k$  for discrete functions  $f, g \in \mathbb{R}^{K+1}$  with  $g_0 = g_K = f_0 = f_K = 0$ . We calculate the sign of  $\langle \chi_{j,k}^{m,1/2}, \chi_{j+1,k}^{m,1/2} \rangle$  for all modes  $m$  and multiply  $\chi_{j+1,k}^{m,1/2}$  for all  $k = 1, \dots, K-1$  with it for all  $j = 0, \dots, J$ . Hence it is sure, that the eigenmodes  $\chi_{j,k}^{m,1/2}$  at the line  $x_j$  and the following eigenmodes  $\chi_{j+1,k}^{m,1/2}$  at the line  $x_{j+1}$  have the same sign. In all time steps we orientate the eigenmode of the first line  $\chi_{0,k}^{m,n+3/2}$  at the new time step  $n+1$  w.r.t. the eigenmode of the first line  $\chi_{0,k}^{m,n+1/2}$  at the old time step  $n$  and then adjust the eigenmodes of lines  $j \geq 1$  w.r.t.  $\chi_{0,k}^{m,n+3/2}$ .*

**Remark 3.5** *In [Po05] the author points out that if the silicon layer of the DG-MOS is larger than  $\sim 10\text{nm}$ , then the first two modes  $\chi_{j,k}^{1,n+1/2}, \chi_{j,k}^{2,n+1/2}$  will have very close energies  $\epsilon_j^{1,n+1/2}, \epsilon_j^{2,n+1/2}$ . Due to rounding errors it may be the case that the energies are equal and hence the associated eigenspace is computed as two dimensional, which is not correct. We calculate the eigenfunctions in each line  $x_j$  independently of the neighbour line  $x_{j+1}$ . Computing an energy eigenvalue as a double eigenvalue leads to the regularity of  $\text{span} \left\{ \chi_{j,k}^{1,n+1/2}, \chi_{j,k}^{2,n+1/2} \right\}$  in  $x$ -direction, but the eigenfunctions may be not smooth in  $x$ . Let the eigenmodes  $\chi_{j,k}^{1,n+1/2}, \chi_{j,k}^{2,n+1/2}$  be computed for the  $j$ -th line. The “wrong” eigenmodes computed in the neighbour line  $j+1$  are notated by  $\hat{\chi}_{j+1,k}^{1,n+1/2}, \hat{\chi}_{j+1,k}^{2,n+1/2}$ . They are going to be corrected by the orthogonalization due to the rotation*

$$\begin{pmatrix} \chi_{j+1,k}^{1,n+1/2} \\ \chi_{j+1,k}^{2,n+1/2} \end{pmatrix} = \begin{pmatrix} \cos(\vartheta) & \sin(\vartheta) \\ -\sin(\vartheta) & \cos(\vartheta) \end{pmatrix} \begin{pmatrix} \hat{\chi}_{j+1,k}^{1,n+1/2} \\ \hat{\chi}_{j+1,k}^{2,n+1/2} \end{pmatrix},$$

*where the angle  $\vartheta$  is computed by*

$$\tan(\vartheta) = -\frac{\langle \hat{\chi}_{j,k}^{1,n+1/2}, \chi_{j,k}^{2,n+1/2} \rangle}{\langle \hat{\chi}_{j,k}^{2,n+1/2}, \chi_{j,k}^{2,n+1/2} \rangle}.$$

### 3.3 Discretization of the Schrödinger-Poisson system

---

The value of  $\vartheta$  follows from considering  $\langle \chi_{j+1,k}^{1,n+1/2}, \chi_{j,k}^{2,n+1/2} \rangle = 0$ , which is a natural condition for  $\chi_{j+1,k}^{1,n+1/2}, \chi_{j+1,k}^{2,n+1/2}$ , being close to  $\chi_{j,k}^{1,n+1/2}, \chi_{j,k}^{1,n+1/2}$ . For details and numerical tests we refer to [Po05].

Performing the transformation

$$\varphi_{j,m}^n = \sum_{k=1}^{K-1} \chi_{j,k}^{m,n+1/2} \psi_{j,k}^n, \quad m = 1, \dots, K-1, j = 0, \dots, J, n \in \mathbb{N}_0,$$

and accordingly

$$\psi_{j,k}^n = \sum_{m=1}^{K-1} \chi_{j,k}^{m,n+1/2} \varphi_{j,m}^n, \quad k = 1, \dots, K-1, j = 0, \dots, J, n \in \mathbb{N}_0 \quad (3.19)$$

yields by inserting (3.19) into (3.17) the coupled discrete 1D equations

$$\begin{aligned} \frac{i\hbar}{\Delta t} (\varphi_{j,m}^{n+1} - \varphi_{j,m}^n) &= -\frac{\hbar^2}{2m_* \Delta x^2} (\varphi_{j-1,m}^{n+1/2} - 2\varphi_{j,m}^{n+1/2} + \varphi_{j+1,m}^{n+1/2}) \\ &\quad + \epsilon_{j,m}^{n+1/2} \varphi_{j,m}^{n+1/2} - \frac{i\hbar}{2} \sum_{q=1}^{K-1} (c_{j,m,q}^{n+1} \varphi_{j,q}^{n+1} + c_{j,m,q}^n \varphi_{j,q}^n) \\ &\quad - \frac{\hbar^2}{4m_*} \sum_{q=1}^{K-1} (d_{j,m,q}^{n+1} \varphi_{j,q}^{n+1} + d_{j,m,q}^n \varphi_{j,q}^n) \\ &\quad - \frac{\hbar^2}{2m_*} \sum_{q=1}^{K-1} (e_{j,m,q}^{n+1} D_x^0 \varphi_{j,q}^{n+1} + e_{j,m,q}^n D_x^0 \varphi_{j,q}^n), \\ &\quad j = 1, \dots, J-1, m = 1, \dots, K-1, n \in \mathbb{N}_0, \end{aligned} \quad (3.20)$$

with the abbreviations

$$\begin{aligned} c_{j,m,q}^n &= \langle D_t^+ \chi_{j,k}^{m,n+1/2}, \chi_{j,k}^{q,n+1/2} \rangle, \\ d_{j,m,q}^n &= \langle D_x^2 \chi_{j,k}^{m,n+1/2}, \chi_{j,k}^{q,n+1/2} \rangle, \\ e_{j,m,q}^n &= \langle D_x^+ \chi_{j,k}^{m,n+1/2}, \chi_{j,k}^{q,n+1/2} \rangle, \end{aligned} \quad (3.21)$$

for the coupling terms and the difference operators

$$\begin{aligned} D_x^0 \varphi_{j,m}^n &= \frac{1}{2\Delta x} (\varphi_{j+1,m}^n - \varphi_{j-1,m}^n), \\ D_x^+ \varphi_{j,m}^n &= \frac{1}{\Delta x} (\varphi_{j+1,m}^n - \varphi_{j,m}^n), \\ D_x^2 \varphi_{j,m}^n &= \frac{1}{\Delta x^2} (\varphi_{j+1,m}^n - 2\varphi_{j,m}^n + \varphi_{j-1,m}^n), \\ D_t^+ \varphi_{j,m}^n &= \frac{1}{\Delta t} (\varphi_{j,m}^{n+1} - \varphi_{j,m}^n), \\ &\quad j = 1, \dots, J-1, m = 1, \dots, K-1, n \in \mathbb{N}_0. \end{aligned} \quad (3.22)$$

### 3 Transient quantum simulations for the double gate MOSFET

---

In each time step we solve  $M < K$  coupled 1D equations according to (3.20) by truncating the coupling sums at  $q = M$ . We set  $c_{j,m,q}^n = d_{j,m,q}^n = e_{j,m,q}^n = 0$  for all  $q = M + 1, \dots, K - 1$  and solve additionally the  $K - M - 1$  uncoupled 1D equations

$$\frac{i\hbar}{\Delta t} (\varphi_{j,m}^{n+1} - \varphi_{j,m}^n) = -\frac{\hbar^2}{2m_*\Delta x^2} (\varphi_{j-1,m}^{n+1/2} - 2\varphi_{j,m}^{n+1/2} + \varphi_{j+1,m}^{n+1/2}) + \epsilon_{j,m}\varphi_{j,m}^{n+1/2} \quad (3.23)$$

for  $m = M + 1, \dots, K$ ,  $j = 1, \dots, J - 1$ ,  $n \in \mathbb{N}_0$ .

Since the eigenfunctions  $\chi_{j,k}^{m,n+1/2}$  are constant in  $x_j$ -direction and time independent for  $j \leq 0$  and  $j \geq J$ , we obtain  $c_{j,m,q}^n = d_{j,m,q}^n = e_{j,m,q}^n = 0$  for all  $j = 1, J$ ,  $m, q = 1, \dots, K - 1$ ,  $n \geq 0$  and the energy  $\epsilon_{j,m}^{n+1/2}$  is constant for all  $n \geq 0$ . Hence, equation (3.20) reduces in transport direction at the boundaries to (3.23) for  $j = 0, J$ ,  $m = 1, \dots, K - 1$ ,  $n \in \mathbb{N}_0$ , which coincides with (1.4) by replacing the potential with  $\epsilon_{j,m}$ . Hence we can use the DTBCs obtained in §1 for this model.

#### 3.3.2 Discretizing the Poisson equation

In the outer domains  $x \leq 0$  and  $x \geq X$  we assume given external potentials  $V_0(y)$  and  $V_X(y)$ , which give rise to the constant-in-time self-consistent potentials  $V_{0,s}(y)$  and  $V_{X,s}(y)$ . For the left outer domain we compute  $V_{0,s}(y)$  numerically by solving the discretized Poisson equation (3.10) with the electron density (3.13) and  $\mu$  obtained from (3.14). For the discretization of the Laplacian we use the standard second order difference operator.

In each time step we solve (3.18), therefore we need the self-consistent potential in the interior domain at each time step. This is obtained by solving the Poisson equation (3.15) again with the standard five-point discretization of the Laplacian. In [Pi02] the author updates the potential by extrapolation:

$$V_s^{n+3/2} = 2V_*^{n+1} - V_s^{n+1/2}, \quad n \geq 0 \quad (3.24)$$

where  $V_*^{n+1}$  is the solution to the Poisson equation (3.15) at time  $t_{n+1}$ .  $V_s^{n+1/2}$  denotes the self-consistent part of the potential in the time step  $n$  and the total potential arises from the sum of the external and the self-consistent potential.

#### 3.3.3 Implementation of the model

Finally we summarize the algorithm for the implementation of the model. The following steps (1)-(7) have to be calculated only once before starting to solve the time stepping algorithm for the Schrödinger-Poisson system:

### 3.3 Discretization of the Schrödinger-Poisson system

---

- (1) We choose a given external potential  $V_e(x, y, t)$  (cf. (3.4)) and an initial potential  $V(x, y, 0)$ .
- (2) Next, we choose a given energy  $E_{x,y}$  of the incoming wave. For a the given energy  $E_{x,y}$  the wavenumber  $k_x$  of the injected plane wave

$$\varphi_{j,m}^n = e^{ik_x j \Delta x} e^{-iE_{x,y} n \Delta t / \hbar}, \quad j \leq 0, m = 1, \dots, K-1, n \in \mathbb{N}_0$$

has to be calculated by inverting the discrete dispersion relation

$$E_{x,y} = \frac{\hbar^2}{m_*} \left( \frac{1 - \cos(\Delta x k_x)}{\Delta x^2} \right) + \frac{\hbar^2}{m_*} \left( \frac{1 - \cos\left(\frac{\pi \Delta y}{Y}\right)}{\Delta y^2} \right).$$

We consider the discrete incoming function  $(\varphi^{inc})_{0,m}^n = e^{-iE_{x,y} n \Delta t / \hbar}$  at  $j = 0$ . For different transversal modes  $\varphi_m$  one may take also different wavenumbers  $k_x$  and therefore different energies  $E_{x,y}$ .

- (3) The discrete initial function has to be chosen. The initial function is a plane wave  $\varphi_{j,m}^0 = e^{ik_x j \Delta x}$ ,  $j = 0, \dots, J$ ,  $m = 1, \dots, K-1$ , which fits to the injected wave  $(\varphi^{inc})_{0,m}^n$ .
- (4) In the r.h.s. of the 2D Poisson equation (3.15) appears the discretized 2D electron density  $(n_{2D})_{j,k}^n$  (cf. (3.16)) with  $k_x \in [-c, c]$ ,  $c \in \mathbb{R}^+$ . For the scaled values  $\hbar = m_* = k_B = T = 1$  one computes  $e^{-\hbar^2 k_x^2 / 2m_*} \leq 10^{-10}$  for  $k_x \geq 7$ . The choice of  $c$  depends on the absolute value of the injected wave,  $e^{-\hbar^2 c^2 / 2m_*} |\psi_{\lambda_{x,y}}^{inc}(x, y, t)|^2$  should be “small enough”. For a finite number of wavenumbers  $k_x^{(\ell)} \in [-c, c]$ ,  $\ell = -L, 1-L, \dots, L$  we choose the initial functions  $(\varphi_{j,m}^0)^{(\ell)} = e^{ik_x^{(\ell)} j \Delta x}$ ,  $j = 0, \dots, J$ ,  $\ell = -L, 1-L, \dots, L$ ,  $m = 1, \dots, K-1$  of the coupled 1D Schrödinger equations (3.20). The solutions  $(\varphi_{j,m}^n)^{(\ell)}$ ,  $\ell = -L, \dots, L$  to (3.20) with this initial data will be used after the transformation (3.19) in each time step for the r.h.s. for the 2D Poisson equation (3.15) for all  $k_x^{(\ell)}$ ,  $\ell = -L, 1-L, \dots, L$ .
- (5) The chemical potential  $\mu$  is computed according to (3.14).
- (6) The convolution coefficients for the DTBCs can either be calculated exactly (cf. Theorem 1.1, §1) or approximately (cf. Remark 1.3, §1). They are not time-dependent and they do not depend on the wavenumbers.

### 3 Transient quantum simulations for the double gate MOSFET

---

- (7) For the determination of the self-consistent potential outside the computational domain we solve the 1D Poisson equation (3.10) with the standard second order finite difference discretization for both  $y$ -dependent external potentials on the leads  $j \leq 0$ ,  $j \geq J$ . At  $y = 0$  and  $y = Y$  zero Neumann boundary conditions are assumed. The obtained solutions are vectors denoted by  $V_{0,k}$ ,  $V_{J,k}$ ,  $k = 1, \dots, K - 1$  of length  $K - 1$  for each outer domain. They will be needed as boundary conditions of the 2D Poisson equation inside the computational domain.

At the time step  $t_n$  we have given  $\varphi_{j,m}^n$ ,  $\chi_{j,k}^{m,n+1/2}$ ,  $V_{j,k}^{n+1/2}$ ,  $c_{j,m,q}^n$ ,  $d_{j,m,q}^n$ ,  $e_{j,m,q}^n$ ,  $(n_{2D})_{j,k}^n$  and the convolution sum  $\sum_{\nu=1}^n s_{j,m}^{(n+1-\nu)} \varphi_{j,m}^\nu$  for the DTBCs. For the time stepping algorithm the following items are calculated iteratively as an update from time step  $t_n$  to  $t_{n+1}$ :

- (8) We calculate the 2D electron density (3.16) appearing in the r.h.s. of the 2D Poisson equation (3.15) at time step  $t_{n+1}$ . Therefore we solve for the finite number of wavenumbers  $k_x^{(\ell)} \in [-c, c]$ ,  $\ell = -L, \dots, L$  the time-dependent Schrödinger equation (3.20) with inhomogeneous DTBCs at  $x = 0$  and DTBCs  $x = X$ .
- (9) With  $n_{2D}$  computed in step (8) we solve the 2D Poisson equation. At  $y = 0$  and  $y = Y$  we use homogeneous Neumann boundary conditions and we use the Dirichlet boundary conditions  $V_{0,k}$ ,  $V_{J,k}$ ,  $k = 1, \dots, K - 1$  obtained from step (7). This yields  $V_*^{n+1}$ .
- (10) The self-consistent part of the potential is computed by  $V_s^{n+3/2} = 2V_*^{n+1} - V_s^{n+1/2}$  (cf. (3.24)).
- (11) We calculate the eigenfunctions  $\chi_{j,k}^{m,n+3/2}$  and the energies  $\epsilon_j^{m,n+3/2}$  for  $j = 0, \dots, J$  by solving the eigenvalue problems (3.18). It is necessary to take care of the orientation  $\chi_{j,k}^{m,n+3/2}$  w.r.t. the orientation of  $\chi_{j,k}^{m,n+1/2}$  and of  $\chi_{j+1,k}^{m,n+3/2}$  w.r.t.  $\chi_{j,k}^{m,n+3/2}$ . We observe also the orthogonality of  $\chi_{j,k}^{1,n+3/2}$ ,  $\chi_{j,k}^{2,n+3/2}$  (cf. Remark 3.5). With the eigenfunctions we can compute the coupling coefficients  $c_{j,m,q}^{n+1}$ ,  $d_{j,m,q}^{n+1}$ ,  $e_{j,m,q}^{n+1}$  with (3.21), (3.22).

- (12) At the boundaries  $x = 0$  and  $x = X$  the wave function  $\psi_{\lambda_{x,y}}$  is transformed according to (3.5).
- (13) The coupled 1D equations (3.20) with the DTBCs from Theorem 1.1 (§1) are solved via a direct method or iteratively. We cut the sums  $\sum_{q=1}^{K-1}$  to  $\sum_{q=1}^M$ .
- (14) Additionally we solve  $K - M - 1$  uncoupled 1D Schrödinger equations (3.23).
- (15) At the boundaries  $x = 0$  and  $x = X$  the wave function  $\psi_{\lambda_{x,y}}$  has to be transformed back according to the inverse transformation of (3.5).
- (16) We store the boundary data  $\varphi_{j,m}^{n+1}$ ,  $j = 0, J$  for all modes  $m = 1, \dots, K - 1$  for the computation of the convolution sum for the DTBCs.
- (17) The wave function  $\psi$  which is the solution to the 2D Schrödinger equation is obtained by the transformation (3.19).

## 3.4 Numerical results

In this section we will present numerical examples concerning the 2D time-dependent Schrödinger-Poisson system including open boundary conditions in transport direction. In a first example we will stress the advantages due to the  $y$ -dependence of the external potential in the leads of the waveguide. Therefore we drop the self-consistent potential in this example and solve only the Schrödinger equation on a rectangular domain. In a second example we will present a solution to the coupled Schrödinger-Poisson system.

### 3.4.1 Example 1: $y$ -dependent potentials in the outer domains

Consider a rectangular computational domain  $\Omega = (0, 1)^2$ . We compute the solution  $\psi$  to the scaled 2D Schrödinger equation

$$i \frac{\partial}{\partial t} \psi(x, y, t) = -\frac{1}{2} \Delta \psi(x, y, t) + V(x, y, t) \psi(x, y, t), \quad (x, y) \in \Omega, t > 0 \quad (3.25)$$

by solving the coupled 1D equations (3.9) with the initial data

$$\varphi_m^I(x) = e^{ik_x x}, \quad x \in [0, 1/2], m = 1 \quad (3.26)$$

### 3 Transient quantum simulations for the double gate MOSFET

---

which is smoothly damped down to zero for  $x > 1/2$ . The given wavenumber  $k_x$  corresponds to an energy  $E_{x,y} = 200$ . We inject only on the first mode  $m = 1$  and the incoming function  $\varphi_1^{inc}(x, t) = e^{ik_x x} e^{-iE_{x,y} t}$  has the same energy as the initial function. At  $x = 1$  we implement homogeneous DTBCs, inhomogeneous DTBCs are considered at  $x = 0$ . The potential is chosen rather arbitrarily as

$$V(x, y, t) = \begin{cases} \tilde{V}(x, y) & : y \in (0, 1), x \leq x_1, t > 0 \\ \tilde{V}(x, y) + V^2(x, t) & : y \in (0, 1), x \geq x_1, t > 0, \end{cases} \quad (3.27)$$

with  $\tilde{V}(x, y) = 100 - 300y(1-y) + 150e^{-\alpha[(x-3/4)^2 + (y-1/2)^2]}$ ,  $\alpha = 80$ , and some fixed value  $0 < x_1 < 1$ .  $V^2(x, t)$  is a piecewise constant function in time, continuous in  $x$  and bounded. Hence,  $V(x, y, t)$  is increasing for  $y \rightarrow 0$  and  $y \rightarrow 1$ . We use Dirichlet boundary conditions  $\psi(x, 0, t) = \psi(x, 1, t) = 0$  at the channel walls  $y = 0$  and  $y = 1$ . These conditions are somehow “natural” since the potential acts like a barrier at the walls. We use the discretization parameters  $J = K = 60$ ,  $\Delta t = 0.001$  and choose  $M = 10$  for the number of coupled modes. In Figure 3.5 we present the piecewise constant-in-time potential  $V$  for times  $t > 0$ . Figure 3.6 shows some temporal snapshots of  $|\psi|^2$  (cf. (3.19)), where  $\psi$  is the solution to the scaled 2D Schrödinger equation (3.25) with the initial function (3.26) for the corresponding coupled 1D system and the potential (3.27). The wave function leaves the computational domain without being reflected back at the artificial boundaries. The occupation density  $|\varphi_m(x, t)|^2 / \sum_{m=1}^M |\varphi_m(x, t)|^2$  of the different subbands is shown in Figure 3.7. At the initial time only the first band  $m = 1$  is occupied. After several time steps there are also higher modes get occupied. Since

$$\int_0^Y \chi_m(x, y, t) dy = 0$$

holds for this choice of  $V(x, y, t)$  for even modes  $m$ , only the odd modes  $\varphi_m(x, t)$ ,  $m = 1, 3, 5, \dots$  are occupied. With the choice  $M = 10$  the subband decomposition algorithm is about 80% faster than the usual algorithm for the 2D Schrödinger equation proposed in §1.

#### 3.4.2 Example 2: A solution to the Schrödinger-Poisson system

We compute the solution  $\psi(x, y, t) = \sum_{m=1}^{K-1} \varphi_m(x, t) \chi_m(x, y, t)$  to the scaled coupled Schrödinger-Poisson system (we let all physical constants  $\hbar$ ,  $m_*$ ,  $k_B$ ,  $T$  equal 1) on the computational domain  $\Omega = (0, 1)^2$  with the subband decomposition algorithm. The given doping profile is chosen constant as  $n_D = 100$  and we assume

### 3.4 Numerical results

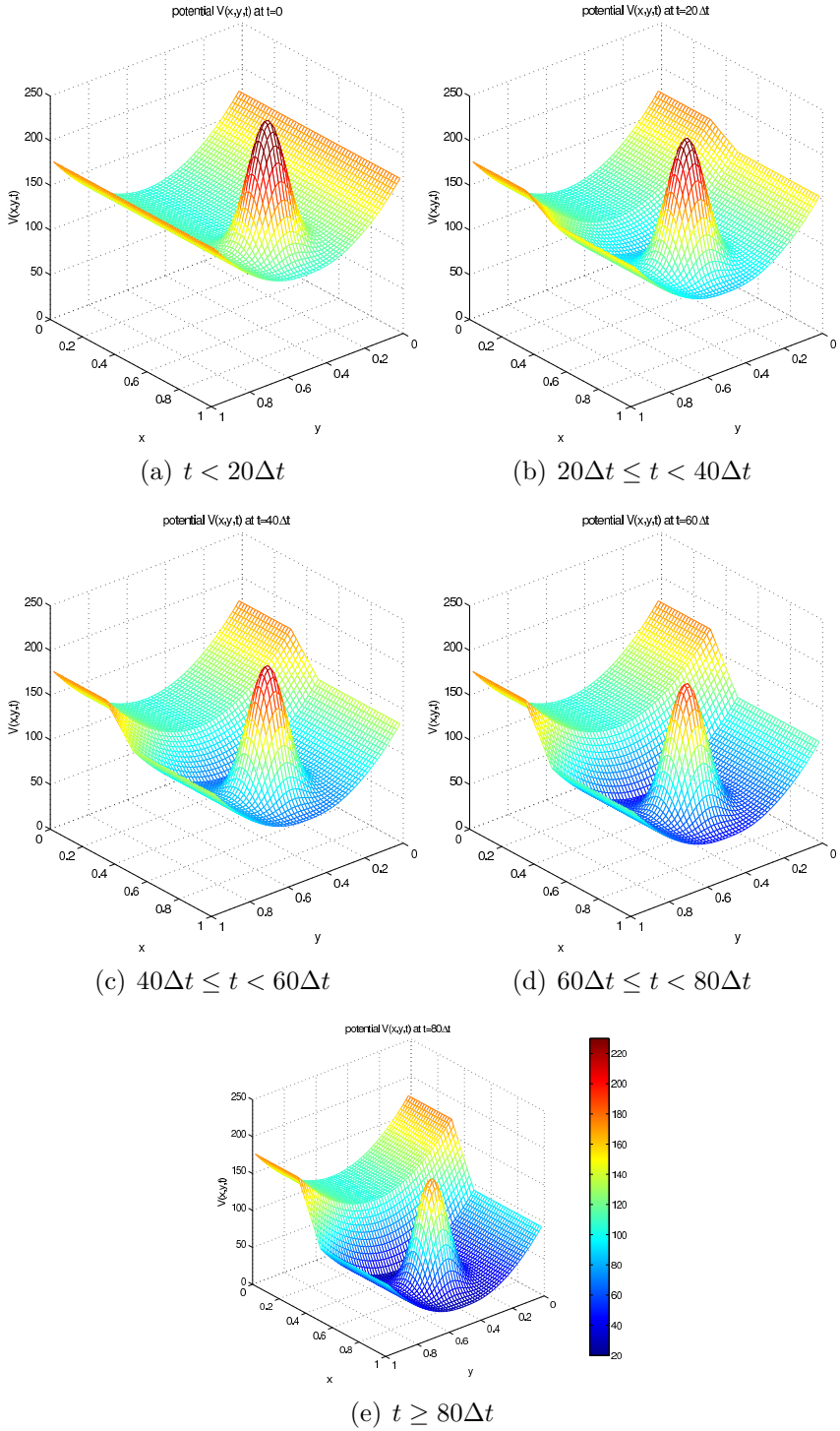


Figure 3.5: Example 1. Potential  $V(x, y, t)$  (cf. (3.27)), which is a piecewise constant function in time.

### 3 Transient quantum simulations for the double gate MOSFET

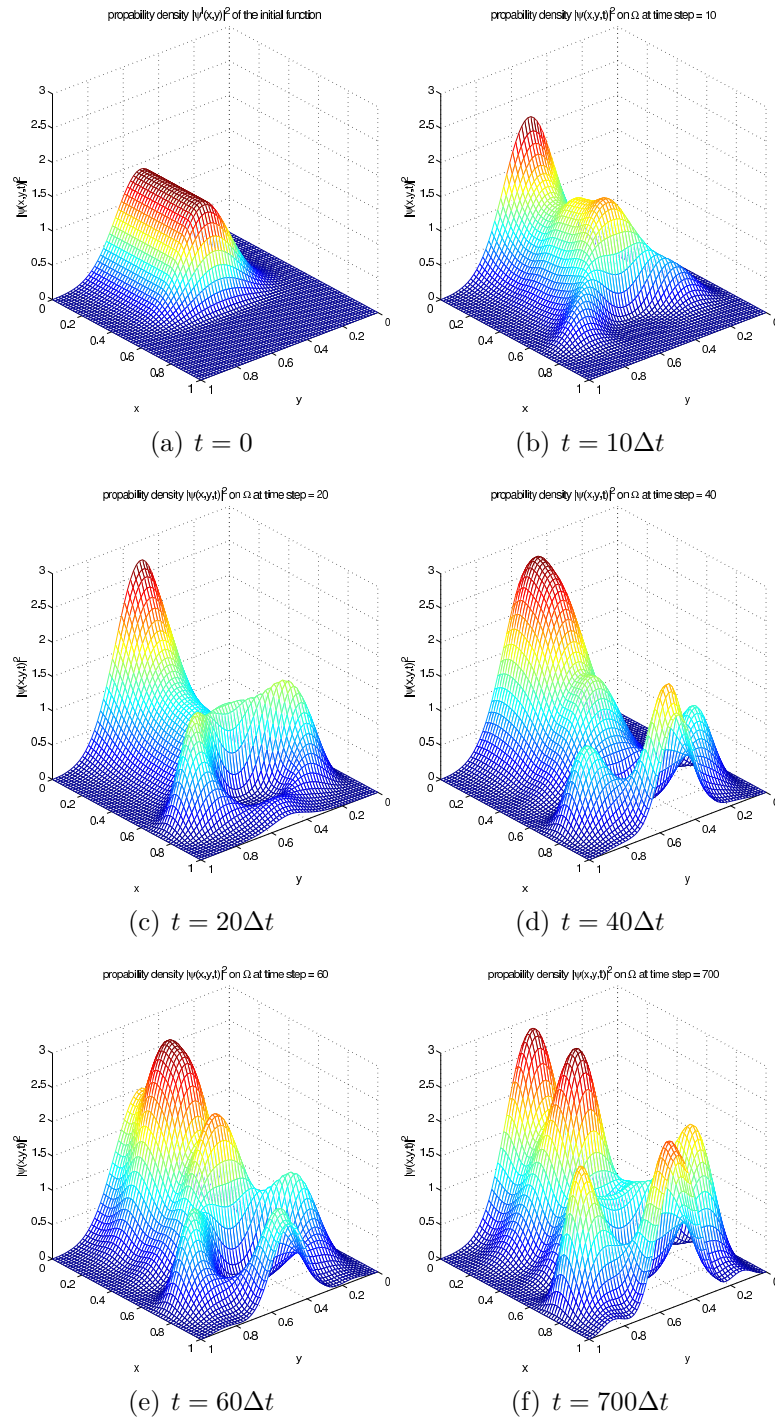


Figure 3.6: Example 1. Squared absolute value of the solution  $\psi$  to the Schrödinger equation (3.25) with the initial function (3.26) and the potential (3.27). The discretization parameters are  $\Delta x = \Delta y = 1/60$ ,  $\Delta t = 0.001$ ,  $M = 10$ .

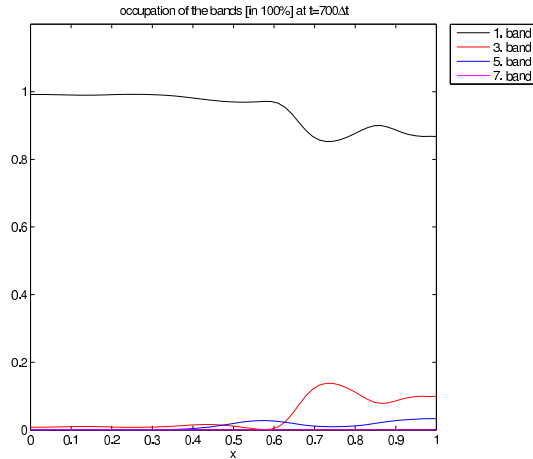


Figure 3.7: Example 1. Occupation density  $|\varphi_m(x, t)|^2 / \sum_{m=1}^M |\varphi_m(x, t)|^2$  of the different bands at  $t = 700\Delta t$ .

an external potential

$$V_e(x, y, t) = \begin{cases} 0 & : (x, y) \in \Omega, t \leq t_1 \\ \tilde{V}(x, y) \cdot \sin\left(\frac{\pi(t-t_1)}{2(t_2-t_1)}\right) & : (x, y) \in \Omega, t_1 \leq t < t_2 \\ \tilde{V}(x, y) & : (x, y) \in \Omega, t \geq t_2 \end{cases} \quad (3.28)$$

with  $\tilde{V}(x, y) = 100y(1-y)e^{-\alpha[(x-1/2)^2+(y-1/2)^2]}$ ,  $\alpha = 30$ ,  $t_1 = 30\Delta t$ ,  $t_2 = 100\Delta t$ . Some temporal snapshots of the external potential  $V_e(x, y, t)$  are shown in Figure 3.8. At  $t = 0$  the external potential equals zero. For  $t \geq 30\Delta t$  it is built by a Gaussian beam which is increasing in time up to  $t = 100\Delta t$ . For  $t \geq 100\Delta t$  it stays constant in time. The maximum peak of the potential is 25. Again we consider the initial function

$$\varphi_m^I(x) = e^{ik_x x}, \quad x \in [0, 0.8], m = 1$$

which is smoothly damped down to zero for  $x$  tending to 1 for the system (3.9) of coupled 1D equations. In this example we calculate solutions  $\psi$  for different choices of wavenumbers  $k_x$ . The absolute value of an example for such an initial function is plotted in Figure 3.9.

For the discretization parameters  $M = 10$ ,  $\Delta x = \Delta y = 1/50$ ,  $\Delta t = 0.001$  we compute on the one hand the solution to the 2D time-dependent Schrödinger equation (3.25) *without* the self-consistent Poisson coupling and, on the other hand, the solution to the coupled Schrödinger-Poisson system (cf. (3.25), (3.15)) for 500 time steps. An incoming function  $\varphi_m^{inc}(x, t) = e^{ik_x x} e^{-iE_{x,y} t}$ ,  $m = 1$  is injected at

### 3 Transient quantum simulations for the double gate MOSFET

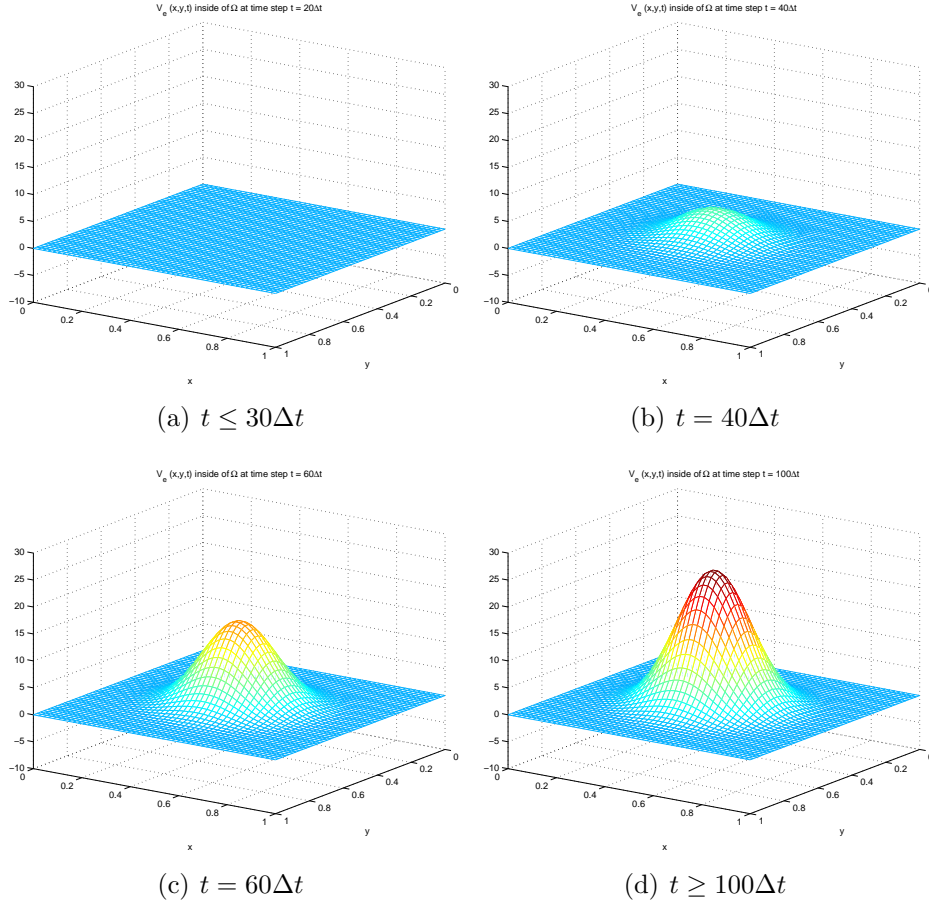


Figure 3.8: Example 2. External potential  $V_e(x, y, t)$  (cf. (3.28)).

$x = 0$ . Therefore, inhomogeneous DTBCs are implemented at  $x = 0$ . Homogeneous DTBCs are given at  $x = 1$ . At  $y = 0, y = 1$  we assume homogeneous Dirichlet boundary conditions.

For the Schrödinger-Poisson case, the evolution of the total potential (including the self-consistent part),  $V(x, y, t) = V_s(x, y, t) + V_e(x, y, t)$ , is presented in Figure 3.10. Up to some time the self-consistent part is partially increasing, afterwards it is decreasing. The maximum peak of  $V(x, y, t)$  at  $t = 500\Delta t$  is about  $\sim 20$ .

In Figure 3.11 we present results for the wavenumber  $k_x = 0$ , which corresponds to an energy  $E_{x,y} \sim 5$ . We plot the absolute value of the solution to the Schrödinger equation *without* the self-consistent coupling to the Poisson equation on the left side in Figures 3.11(a), 3.11(c) and 3.11(e). On the right side we

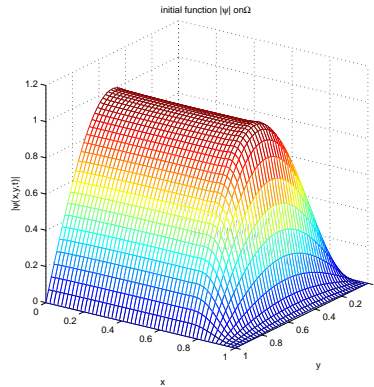


Figure 3.9: Example 2. Absolute value of the initial function  $\varphi_1^I(x)$  for the coupled Schrödinger-Poisson system.

show the results obtained with the Schrödinger-Poisson system in Figures 3.11(b), 3.11(d) and 3.11(f).

For the wavenumber  $k_x = 8$ , which corresponds to an energy  $E_{x,y} \sim 37$ , we present the solutions of the same calculations in Figure 3.12.

In all examples the wave functions travel through the channel without any unphysical reflections at the artificial boundaries  $x = 0$  and  $x = 1$ . For  $k_x = 0$  the potential  $V(x, y, t)$  is acting like a barrier in the case of solving the Schrödinger equation and also in the case of solving the Schrödinger-Poisson system. For  $k_x = 8$  the energy of the travelling wave is higher and hence more electrons can travel through the channel without being reflected back at the potential. One can clearly obtain in the calculations for  $k_x = 0$  and  $k_x = 8$  that the particle density in the region  $(0, 0.5) \times (0, 1)$  is much bigger in the case of the solution to the Schrödinger equation without coupling than in the case of the solution to the coupled system. This results from the fact, that the potential  $V(x, y, t) = V_e(x, y, t) + V_s(x, y, t)$  is smaller than the external part  $V_e(x, y, t)$ .

## 3.5 Conclusion

We have combined DTBCs for the 2D time-dependent Schrödinger equation with the physical model of the coupled Schrödinger-Poisson system. This is a highly relevant model for simulations of semiconductor devices like the DGMOS. Furthermore we have extended the DTBCs to  $y$ -dependent potentials in the outer domains and introduced the efficient subband decomposition algorithm for the solution of the coupled system.

### 3 Transient quantum simulations for the double gate MOSFET

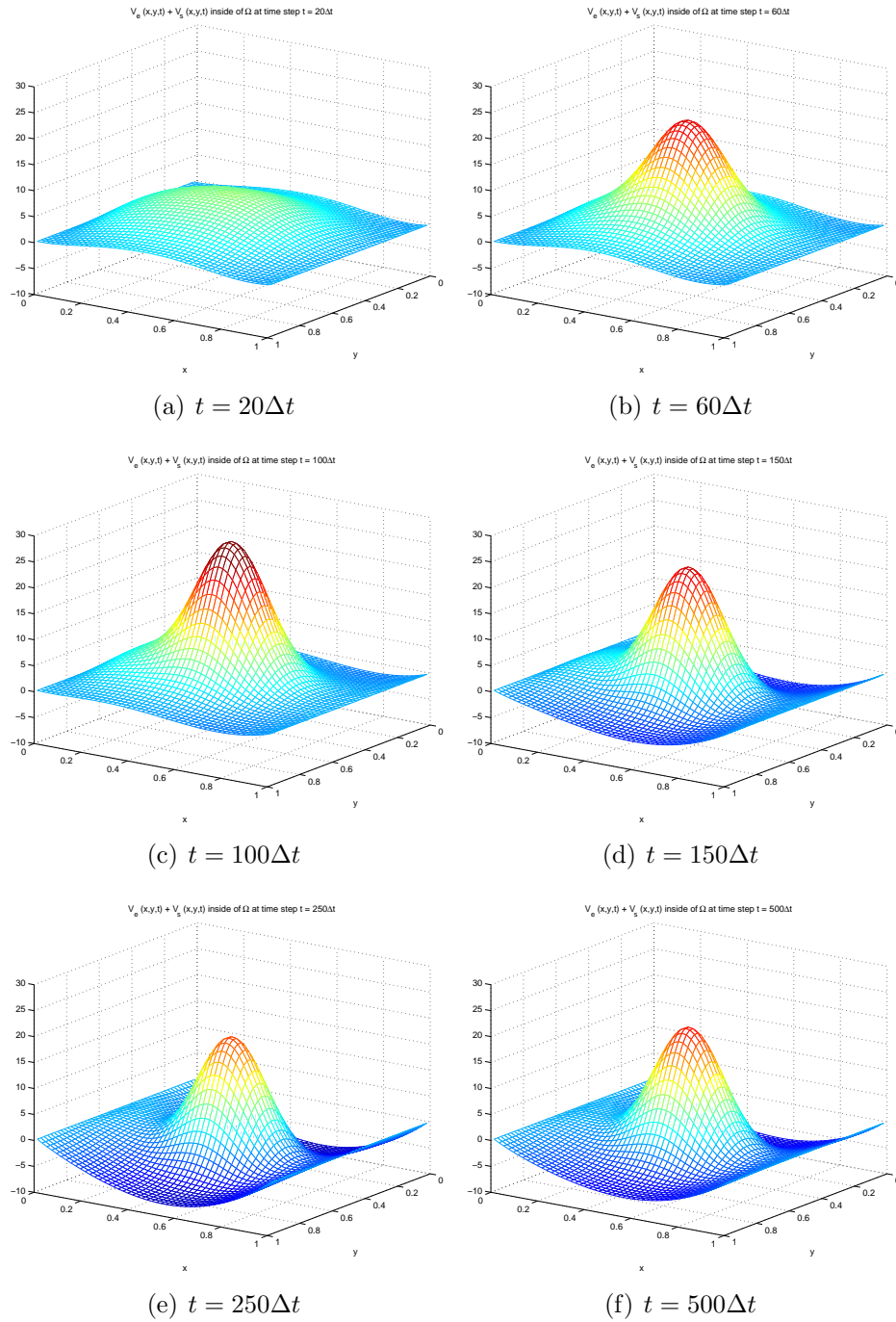


Figure 3.10: Example 2. Potential  $V(x, y, t) = V_e(x, y, t) + V_s(x, y, t)$  with  $V_e$  given in (3.28) and the self-consistent potential  $V_s$  which is a solution to the Poisson equation (3.15).

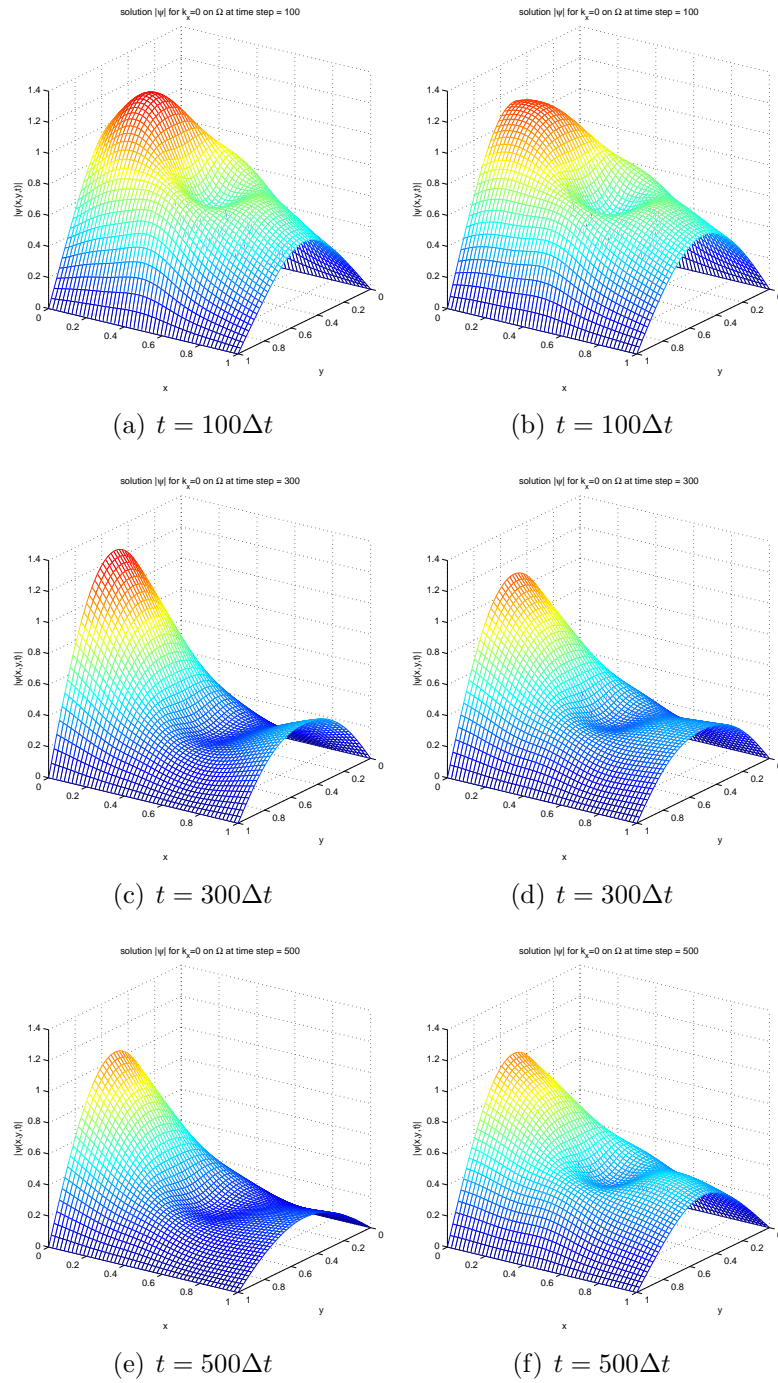


Figure 3.11: Example 2. Absolute value of the solution to the scaled Schrödinger equation without Poisson coupling ((a), (c), (e)) and of the solution to the scaled Schrödinger-Poisson system ((b), (d), (f)) for the wavenumber  $k_x = 0$ . We choose the discretization parameters  $M = 10$ ,  $\Delta x = \Delta y = 1/50$ ,  $\Delta t = 0.001$ .

### 3 Transient quantum simulations for the double gate MOSFET

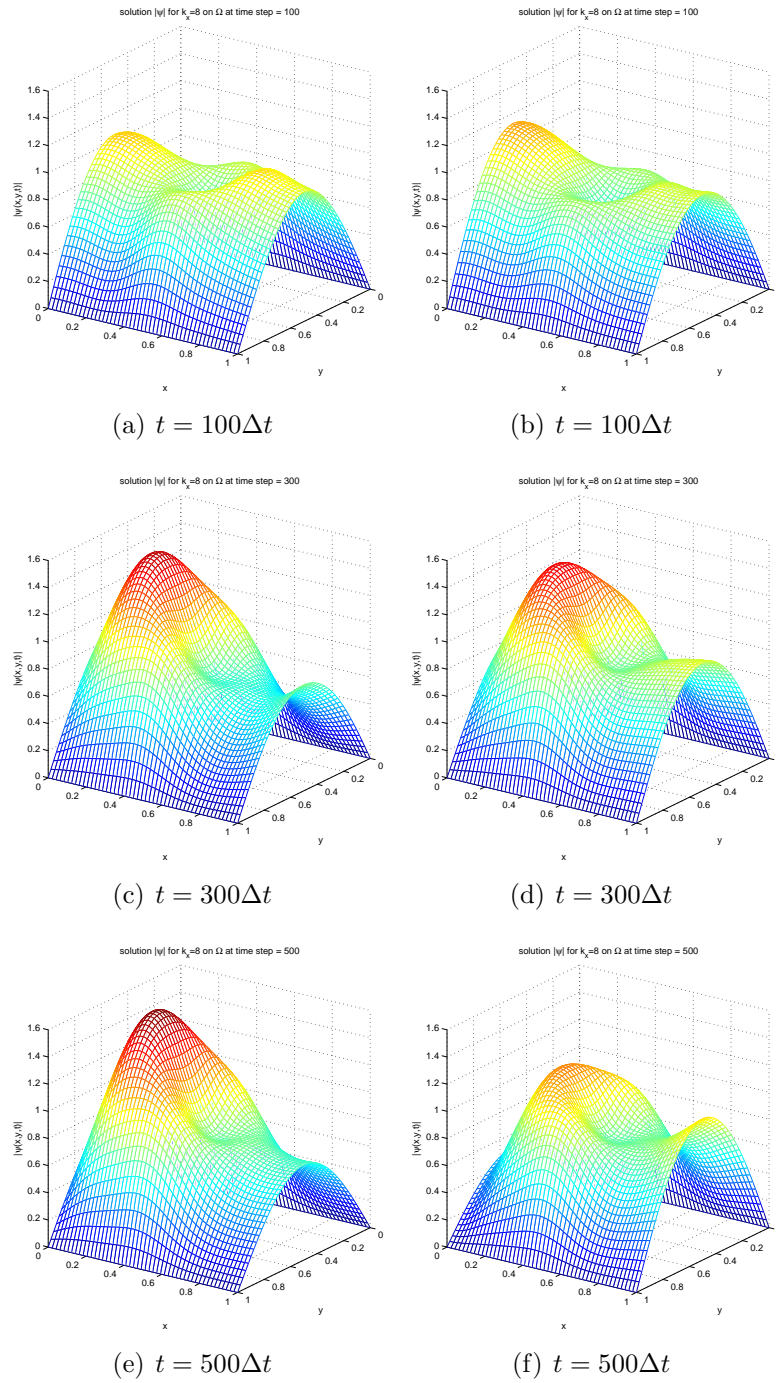


Figure 3.12: Example 2. Absolute value of the solution to the scaled Schrödinger equation without Poisson coupling ((a), (c), (e)) and of the solution to the scaled Schrödinger-Poisson system ((b), (d), (f)) for the wavenumber  $k_x = 8$ . We choose the discretization parameters  $M = 10$ ,  $\Delta x = \Delta y = 1/50$ ,  $\Delta t = 0.001$ .

# Bibliography

- [BeMePi05] N. Ben Abdallah, F. Méhats and O. Pinaud: *On an open transient Schrödinger-Poisson system*, Math. Mod. Meth. Appl. Sci. **15** (2005) 667–688
- [BePi02] N. Ben Abdallah and O. Pinaud: *A mathematical model for the transient evolution of a resonant tunneling diode*, C. R. Math. Acad. Sci. Paris **334** (2002) 283–288
- [Ca97] F. Castella:  *$L^2$  solutions to the Schrödinger-Poisson system: existence, uniqueness, time-behavior, and smoothing effects*, Math. Mod. Meth. Appl. Sci. **7** (1997) 1051–1083
- [Ca89] T. Cazenave: *An introduction to nonlinear Schrödinger equations*, Textos de Métodos Matemáticos **22** I.M.U.F.R.J., Rio de Janeiro (1989)
- [FeGo97] D.K. Ferry and S.M. Goodnick: *Transport in Nanostructures*, Cambridge University Press, Cambridge (1997)
- [IlZwLa94] R. Illner, P.F. Zweifel and H. Lange: *Global existence, uniqueness and asymptotic behavior of the Wigner-Poisson and Schrödinger-Poisson systems*, Math. Meth. Appl. Sci. **17** (1994) 349–376
- [Pi02] O. Pinaud: *Transient simulations of a resonant tunneling diode*, J. Appl. Phys. **92** (2002) 1978–1994
- [Po02] E. Polizzi and N. Ben Abdallah: *Self-consistent three dimensional model for quantum ballistic transport in open systems*, Phys. Rev B. **66** 245301–245309 (2002)
- [Po05] E. Polizzi and N. Ben Abdallah: *Subband decomposition approach for the simulation of quantum electron transport in nanostructures*, J. Comp. Phys. **202** (2005) 150–180

# 4 Discrete transparent boundary conditions for the two dimensional Schrödinger equation on circular domains

In this chapter we propose transparent boundary conditions for the time-dependent Schrödinger equation on a circular computational domain. First we derive the two dimensional discrete TBCs in conjunction with a conservative Crank-Nicolson-type finite difference scheme. The presented discrete boundary-valued problem is unconditionally stable and completely reflection-free at the boundary. Then, since the discrete TBCs for the Schrödinger equation with a spatially dependent potential include a convolution w.r.t. time with a weakly decaying kernel, we construct *approximate* discrete TBCs with a kernel having the form of a finite sum of exponentials, which can be efficiently evaluated by recursion. Finally, we describe several numerical examples illustrating the accuracy, stability and efficiency of the proposed method.

## 4.1 Introduction

Consider in the circular geometry with polar coordinates  $(r, \theta)$  the following Cauchy problem for the scaled transient Schrödinger equation

$$\begin{aligned} i\psi_t &= -\frac{1}{2} \left[ \frac{1}{r} (r\psi_r)_r + \frac{1}{r^2} \psi_{\theta\theta} \right] + V(r, \theta, t)\psi, \quad r \geq 0, 0 < \theta \leq 2\pi, t > 0, \\ \psi(r, \theta, 0) &= \psi^I(r, \theta), \quad r \geq 0, 0 < \theta \leq 2\pi. \end{aligned} \quad (4.1)$$

We assume that the given periodical potential  $V$  is constant outside of the computational domain  $[0, R] \times [0, 2\pi]$ :

$$V(r, \theta, t) = V_R \equiv \text{const} \quad \text{for } r \geq R,$$

and that the sufficiently smooth periodical initial data has a compact support:

$$\text{supp } \psi^I \subset [0, R] \times [0, 2\pi].$$

Equation (4.1) has different important applications including electromagnetic wave propagation [Lev00], modeling of quantum devices [Ar95], integrated optics (Fresnel equation) [ScDe95], plasma physics and (underwater) acoustics due to the *paraxial approximation* to the wave equation in the frequency domain [ArEh98], [Ta77], etc.

One quite important application of the Schrödinger equation especially in a circular geometry arises in the context of optical fibers [Ke83], [Za01].

### 4.1.1 Analytic transparent boundary conditions for the 2D Schrödinger equation on circular domains

Let us exemplify first *analytic* TBCs that can be derived for the Schrödinger equation on a circular domain. In the following we briefly review the construction of the analytic TBCs from [AnBeMo04] and extend them to the case of a nonzero potential at infinity. We remark that a more concise derivation can be found in [HaHu04], [JiGr06]. We consider sufficiently smooth bounded periodical solutions to (4.1) on the exterior domain  $r > R$  and denote by  $\Phi = \Phi(r, \theta, s)$  the Laplace transform of  $\psi$  w.r.t. time. The transformation of (4.1) reads

$$\frac{1}{r}(r\Phi_r)_r + \frac{1}{r^2}\Phi_{\theta\theta} + 2i(s + iV_R)\Phi = 0, \quad r \geq R, \quad 0 < \theta \leq 2\pi.$$

Using a Fourier series w.r.t. the angle  $\theta$ :

$$\Phi(r, \theta, s) = \sum_{m \in \mathbb{Z}} \Phi^{(m)}(r, s) e^{im\theta}, \quad r \geq R, \quad (4.2)$$

we obtain that the *Fourier coefficient*  $\Phi^{(m)}(r, s)$  for each mode  $m \in \mathbb{Z}$  satisfies the ordinary differential equation

$$\frac{1}{r}(r\Phi_r^{(m)})_r + \left(2is - 2V_R - \frac{m^2}{r^2}\right)\Phi^{(m)} = 0, \quad r \geq R. \quad (4.3)$$

This is the Bessel equation for functions of order  $m$ . Hence the solution to (4.3) vanishing as  $r \rightarrow \infty$  is given in terms of the *m-th order Hankel function of the first kind*  $H_m^{(1)}$ :

$$\Phi^{(m)}(r, s) = \alpha_m(s) H_m^{(1)}(\sqrt{2is - 2V_R} r), \quad r \geq R, \quad (4.4)$$

where  $\alpha_m(s)$  is an arbitrary multiplier. The radial derivative of  $\Phi^{(m)}$  is computed as

$$\begin{aligned} \frac{\partial}{\partial r} \Phi^{(m)}(r, s) &= \alpha_m(s) \sqrt{2is - 2V_R} H_m^{(1)'}(\sqrt{2is - 2V_R} r) \\ &= \sqrt{2is - 2V_R} \frac{H_m^{(1)'}(\sqrt{2is - 2V_R} R)}{H_m^{(1)}(\sqrt{2is - 2V_R} R)} \Phi^{(m)}(R, s), \end{aligned}$$

## 4 DTBCs for the two dimensional Schrödinger equation on circular domains

where we have determined the value of the coefficient  $\alpha_m(s)$  from (4.4) by setting  $r = R$ . Finally, the TBCs are obtained by computing the series (4.2), using the inverse Laplace transform and setting  $r = R$ . We achieve

$$\begin{aligned} \frac{\partial \psi}{\partial r}(R, \theta, t) = & \\ & \frac{1}{2\pi i} \sum_{m \in \mathbb{Z}} \int_{\gamma - i\infty}^{\gamma + i\infty} \sqrt{2is - 2V_R} \frac{H_m^{(1)'}(\sqrt{2is - 2V_R} R)}{H_m^{(1)}(\sqrt{2is - 2V_R} R)} \Phi^{(m)}(R, s) e^{st} ds e^{im\theta}, \end{aligned} \quad (4.5)$$

where  $\gamma$  is a vertical contour in the complex plane chosen such that all singularities of the integrand are to the left of it.

The TBCs (4.5) are non-local both in time and in space. A strategy to derive a spatially localized version of (4.5) by an asymptotic expansion of the Hankel functions and their derivatives according to  $s$  can be found in [AnBeMo04].

Because of the nonlocality of the TBCs (4.5), their immediate numerical implementation requires to store the boundary data  $\Phi^{(m)}(R, \cdot)$  of all the past history and for all modes  $m \in \mathbb{Z}$ . Moreover, the discretization of the TBCs (4.5), even in one space dimension, is not trivial at all and has attracted lots of attention. For the many proposed strategies of discretizations of the TBCs (4.5) in 1D (as well as semi-discrete approaches), we refer the reader to [AlRe02], [AnBe03], [BaPo91], [BrDi95], [Ma89], [Sc99], [ScDe95] and references therein. A numerically efficient treatment of 2D TBCs (4.5) is recently proposed in [JiGr06].

We remark also that inadequate discretizations may introduce strong numerical reflections at the boundary or render the discrete initial boundary value problem only conditionally stable, see [EhAr01] for a detailed discussion.

### 4.1.2 The difference equations

We consider a Crank-Nicolson finite difference scheme, which is one of the commonly used discretization methods for the Schrödinger equation. Let us introduce a polar and temporal grid  $r_{-1} < r_0 < r_1 < \dots < r_J < \dots$  with

$$\begin{aligned} r_{-1} &= -r_0; & r_{J-1/2} &= R; & r_{j+1/2} &= (r_{j+1} + r_j)/2; \\ \Delta r_{j+1/2} &= r_{j+1} - r_j; & \Delta r_j &= r_{j+1/2} - r_{j-1/2}; \\ \theta_k &= k\Delta\theta, & k &= 0, 1, \dots, K; & \Delta\theta &= 2\pi/K; \\ t_n &= n\Delta t, & n &\in \mathbb{N}_0. \end{aligned}$$

We denote

$$\psi_{j,k}^n = \psi(r_j, \theta_k, t_n), \quad \psi_{j,k}^{n+1/2} = (\psi_{j,k}^{n+1} + \psi_{j,k}^n)/2,$$

and  $V_{j,k}^{n+1/2} = V(r_j, \theta_k, t_{n+1/2})$ . Then the Crank-Nicolson scheme reads

$$\begin{aligned} & -\frac{2i}{\Delta t} (\psi_{j,k}^{n+1} - \psi_{j,k}^n) \\ &= \frac{1}{r_j} \frac{1}{\Delta r_j} \left[ \frac{r_{j+1/2}(\psi_{j+1,k}^{n+1/2} - \psi_{j,k}^{n+1/2})}{\Delta r_{j+1/2}} - \frac{r_{j-1/2}(\psi_{j,k}^{n+1/2} - \psi_{j-1,k}^{n+1/2})}{\Delta r_{j-1/2}} \right] \\ & \quad + \frac{1}{r_j^2} \frac{\psi_{j,k+1}^{n+1/2} - 2\psi_{j,k}^{n+1/2} + \psi_{j,k-1}^{n+1/2}}{\Delta \theta^2} - 2V_{j,k}^{n+1/2} \psi_{j,k}^{n+1/2}, \\ & \quad j \in \mathbb{N}_0 \quad k = 0, 1, \dots, K-1; \quad n \in \mathbb{N}_0. \end{aligned} \tag{4.6}$$

**Remark 4.1 (Treatment of singularity at the origin)** *We use a radial off-set grid here such that the coefficient at  $\psi_{-1,k}^n$  is zero.*

This chapter is organized as follows. In §4.2 we prove the discrete mass conservation property of the Crank-Nicolson scheme and derive discrete TBCs (DTBCs) directly for the chosen numerical scheme using the  $\mathcal{Z}$ -transform. In the sequel we prove concisely the stability of the recurrence formulas used to obtain the convolution coefficients of the new DTBCs for a spatially dependent potential. In §4.3 we discuss the approximation of the convolution coefficients by a discrete sum of exponentials and present an efficient recursion for evaluating these approximate DTBCs. Finally, the numerical examples of §4.4 illustrate the accuracy, stability and efficiency of the proposed method.

## 4.2 DTBCs for circular domains

First we generate discrete transparent boundary conditions using exact solutions to the difference scheme (4.6) in the exterior domain  $r \geq R$ .

In order to reduce the problem to the simpler 1D case, the discrete Fourier method is used in  $\theta$ -direction. Due to the periodic boundary conditions in angular direction we have

$$\psi_{j,0}^n = \psi_{j,K}^n, \quad j, n \in \mathbb{N}_0,$$

and hence, we use the discrete Fourier transform of  $\psi_{j,k}^n$  in  $\theta$ -direction:

$$\hat{\psi}_{j,m}^n := \frac{1}{K} \sum_{k=0}^{K-1} \psi_{j,k}^n \exp\left(\frac{2\pi i k m}{K}\right), \quad m = 0, \dots, K-1, n \in \mathbb{N}_0. \tag{4.7}$$

## 4 DTBCs for the two dimensional Schrödinger equation on circular domains

The scheme (4.6) in the exterior domain  $j \geq J - 1$  then transforms into:

$$-\frac{2i}{\Delta t} \left( \hat{\psi}_{j,m}^{n+1} - \hat{\psi}_{j,m}^n \right) = \frac{1}{r_j} \frac{1}{\Delta r_j} \left[ \frac{r_{j+1/2} \left( \hat{\psi}_{j+1,m}^{n+1/2} - \hat{\psi}_{j,m}^{n+1/2} \right)}{\Delta r_{j+1/2}} - \frac{r_{j-1/2} \left( \hat{\psi}_{j,m}^{n+1/2} - \hat{\psi}_{j-1,m}^{n+1/2} \right)}{\Delta r_{j-1/2}} \right] - 2V_{j,m} \hat{\psi}_{j,m}^{n+1/2},$$

$$V_{j,m} := V_R + \frac{2 \sin^2 \left( \frac{\pi m}{K} \right)}{r_j^2 \Delta \theta^2}, \quad 0 \leq m \leq K - 1, n \in \mathbb{N}_0.$$

The modes  $\psi_m$ ,  $m = 0, \dots, K - 1$  are independent of each other in the exterior domain  $r \geq R$ . Therefore we can continue our analysis for each azimuth mode separately.

Thus, by omitting in the sequel the superscript  $m$  and the notation  $\hat{\cdot}$ , we will consider in the exterior domain the following discrete 1D Schrödinger equation with spatially dependent potential:

$$-\frac{2i \Delta r_j \Delta r_{j+1/2}}{\Delta t} (\psi_j^{n+1} - \psi_j^n)$$

$$= \frac{1}{r_j} \left[ r_{j+1/2} \left( \psi_{j+1}^{n+1/2} - \psi_j^{n+1/2} \right) - r_{j-1/2} \frac{\Delta r_{j+1/2}}{\Delta r_{j-1/2}} \left( \psi_j^{n+1/2} - \psi_{j-1}^{n+1/2} \right) \right]$$

$$- 2 \Delta r_j \Delta r_{j+1/2} V_j \psi_j^{n+1/2}, \quad j \geq J - 1 \quad (4.8)$$

with

$$V_j = V_R + \frac{C}{(j + 0.5)^2}, \quad C = \frac{2 \sin^2 \left( \frac{\pi m}{K} \right)}{\Delta r^2 \Delta \theta^2}.$$

### 4.2.1 Mass conservation property

There are two important advantages of this second order (in  $\Delta r$  and  $\Delta t$ ) scheme (4.8). It is unconditionally stable, and it preserves the discrete  $L^2$ -norm in time:

**Lemma 4.1** *For the scheme (4.8) (considered on  $j \in \mathbb{N}_0$ ) holds, that*

$$\|\psi^n\|_2^2 := \sum_{j \in \mathbb{N}_0} \Delta r_j |\psi_j^n|^2 r_j \quad (4.9)$$

*is a conserved quantity in time.*

**Proof:** This conservation property can be seen by a discrete energy estimate. First we multiply (4.8) by  $\bar{\psi}_j^n r_j$  and its complex conjugate by  $\psi_j^{n+1} r_j$  and regard the whole domain:

$$\begin{aligned} & -\frac{2i}{\Delta t} (\psi_j^{n+1} \bar{\psi}_j^n - |\psi_j^n|^2) r_j \\ & = \bar{\psi}_j^n D^0(r_j D^0 \psi_j^n) - 2V_j \psi_j^n \bar{\psi}_j^n r_j, \quad j = 0, 1, \dots, \end{aligned} \quad (4.10)$$

and

$$\begin{aligned} & \frac{2i}{\Delta t} (|\psi_j^{n+1}|^2 - \bar{\psi}_j^n \psi_j^{n+1}) r_j \\ & = \psi_j^{n+1} D^0(r_j D^0 \bar{\psi}_j^n) - 2V_j \bar{\psi}_j^n \psi_j^{n+1} r_j, \quad j = 0, 1, \dots \end{aligned} \quad (4.11)$$

with the abbreviation of the centered difference quotient

$$D^0 = D^0_{\frac{\Delta r_j}{2}}, \text{ i.e. } D^0 \psi_j^n = \frac{\psi_{j+1/2}^n - \psi_{j-1/2}^n}{\Delta r_j}.$$

Next we subtract (4.10) from (4.11):

$$\begin{aligned} & \frac{2i}{\Delta t} (|\psi_j^{n+1}|^2 - |\psi_j^n|^2) r_j = \psi_j^{n+1} D^0(r_j D^0 \bar{\psi}_j^n) \\ & \quad - \bar{\psi}_j^n D^0(r_j D^0 \psi_j^n) - V_j (|\psi_j^{n+1}|^2 - |\psi_j^n|^2) r_j, \quad j = 0, 1, \dots, \end{aligned}$$

sum from  $j = 0$  to  $\infty$ , and apply summation by parts:

$$\begin{aligned} & \frac{2i}{\Delta t} \sum_{j=0}^{\infty} (|\psi_j^{n+1}|^2 - |\psi_j^n|^2) r_j \\ & = - \sum_{N_0 + \frac{1}{2}}^{\infty} (D^0 \bar{\psi}_j^n) (D^0 \psi_j^{n+1}) r_j - (D^0 \bar{\psi}_{-\frac{1}{2}}^n) \psi_0^{n+1} r_{-\frac{1}{2}} \\ & \quad + \sum_{N_0 + \frac{1}{2}}^{\infty} (D^0 \psi_j^n) (D^0 \bar{\psi}_j^n) r_j - (\psi_{-\frac{1}{2}}^n) \bar{\psi}_0^n r_{-\frac{1}{2}} \\ & \quad - \sum_{j=0}^{\infty} V_j (|\psi_j^{n+1}|^2 - |\psi_j^n|^2) r_j. \end{aligned} \quad (4.12)$$

## 4 DTBCs for the two dimensional Schrödinger equation on circular domains

The boundary terms in (4.12) vanish since  $r_{-\frac{1}{2}} = 0$  and we get

$$\begin{aligned} & \frac{2i}{\Delta t} \sum_{j=0}^{\infty} (|\psi_j^{n+1}|^2 - |\psi_j^n|^2) r_j \\ &= - \sum_{\mathbb{N}_0 + \frac{1}{2}}^{\infty} (|D^0 \bar{\psi}_j^{n+1}|^2 - |D^0 \bar{\psi}_j^n|^2) r_j - \sum_{j=0}^{\infty} V_j (|\psi_j^{n+1}|^2 - |\psi_j^n|^2) r_j. \end{aligned}$$

By taking imaginary parts one obtains the desired result. □

### 4.2.2 DTBCs for a single azimuth mode

Discrete transparent boundary conditions the 1D plane Schrödinger equation with constant coefficients of the difference scheme in the exterior domain were introduced by Arnold in [Ar95]. Here we derive DTBCs for spatially varying coefficients for the equation (4.8).

We use the  $\mathcal{Z}$ -transformation of the sequence  $\{\psi_j^n\}$ ,  $n \in \mathbb{N}_0$  (with  $j$  considered fixed) which is defined as the Laurent series, see [Do67]:

$$\mathcal{Z}\{\psi_j^n\} = \Phi_j(z) := \sum_{n=0}^{\infty} \psi_j^n z^{-n}, \quad z \in \mathbb{C}, \quad |z| > R_{\Phi_j},$$

and  $R_{\Phi_j}$  denotes the convergence radius of the series. Now the transformed exterior scheme (4.8) reads

$$\begin{aligned} & -i\rho_j \frac{z-1}{z+1} \Phi_j(z) \\ &= \frac{1}{r_j} \left[ r_{j+1/2} (\Phi_{j+1}(z) - \Phi_j(z)) - r_{j-1/2} \frac{\Delta r_{j+1/2}}{\Delta r_{j-1/2}} (\Phi_j(z) - \Phi_{j-1}(z)) \right] \\ & \quad - 2\Delta r_j \Delta r_{j+1/2} V_j \Phi_j(z), \quad j \geq J-1, \end{aligned}$$

with the mesh ratio  $\rho_j = 4\Delta r_j \Delta r_{j+1/2} / \Delta t$  and  $V_j = V_R + C/(j+0.5)^2$ . Thus we obtain a homogeneous second order difference equation with varying coefficients of the form

$$a_j \Phi_{j+1}(z) + b_j(z) \Phi_j(z) + c_j \Phi_{j-1}(z) = 0, \quad j \geq J-1, \quad (4.13)$$

with the coefficients

$$a_j = \frac{r_{j+1/2}}{r_j},$$

$$\begin{aligned}
 b_j(z) &= -\frac{1}{r_j} \left[ r_{j+1/2} + r_{j-1/2} \frac{\Delta r_{j+1/2}}{\Delta r_{j-1/2}} \right] + i\rho_j \frac{z-1}{z+1} - 2\Delta r_j \Delta r_{j+1/2} V_j, \\
 c_j &= \frac{r_{j-1/2} \Delta r_{j+1/2}}{r_j \Delta r_{j-1/2}}.
 \end{aligned} \tag{4.14}$$

**Remark 4.2 (uniform offset grid)** *In the special case of a uniform radial offset grid  $r_j = (j + \frac{1}{2})\Delta r$ ,  $j \geq J - 1$ , we obtain*

$$\begin{aligned}
 a_j &= \frac{j+1}{j+\frac{1}{2}}, \quad c_j = \frac{j}{j+\frac{1}{2}}, \\
 b_j(z) &= -2 + i\rho \frac{z-1}{z+1} - 2\Delta r^2 V_R - 4 \frac{\sin^2\left(\frac{\pi m}{K}\right)}{(j+1/2)\Delta\theta^2}.
 \end{aligned}$$

For the formulation of the  $\mathcal{Z}$ -transformed DTBCs at  $j = J$  we regard the ratio  $\hat{\ell}_j(z)$  of the solutions at two adjacent points:

$$\hat{\ell}_j(z) = \frac{\Phi_j(z)}{\Phi_{j-1}(z)}, \quad j \geq J. \tag{4.15}$$

From (4.13) we obtain the equation

$$\hat{\ell}_j(z) \left( a_j \hat{\ell}_{j+1}(z) + b_j(z) \right) + c_j = 0, \quad j \geq J. \tag{4.16}$$

Suppose that the coefficients  $\hat{\ell}_j(z)$  are known. Setting  $j = J + 1$  we get from (4.15):

$$\hat{\ell}_{J+1}(z) = \frac{\Phi_{J+1}(z)}{\Phi_J(z)}.$$

Calculating the inverse  $\mathcal{Z}$ -transformation we obtain the discrete convolution

$$\psi_{J+1}^n = \ell_{J+1}^n * \psi_J^n,$$

hence

$$\psi_{J+1}^n - \ell_{J+1}^{(0)} \psi_J^n = \sum_{p=1}^{n-1} \ell_{J+1}^{(n-p)} \psi_J^{(p)}$$

and finally

$$\psi_{J+1}^n - s^{(0)} \psi_J^n = \sum_{p=1}^{n-1} s^{(n-p)} \psi_J^{(p)} - \psi_{J+1}^{(n-1)},$$

## 4 DTBCs for the two dimensional Schrödinger equation on circular domains

---

with the *summed convolution coefficients*

$$\begin{aligned} s^{(0)} &:= \ell_{J+1}^{(0)}, \\ s^{(n)} &:= \ell_{J+1}^{(n)} + \ell_{J+1}^{(n-1)}, \quad n \geq 1. \end{aligned} \quad (4.17)$$

Note that these summed coefficients are introduced due to the observed oscillatory behaviour of the convolution coefficients  $\ell_{J+1}^{(n)}$  (cf. §2, [EhAr01]). Hence the DTBCs for the single azimuth mode read

$$\psi_{J+1}^n - s^{(0)}\psi_J^n = \sum_{p=1}^{n-1} s^{(n-p)}\psi_J^{(p)} - \psi_{J+1}^{(n-1)}. \quad (4.18)$$

### 4.2.3 Calculation of the convolution coefficients

In order to find a solution to (4.16) we use the *method of series*. Let us consider the Laurent series for  $\hat{\ell}_j(z)$ :

$$\hat{\ell}_j(z) = \ell_j^{(0)} + \ell_j^{(1)}z^{-1} + \dots + \ell_j^{(n)}z^{-n} + \dots, \quad |z| \geq 1. \quad (4.19)$$

With the auxiliary functions

$$\begin{aligned} \alpha_j(z) &:= \frac{b_j(z)}{a_j}, \\ \alpha_j &:= \lim_{z \rightarrow \infty} \alpha_j(z), \\ \beta_j &:= \frac{c_j}{a_j}. \end{aligned}$$

equation (4.16) reads

$$\hat{\ell}_j(z) \left( \hat{\ell}_{j+1}(z) + \alpha_j(z) \right) + \beta_j = 0, \quad j \geq J. \quad (4.20)$$

Substituting (4.19) for (4.20) we get

$$\begin{aligned} &(\ell_j^{(0)} + \ell_j^{(1)}z^{-1} + \dots + \ell_j^{(n)}z^{-n} + \dots) \\ &\cdot \left( (\ell_{j+1}^{(0)} + \ell_{j+1}^{(1)}z^{-1} + \dots + \ell_{j+1}^{(n)}z^{-n} + \dots) + \alpha_j(z) \right) + \beta_j = 0. \end{aligned} \quad (4.21)$$

**Coefficient  $\ell_j^{(0)}$ .** Taking  $|z| \rightarrow \infty$  we have the recurrence equation

$$\ell_j^{(0)}(\ell_{j+1}^{(0)} + \alpha_j) + \beta_j = 0. \quad (4.22)$$

for  $\ell_j^{(0)}$ . We shall solve this equation by “iteration from infinity”, i.e. starting from an index  $J_\infty$ , putting a boundary value  $\ell_{J_\infty}^{(0)} := \ell_\infty^{(0)}$ , and running the recursion from  $J_\infty$  to  $J$ :

$$\ell_j^{(0)} = \frac{-\beta_j}{\ell_{j+1}^{(0)} + \alpha_j}, \quad j = J_\infty - 1, J_\infty - 2, \dots, J. \quad (4.23)$$

Note that a very large index  $J$  corresponds to a very large radius  $r_{J_\infty}$ ; therefore we can use the 1D plane case coefficient  $\ell^{(0)}$ , see [ArEhSo03], as the starting value  $\ell_\infty^{(0)}$ .

**Theorem 4.2 (stability of the recurrence relations)** *Let  $|\alpha_j| \geq 2 > \beta_j + 1$ . Then:*

- (i)  $|\ell_j^{(0)}| < \beta_j < 1$ ; and
- (ii) *the recurrence formula (4.23) is stable with respect to small perturbations.*

**Proof:** The item (i) is proved by induction. Suppose  $|\ell_{j+1}^{(0)}| < \beta_{j+1}$ . Hence

$$|\ell_{j+1}^{(0)} + \alpha_j| - \beta_j \geq |\alpha_j| - |\ell_{j+1}^{(0)}| - \beta_j > 1 - |\ell_{j+1}^{(0)}| > 0.$$

Therefore we obtain  $|\ell_j^{(0)}| < 1$ . Furthermore we have

$$|\ell_j^{(0)}| = \frac{\beta_j}{|\ell_{j+1}^{(0)} + \alpha_j|} < \frac{\beta_j}{2 - |\ell_{j+1}^{(0)}|} < \beta_j. \quad (4.24)$$

To prove (ii) and establish the stability we suppose that we have a perturbation  $\ell_{j+1}^{(0)} + \delta_{j+1}$  instead of  $\ell_{j+1}^{(0)}$  with  $|\delta_{j+1}| < 1$ . Let us look at the evolution of  $\delta_j$  by comparing (4.23) with

$$\ell_j^{(0)} + \delta_j = \frac{-\beta_j}{\ell_{j+1}^{(0)} + \delta_{j+1} + \alpha_j}, \quad j = J_\infty - 1, J_\infty - 2, \dots, J.$$

Evidently we obtain

$$\begin{aligned} \delta_j &= \frac{-\beta_j}{\ell_{j+1}^{(0)} + \delta_{j+1} + \alpha_j} - \frac{-\beta_j}{\ell_{j+1}^{(0)} + \alpha_j} = \delta_{j+1} \frac{-\ell_j^{(0)}}{\ell_{j+1}^{(0)} + \delta_{j+1} + \alpha_j} \\ &= \delta_{j+1} \frac{-\ell_j^{(0)}}{-\beta_j/\ell_j^{(0)} + \delta_{j+1}}. \end{aligned}$$

## 4 DTBCs for the two dimensional Schrödinger equation on circular domains

---

Therefore we get

$$\begin{aligned} |\delta_j| &= |\delta_{j+1}| \frac{|\ell_j^{(0)}|}{|\beta_j/\ell_j^{(0)} + \delta_{j+1}|} < |\delta_{j+1}| \frac{|\ell_j^{(0)}|^2}{\beta_j - |\ell_j^{(0)}||\delta_{j+1}|} \\ &< |\delta_{j+1}| \frac{|\ell_j^{(0)}|^2}{\beta_j} \frac{1}{1 - |\delta_{j+1}|}, \end{aligned}$$

and hence

$$\frac{|\delta_j|}{|\delta_{j+1}|} \sim \frac{|\ell_j^{(0)}|^2}{\beta_j} < \beta_j < 1, \quad (4.25)$$

for  $|\delta_{j+1}| < 1$ . Thus the recursion (4.23) is stable with respect to small perturbations (e.g. for truncation errors or for an “incorrect” initial guess  $\ell_{J_\infty}^{(0)} := \ell_\infty^{(0)}$ ).

□

**Remark 4.3** *The theorem condition  $|\alpha_j| \geq 2 > \beta_j + 1$  is valid for the definitions (4.14).*

**Remark 4.4** *The estimate (4.25) permits to explain a fast convergence of the recursion (4.23) to the correct value  $\ell_j^{(0)}$  while taking an “incorrect” initial guess  $\ell_{J_\infty}^{(0)} := \ell_\infty^{(0)}$ , see the numerical examples below. Indeed, due to (4.25) we can hope for the exponential decay of  $|\delta_j|$  with the factor  $|\ell_j^{(0)}|^2/\beta_j \sim |\ell_j^{(0)}|$ . For instance the value  $|\ell_j^{(0)}|$  is estimated from the case of the “frozen” coefficients at  $J_\infty$ :*

$$|\ell_j^{(0)}| \sim |\ell_\infty^{(0)}|,$$

where  $|\ell_\infty^{(0)}| < 1$  is the root of the square equation

$$\ell_\infty^{(0)} = \frac{-\beta_{J_\infty}}{\ell_\infty^{(0)} + \alpha_{J_\infty}}.$$

**Coefficient  $\ell_j^{(1)}$ .** Now we consider the calculation of  $\ell_j^{(1)}$ . We have from (4.14):

$$\alpha_j(z) := \alpha_j - \gamma_j(z^{-1} - z^{-2} + z^{-3} - \dots), \quad (4.26)$$

with  $\gamma_j := \alpha_j - \bar{\alpha}_j$ . From (4.21) and (4.26) we can write

$$\begin{aligned} &(\ell_j^{(0)} + \ell_j^{(1)}z^{-1} + \mathcal{O}(z^{-2})) \\ &\cdot \left( (\ell_{j+1}^{(0)} + \ell_{j+1}^{(1)}z^{-1} + \mathcal{O}(z^{-2})) + (\alpha_j - \gamma_j z^{-1} + \mathcal{O}(z^{-2})) \right) + \beta_j = 0. \end{aligned} \quad (4.27)$$

Annihilating leading terms subjected to (4.22) we collect terms with factor  $z^{-1}$  and obtain after multiplying by  $z$  and considering  $|z| \rightarrow \infty$ :

$$\ell_j^{(0)} \ell_{j+1}^{(1)} - \ell_j^{(0)} \gamma_j + \ell_j^{(1)} \ell_{j+1}^{(0)} + \ell_j^{(1)} \alpha_j = 0.$$

Therefore the recursion is defined by

$$\ell_j^{(1)} = -\frac{\ell_j^{(0)} \ell_{j+1}^{(1)} - \ell_j^{(0)} \gamma_j}{\ell_{j+1}^{(0)} + \alpha_j}, \quad j = J_\infty - 1, J_\infty - 2, \dots, J \quad (4.28)$$

with a boundary value  $\ell_{J_\infty}^{(1)} := \ell_\infty^{(1)}$ .

**Coefficient  $\ell_j^{(n)}$ .** The case of  $\ell_j^{(n)}$  with  $n \geq 2$  is considered similarly by truncating terms of  $\mathcal{O}(z^{-n-1})$  in (4.27). We get the recursion formula

$$\ell_j^{(n)} = -\frac{\sum_{k=0}^{n-1} \ell_j^{(k)} \ell_{j+1}^{(n-k)} + \gamma_j (-1)^{n-k} \ell_j^{(k)}}{\ell_{j+1}^{(0)} + \alpha_j}, \quad j = J_\infty - 1, J_\infty - 2, \dots, J \quad (4.29)$$

with a boundary value  $\ell_{J_\infty}^{(n)} := \ell_\infty^{(n)}$  that can be taken with  $\ell_\infty^{(n)} \equiv \ell^{(n)}$  from the 1D plane case. Notice that (4.28) is a particular case of (4.29) at  $n = 1$ .

**Theorem 4.3** *Under conditions of Theorem 4.2 the recurrence formula (4.29) is stable with respect to small perturbations.*

**Proof:** Let us write (4.29) in the resolution form with respect to index  $n$ :

$$\ell_j^{(n)} = \frac{\ell_j^{(0)}}{\ell_{j+1}^{(0)} + \alpha_j} \ell_{j+1}^{(n)} + F\left(\{\ell_j^{(n_1 < n)}\}, \{\ell_{j+1}^{(n_1 < n)}\}\right),$$

$$j = J_\infty - 1, J_\infty - 2, \dots, J,$$

where the function  $F$  contains the remaining terms with indexes  $n_1 < n$ . Suppose that the coefficients  $\{\ell_j^{(n_1)}\}$ ,  $n_1 = 0, 1, \dots, n-1$ ,  $j = J_\infty - 1, J_\infty - 2, \dots, J$  are exact (or they are known with a good accuracy). Then the stability of (4.29) is determined by the magnitude of the multiplier

$$\frac{\ell_j^{(0)}}{\ell_{j+1}^{(0)} + \alpha_j}.$$

From (4.24) we get

$$\frac{|\ell_j^{(0)}|}{|\ell_{j+1}^{(0)} + \alpha_j|} < \frac{\beta_j}{|\ell_{j+1}^{(0)} + \alpha_j|} < \frac{\beta_j}{2 - |\ell_{j+1}^{(0)}|} < \beta_j < 1.$$

□

## 4 DTBCs for the two dimensional Schrödinger equation on circular domains

**Remark 4.5** *The proof of Theorem 4.3 is made by induction w.r.t.  $n \in \mathbb{N}$  at the assumption that the previous coefficients for  $n_1 < n$  are correct. In the practice, while calculating the coefficients  $\ell_j^{(n)}$ , we must fix some value  $J_\infty$  and take an “incorrect” boundary value  $\ell_{J_\infty}^{(n)} := \ell_\infty^{(n)}$ . This could give a numerical instability. However, due to sufficiently fast convergence of  $\ell_j^{(0)}$  to its correct value, say after several first  $J_0$  steps of the recursion (4.23), we can start the recursion run of  $\ell_j^{(1)}$  a little bit later, i.e. with the delay  $j = J_\infty - J_0$ . Similarly for  $\ell_j^{(1)}$  the initial index can be  $j = J_\infty - 2J_0$ , etc. In our numerical tests the usual value  $J_0$  is  $0 \leq J_0 \leq 5$ .*

### 4.2.4 Examples of the calculation of coefficients $\ell_j^{(n)}$

We demonstrate the efficiency of the proposed algorithm on the following setup. For the radius we consider  $R = 1$  and we discretize the circular domain  $[0, R] \times [0, 2\pi]$  with the uniform step sizes  $\Delta r = 1/200$  and  $\Delta\theta = 2\pi/200$ . For the time step size we take  $\Delta t = 0.0003$  and calculate the convolution coefficients  $\ell_j^{(n)}$  (cf. (4.29)) for the Schrödinger equation with a potential  $V = 0$  for the time steps  $n = 0, \dots, 60$ . In a first set of calculations we run the algorithm with a choice  $J_\infty = 550$  (which corresponds to  $r = 3.75$ ) and a retarding shift  $J_0 = 5$ . Here we just discuss the graphs for the mode  $m = 1$ , all other modes behave similarly. In Figure 4.1 we show the absolute values of the last 7 coefficients  $\ell_j^{(54)}, \dots, \ell_j^{(60)}$  as a function of  $r \in [R, 3.75]$ . We observe a good convergence of the coefficients while approaching the artificial boundary  $R = 1$  from the exterior domain. An estimation of the residual is done by a second set of calculations, where we obtain convolution coefficients  $\tilde{\ell}_j^{(n)}$  with  $J_\infty = 1100$ . The difference  $|\ell_j^{(n)} - \tilde{\ell}_j^{(n)}|$  for the same discretization data is plotted for  $n = 54, \dots, 60$  in Figure 4.2. With values of the order  $\mathcal{O}(10^{-14})$  near the artificial boundary  $R = 1$  this error is about the rounding error of Matlab. The influence of the retarding shift parameter  $J_0$  can be estimated by comparing Figure 4.1 with Figure 4.3. In the third run we determine the convolution coefficients with the same discretization parameters as in the first test (presented in Figure 4.1) but with a smaller choice  $J_0 = 3$ . The absolute values of these convolution coefficients are presented in Figure 4.3. The oscillations in  $\ell_j^{(n)}$  due to the instability near  $J_\infty$  in this plot are more obvious than in the coefficients computed with  $J_0 = 5$  shown in Figure 4.1. But also for the choice  $J_0 = 3$  the coefficients converge while approaching  $r = R$ .

### 4.2.5 Two dimensional DTBCs for circular domains

In the Fourier transformed space, i.e. in terms of separate azimuthal modes, the DTBCs read (this is equation (4.18) with recovered index  $m$  and the notation  $\hat{\phantom{x}}$

## 4.2 DTBCs for circular domains

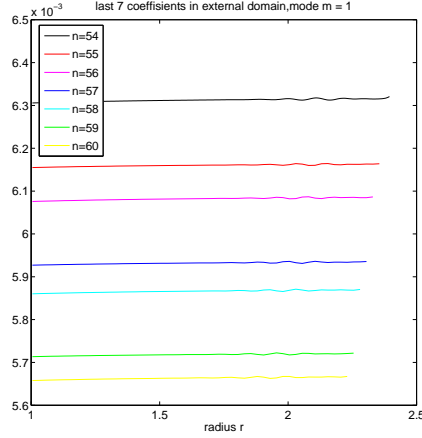


Figure 4.1: Absolute values of last 7 coefficients  $\ell_j^{(n)}$ ,  $n = 54, \dots, 60$ ,  $J_\infty = 550$ ,  $J_0 = 5$ ;  $m = 1$ .

for the Fourier transformation):

$$\hat{\psi}_{J+1,m}^n - s_m^{(0)} \hat{\psi}_{J,m}^n = \sum_{p=1}^{n-1} s_m^{(n-p)} \hat{\psi}_{J,m}^p - \hat{\psi}_{J+1,m}^{n-1}, \quad (4.30)$$

where  $m = 0, \dots, K-1$ ,  $n \geq 1$ .

In order to obtain DTBCs in the physical space let us introduce  $K \times K$  diagonal matrices

$$\mathbf{s}^{(p)} = \text{diag}\{s_m^{(p)}\}, \quad m = 0, \dots, K-1,$$

and also matrices  $\mathbf{F}$  and  $\mathbf{F}^{-1}$  of the direct and inverse Fourier transform, respectively, acting by

$$\hat{\psi}_j^n = \mathbf{F} \bar{\psi}_j^n$$

in accordance with (4.7). The vectors  $\hat{\psi}_j^n$ ,  $\bar{\psi}_j^n$  notate

$$\hat{\psi}_j^n = \{\hat{\psi}_{j,m}^n\}_{m=0}^{K-1}, \quad \bar{\psi}_j^n = \{\bar{\psi}_{j,k}^n\}_{k=0}^{K-1}.$$

Then, multiplying (4.30) by  $\mathbf{F}^{-1}$  we get the following 2D discrete TBCs:

$$\bar{\psi}_{J+1}^n - \mathbf{F}^{-1} \mathbf{s}^{(0)} \mathbf{F} \bar{\psi}_J^n = \mathbf{F}^{-1} \sum_{p=1}^{n-1} \mathbf{s}^{(n-p)} \mathbf{F} \bar{\psi}_J^p - \bar{\psi}_{J+1}^{n-1}. \quad (4.31)$$

## 4 DTBCs for the two dimensional Schrödinger equation on circular domains

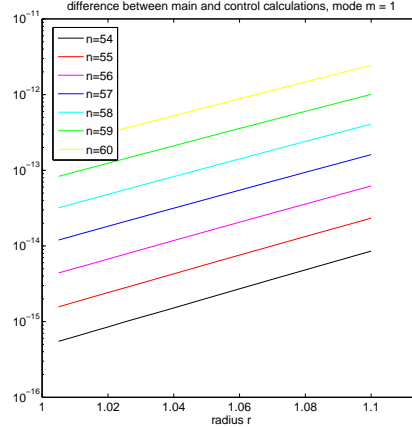


Figure 4.2: Absolute values of difference  $|\ell_j^{(n)} - \tilde{\ell}_j^{(n)}|$  of last 7 coefficients calculated with  $J_\infty = 550$  and  $J_\infty = 1100$ ;  $m = 1$ .

In order to formulate DTBCs as in (4.15) it is necessary that the discrete initial condition vanishes at the two adjacent (spatial) grid points appearing in (4.15). Here, we chose to formulate the DTBCs (4.31) at the boundary of the computational interval and one grid point in the *exterior domain*. Hence we have assumed that the initial condition satisfies  $\psi_{J,k}^{(0)} = \psi_{J+1,k}^{(0)} = 0$ ,  $k = 0, \dots, K - 1$ .

The use of the formulas (4.31) for calculations permits us to avoid any boundary reflections and it renders the fully discrete scheme unconditionally stable (just like the underlying Crank-Nicolson scheme). Note that we need to evaluate for each mode  $m$  just one convolution of (4.31) at each time step (at the endpoint of the interval  $[0, t_n]$ ). Since the other points of this convolution are not needed, using an FFT is not practical.

### 4.3 Approximation by sums of exponentials

An ad-hoc implementation of the discrete convolution

$$\sum_{p=0}^{n-1} s^{(n-p)} \psi_J^p$$

in (4.18) with convolution coefficients  $s^{(n)}$  from (4.17) has still one disadvantage. The boundary conditions are non-local both in time and space and therefore computations are expensive. As a remedy, to get rid of the time non-locality, the

### 4.3 Approximation by sums of exponentials

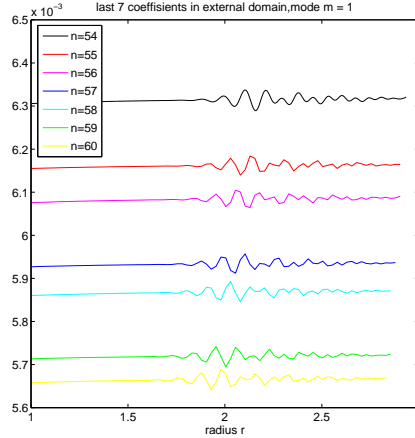


Figure 4.3: Absolute values of last 7 coefficients,  $J_\infty = 550$ ,  $J_0 = 3$ ;  $m = 1$ .

authors in [ArEhSo03] proposed the sum of exponentials ansatz. They approximated the kernel (4.17) by a finite sum (say  $L$  terms) of exponentials that decay with respect to time. This approach allows for a fast (approximate) evaluation of the discrete convolution (4.18) since the convolution can now be evaluated with a simple recurrence formula for  $L$  auxiliary terms and the numerical effort now stays constant in time.

Let us note that such kind of trick has been proposed in [GrSt90] for the heat equation and in [So93] for the continuous TBC in case of the 3D wave equation, and developed in [AlGrHa00], [So98a], [So98b], [DKSW01], [Ha99] for various hyperbolic problems. In the sequel we will briefly review the ansatz proposed in [ArEhSo03].

In order to derive a fast numerical method to calculate the discrete convolutions in (4.30), we approximate the coefficients  $s^{(n)}$  by the following *sum of exponentials* ansatz:

$$s^{(n)} \approx \tilde{s}^{(n)} := \begin{cases} s^{(n)}, & n = 0, 1, \dots, \nu - 1 \\ \sum_{l=1}^L b_l q_l^{-n}, & n = \nu, \nu + 1, \dots, \end{cases} \quad (4.32)$$

where  $L, \nu \in \mathbb{N}$  are a fixed numbers. Evidently, the approximation properties of  $\tilde{s}^{(n)}$  depend on  $L, \nu$ , and the corresponding set  $\{b_l, q_l\}$ . Thus, the choice of an (in some sense) optimal such approximation is a difficult nonlinear problem. Below we propose a deterministic method of finding  $\{b_l, q_l\}$  for fixed  $L$  and  $\nu$ .

**Remark 4.6** The “split” definition of  $\{\tilde{s}^{(n)}\}$  in (4.32) is motivated by the fact that the implementation of the DTBCs (4.30) involves a convolution sum with  $p$

## 4 DTBCs for the two dimensional Schrödinger equation on circular domains

ranging only from 1 to  $p = n - 1$ . Since the first coefficient  $s^{(0)}$  does not appear in this convolution, it makes no sense to include it in our sum of exponential approximation, which aims at simplifying the evaluation of the convolution. Hence, one may choose  $\nu = 1$  in (4.32). The “special form” of  $\ell_\infty^{(0)}$  and  $\ell_\infty^{(1)}$  given in [ArEhSo03] suggests even to exclude  $s^{(1)}$  from this approximation and to choose  $\nu = 2$  in (4.32). We use this choice in our numerical implementation in Example 3 in §4.4.

Also, there is an additional motivation for choosing  $\nu = 2$ : With the choice  $\nu = 0$  (or  $\nu = 1$ ) we typically obtain (for each mode) two (or, resp., one) coefficient pairs  $(b_l, q_l)$  of big magnitude. These “outlier” values reflect the different nature of the first two coefficients. Including them into our discrete sum of exponentials would then yield less accurate approximation results.

Let us fix  $L$  and consider the formal power series

$$g(x) := s^{(\nu)} + s^{(\nu+1)}x + s^{(\nu+2)}x^2 + \dots, \quad |x| \leq 1. \quad (4.33)$$

If there exists the  $[L - 1|L]$  Padé approximation

$$\tilde{g}(x) := \frac{P_{L-1}(x)}{Q_L(x)}$$

of (4.33), then its Taylor series

$$\tilde{g}(x) = \tilde{s}^{(\nu)} + \tilde{s}^{(\nu+1)}x + \tilde{s}^{(\nu+2)}x^2 + \dots$$

satisfies the conditions

$$\tilde{s}^{(n)} = s^{(n)}, \quad n = \nu, \nu + 1, \dots, 2L + \nu - 1, \quad (4.34)$$

due to the definition of the Padé approximation rule.

**Theorem 4.4** ([ArEhSo03]) *Let  $Q_L(x)$  have  $L$  simple roots  $q_l$  with  $|q_l| > 1$ ,  $l = 1, \dots, L$ . Then*

$$\tilde{s}^{(n)} = \sum_{l=1}^L b_l q_l^{-n}, \quad n = \nu, \nu + 1, \dots,$$

where

$$b_l := -\frac{P_{L-1}(q_l)}{Q'_L(q_l)} q_l \neq 0, \quad l = 1, \dots, L.$$

**Remark 4.7** *We remark that the assumption in Theorem 4.4 on the roots of  $Q_L(x)$  to be simple is not essential. For multiple roots one only has to reformulate Theorem 4.4. All our practical calculations confirm that this assumption holds for any desired  $L$ , although we cannot prove this.*

### 4.3 Approximation by sums of exponentials

---

Evidently, the approximation to the convolution coefficients  $s^{(n)}$  by the representation (4.32) using a  $[L - 1|L]$  Padé approximant to (4.33) behaves as follows. The first  $2L$  coefficients are reproduced exactly, see (4.34). However, the asymptotics of  $s^{(n)}$  and  $\tilde{s}^{(n)}$  (as  $n \rightarrow \infty$ ) differ strongly - algebraic versus exponential decay. A typical graph of  $|s_m^{(n)} - \tilde{s}_m^{(n)}|$  versus  $n$  for  $L = 40$  is shown in Figure 4.15 in §4.4.

#### 4.3.1 Fast evaluation of the discrete convolution

Let us consider the approximation (4.32) of the discrete convolution kernel appearing in the DTBCs (4.30) (again with suppressed index  $m$ ). With these “exponential” coefficients the *approximated convolution*

$$\tilde{C}_J^{(n-1)} := \sum_{p=1}^{n-1} \tilde{s}^{(n-p)} \psi_{J+1}^p, \quad \tilde{s}^{(n)} = \sum_{l=1}^L b_l q_l^{-n}, \quad |q_l| > 1 \quad (4.35)$$

of a discrete function  $\psi_{J+1}^p$ ,  $p = 1, 2, \dots$ , with the kernel coefficients  $\tilde{s}^{(n)}$ , can be calculated by recurrence formulas, and this will reduce the numerical effort significantly.

A straightforward calculation (cf. [ArEhSo03]) yields, that the value  $\tilde{C}_J^{(n-1)}$  from (4.35) for  $n \geq 2$  is represented by

$$\tilde{C}_J^{(n-1)} = \sum_{l=1}^L \tilde{C}_{J,l}^{(n-1)},$$

with

$$\begin{aligned} \tilde{C}_l^{(0)} &\equiv 0, \\ \tilde{C}_{J,l}^{(n-1)} &= q_l^{-1} \tilde{C}_{J,l}^{(n-2)} + b_l q_l^{-1} \psi_{J+1}^{n-2}, \quad n = 2, 3, \dots, l = 1, \dots, L. \end{aligned}$$

Finally we summarize the approach by the following algorithm for each azimuth mode  $m = 0, \dots, K - 1$ :

1. Calculate  $\ell_{J+1}^{(n)}$ ,  $n = 0, \dots, N - 1$ , with formulas (4.29) with a boundary value  $\ell_{J_\infty}^{(n)} := \ell_\infty^{(n)}$  that can be taken from the 1D plane case  $\ell_\infty^{(n)} \equiv \ell^{(n)}$  from [ArEhSo03], and use (4.17) to find  $s^{(n)}$ ;
2. Calculate  $\tilde{s}^{(n)}$  via Padé-algorithm;
3. The corresponding coefficients  $b_l$ ,  $q_l$  are used for the efficient calculation of the discrete convolutions.

## 4.4 Numerical results

In the following section we present some numerical results concerning the DTBCs.

### 4.4.1 Example 1

We recall the Example 2 from [HaHu04], i.e. we consider (4.1) with the vanishing potential  $V \equiv 0$  and the angle-dependent initial data

$$\psi^I(r, \theta) = \frac{e^{2ik_x r \cos \theta + 2ik_y r \sin \theta - \frac{(r \cos \theta)^2}{2\alpha_x} - \frac{(r \sin \theta)^2}{2\alpha_y}}}{\sqrt{\alpha_x \alpha_y}}, \quad r \in \mathbb{R}^+, 0 \leq \theta \leq 2\pi. \quad (4.36)$$

Then the exact solution to (4.1) for  $t > 0$  is given by the Gaussian beam

$$\psi(r, \theta, t) = \frac{e^{2ik_x(r \cos \theta - k_x t) + 2ik_y(r \sin \theta - k_y t) - \frac{(r \cos \theta - 2k_x t)^2}{2(\alpha_x + it)} - \frac{(r \sin \theta - 2k_y t)^2}{2(\alpha_y + it)}}}{\sqrt{\alpha_x + it} \sqrt{\alpha_y + it}}.$$

We set  $\alpha_x = \alpha_y = 0.04$ , let  $k_x = 1$ ,  $k_y = -1$  and calculate a solution  $\psi_1$  to (4.6) with an equidistant discretization on the circular computational domain  $\Omega_1 = [0, R] \times [0, 2\pi]$  with  $R = 1$  and  $J + 2$  grid points in  $r$ - and  $K$  in  $\theta$ -direction for times  $0 < t \leq 0.25$ . In order to satisfy the assumption, that the initial data is compactly supported in  $\Omega_1$  (cf. §4.2) we have to use a small numerical cut-off close to  $R$ ,  $\psi^I(r, \theta) = 0$  for  $r \geq R - \Delta r$  for all angles  $\theta$ , i.e. in discrete notation  $\psi_{j,k}^I = 0$  for  $j \geq J$ ,  $k = 0, \dots, K - 1$ . We remark that this assumption of compactly supported data is not essential; strategies to overcome this restriction can be found in [EhAr01]. Since we use an offset grid, DTBCs are implemented as described before (cf. §4.2.5) at  $r = R - \Delta r/2$ , between  $R$  and  $R - \Delta r$ . A reference solution  $\psi_2$  is calculated on the domain  $\Omega_2 = [0, 2R] \times [0, 2\pi]$  with discrete TBCs at  $r = 2R - \Delta r/2$ . For the determination of the error due to the scheme we compare the numerical solution  $\psi_2$  with the exact one  $\psi$  on  $\Omega_1$  and obtain the relative  $L^2$ -error

$$L_{\Omega_1}(\psi_2, \psi, t_n) = \frac{\left( \sum_{(r_j, \theta_k) \in \Omega_1} r_j |\psi_2(r_j, \theta_k, t_n) - \psi(r_j, \theta_k, t_n)|^2 \right)^{\frac{1}{2}}}{\max_{t_n} \left\{ \left( \sum_{(r_j, \theta_k) \in \Omega_1} r_j |\psi(r_j, \theta_k, t_n)|^2 \right)^{\frac{1}{2}} \right\}}, \quad (4.37)$$

which coincides with the error measured with the norm defined in (4.9). Within this test the error due to the cut-off of the initial function is also included. The effects of the boundary should be negligible here, because  $\psi_2$  does not cross the

boundary  $2R$  essentially for the calculated time steps.

In order to distinguish between the error due to the difference scheme and the error due to the DTBCs, we compare the numerical solution  $\psi_1$  with the numerical reference solution  $\psi_2$  and calculate the relative error  $L_{\Omega_1}(\psi_2, \psi_1, t_n)$  due to the boundary condition.

**Discretization and Results.** The solutions  $\psi_1$  and  $\psi_2$  are calculated for three parameter sets. First we let  $J = K = 64$ , i.e.  $\Delta r = 1/64$ ,  $\Delta\theta = 2\pi/64$  and  $\Delta t = 1/64$ , then  $\Delta r = \Delta t = 1/128$ ,  $\Delta\theta = 2\pi/128$  and finally  $\Delta r = \Delta t = 1/256$ ,  $\Delta\theta = 2\pi/256$ . These discretization parameters are taken from [HaHu04]. The relative error of the initial function due to the cut-off is about  $\mathcal{O}(10^{-6})$ ,  $\mathcal{O}(10^{-7})$ ,  $\mathcal{O}(10^{-7})$ , respectively. We present in Figure 4.4 the absolute value of the initial function (4.36) and of the evolution of the numerical solution  $\psi_1$  of (4.6) on the computational domain  $\Omega_1$  until  $t = 0.25$  for the last set of discretization parameters and a potential  $V = 0$ . As expected the Gaussian beam leaves the computational domain without any unphysical reflections. The same results are shown in Figure 4.5 as contour plots. Figure 4.6(a) shows the relative error  $L_{\Omega_1}(\psi_2, \psi, t_n)$  between the numerical solution  $\psi_2$  and the exact solution restricted on  $\Omega_1$  for the three sets of parameters. The relative error  $L_{\Omega_1}(\psi_1, \psi_2, t_n)$  due to the boundary condition is presented in Figure 4.6(b) also for all sets; with a values around  $\mathcal{O}(10^{-13})$  it amounts about the rounding error of Matlab.

**Remark 4.8** *The error due to the boundary may increase with finer discretizations. This depends on the iterative solver for linear systems of equations in Matlab. For abrasive discretizations, the system matrix has a better condition and the linear system of equations can be solved with higher accuracy.*

**Remark 4.9** *It is not possible to compare our results directly with the results retrieved in [HaHu04], because the not trivial aspect, how the TBCs have been discretized, is not mentioned there. The difference between the exact and the calculated solution in one point at the boundary presented in [HaHu04] was about 0.7 for  $\Delta r = \Delta t = 64$ , 0.2 for  $\Delta r = \Delta t = 128$  and 0.1 for  $\Delta r = \Delta t = 256$ . This error was not analysed more precisely.*

### 4.4.2 Example 2

We recall the numerical example from [AnBeMo04] and consider (4.1) with the vanishing potential  $V \equiv 0$  and the initial data

$$\psi^I(r, \theta) = e^{-ik_x r \cos \theta - \frac{\alpha}{2} r^2}, \quad r \in \mathbb{R}^+, 0 \leq \theta \leq 2\pi \quad (4.38)$$

with  $k_x = 5$ ,  $\alpha = 2$ .

## 4 DTBCs for the two dimensional Schrödinger equation on circular domains

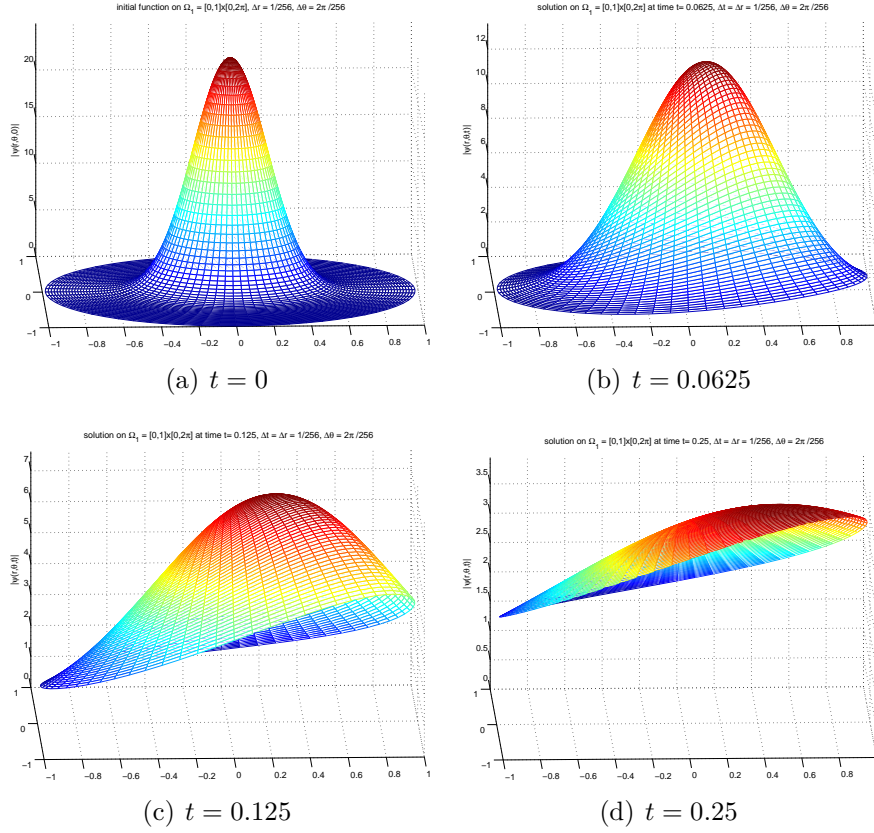


Figure 4.4: Example 1. Absolute value of the initial function ((4.36), with cut-off) and the calculated solution  $\psi_1$  of the discretization scheme (4.6) on the computational domain  $\Omega_1$  with  $\Delta r = \Delta t = 1/256$ ,  $\Delta\theta = 2\pi/256$ ,  $\alpha_x = \alpha_y = 0.04$  and the wave numbers  $k_x = -1$ ,  $k_y = 1$ . The potential equals 0; DTBCs are implemented at  $r = 1 - \Delta r/2$ .

The exact solution of (4.1) with this initial data is a Gaussian distribution

$$\psi(r, \theta, t) = \frac{1}{1 + i\alpha t} \exp\left(\frac{-\alpha r^2 + 2ik_x r \cos\theta - k_x^2 it}{2 + 2i\alpha t}\right)$$

moving into  $\theta = 180^\circ$  direction. Again we calculate a solution  $\psi_1$  of (4.6) for the initial data (4.38) with a cut-off close to the radius  $R = 2.5$  ( $\psi_{J,k}^I = \psi_{J+1,k}^I = 0$ ,  $k = 0, \dots, K-1$  on the discrete level) on a circular domain  $\Omega_1 = [0, R] \times [0, 2\pi]$  with an equidistant offset grid. Because of the offset grid the DTBCs are implemented between  $R$  and  $R - \Delta r$ . The solution  $\psi_1$  is compared with a numerical reference solution  $\psi_2$  calculated on  $[0, 2R] \times [0, 2\pi]$  as it has been described and done in Example 1. Moreover we compare the numerical solution  $\psi_2$  with the exact one  $\psi$  on  $\Omega_1$ .

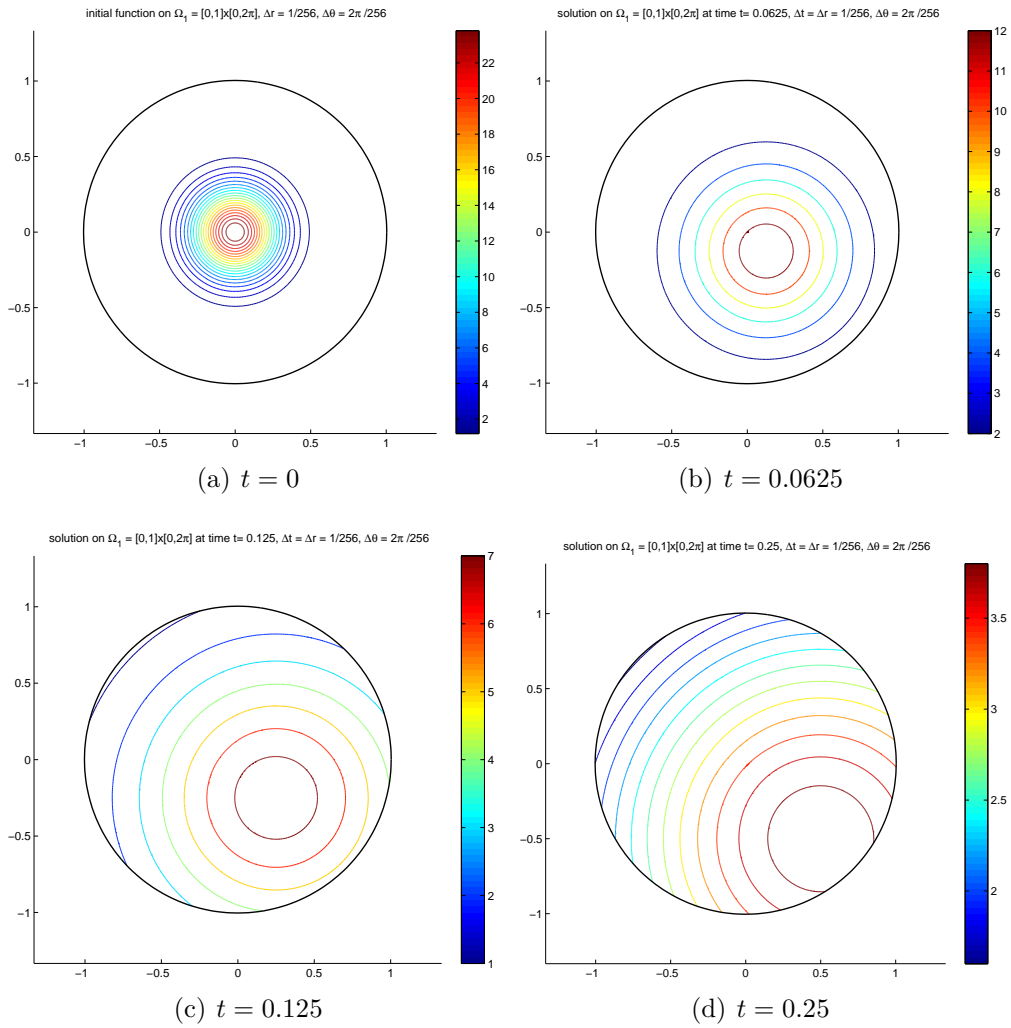
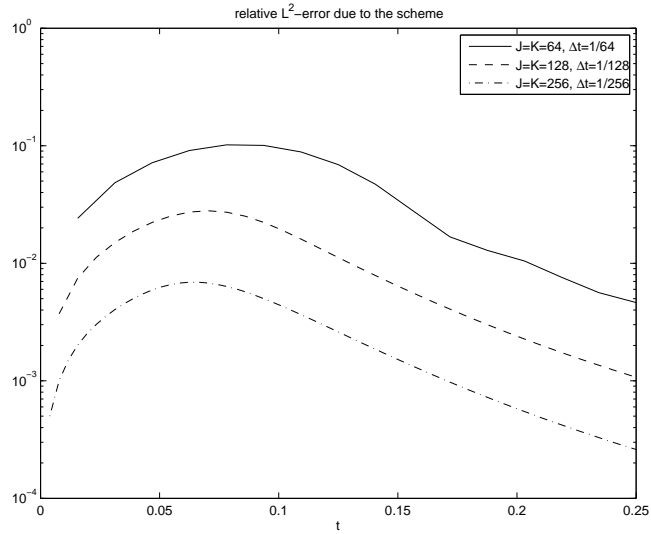
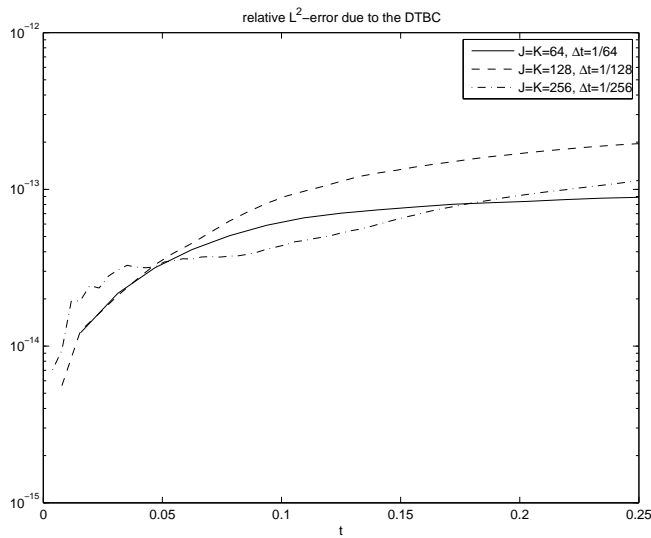


Figure 4.5: Example 1. Contour plot of the absolute value of the initial function ((4.36), with cut-off) and the calculated solution  $\psi_1$  of (4.6) on the computational domain  $\Omega_1$  for the same discretization parameters used in the calculations for Figure 4.4.

## 4 DTBCs for the two dimensional Schrödinger equation on circular domains



(a) error due to the scheme



(b) error due to the boundary condition

Figure 4.6: Example 1. (a): Relative error  $L_{\Omega_1}(\psi_2, \psi, t_n)$  due to the scheme and (b): relative error  $L_{\Omega_1}(\psi_1, \psi_2, t_n)$  due to the boundary conditions for the time evolution of initial function (4.36) for the three parameter sets with 64 (solid line), 128 (dashed line) and 256 grid points (dash-pointed line).

**Discretization and Results.** The numerical solutions in [AnBeMo04] are calculated with finite elements with 32768 and 57344 triangles and the time step size  $\Delta t = 0.01$ . We calculate numerical solutions again for three sets of parameters, first  $\Delta r = R/64$ ,  $\Delta\theta = 2\pi/64$ , then  $\Delta r = R/128$ ,  $\Delta\theta = 2\pi/128$  (which corresponds approximately to 32768 triangles) and finally  $\Delta r = R/256$ ,  $\Delta\theta = 2\pi/256$  (57344 triangles). For all sets we let  $\Delta t = 0.0025$  and solve (4.6) with the initial data (4.38) for  $k_x = -5$  until  $t = 0.5$ .

Figure 4.7 shows the absolute value of the initial function and of the evolution of the numerical solution  $\psi_1$  of (4.6) on the disc  $\Omega_1 = [0, 2.5] \times [0, 2\pi]$ . The Gaussian wave is leaving the computational domain without being reflected back at the artificial boundary  $R = 2.5$ . In Figure 4.8 we present the same results as contour plots. The relative error  $L_{\Omega_1}(\psi_2, \psi, t_n)$  due to the scheme and the relative error  $L_{\Omega_1}(\psi_1, \psi_2, t_n)$  due to the DTBCs are plotted in Figure 4.9. We remark that the error of the boundary is of order  $\mathcal{O}(10^{-14})$  and again about the rounding error of Matlab.

A further test concerns the long-time behaviour of the relative error due to the DTBCs and is also taken from [AnBeMo04]. Therefore we calculate numerical solutions  $\psi_1, \psi_2$  of (4.6) for the initial data (4.38) for  $k_x = 0$  on the circular domains  $\Omega_1 = [0, 2.5] \times [0, 2\pi]$ ,  $\Omega_2 = [0, 5] \times [0, 2\pi]$  until  $t = 4$  with the same spatial discretization parameters used above and the time step size  $\Delta t = 0.01$ , which coincides to the choice of  $\Delta t$  from [AnBeMo04]. In Figure 4.10 we show the relative error  $L_{\Omega_1}(\psi_1, \psi_2, t_n)$  due to the boundary conditions for this long-time test. For these long-time calculations with this coarser time step size the error due to the DTBCs stays bounded. We remark, that the relative error for the Gaussian solution was between  $\mathcal{O}(10^{-1})$  and  $\mathcal{O}(10^{-4})$  in [AnBeMo04]. Also there the error was not analyzed more precisely.

### 4.4.3 Example 3

To illustrate the sum of exponential ansatz we consider the numerical example from [JiGr06] and the initial Gaussian wave function

$$\psi^I(r, \theta) = \frac{e^{ir(k_x \cos \theta + k_y \sin \theta) - \frac{r^2}{4} \left( \frac{\cos^2 \theta}{\alpha_x} + \frac{\sin^2 \theta}{\alpha_y} \right)}}{\sqrt{\alpha_x \alpha_y}}, \quad r \in \mathbb{R}^*, \quad 0 \leq \theta \leq 2\pi. \quad (4.39)$$

The exact solution of the Schrödinger equation with the initial data (4.39) is known (cf. Example 1). For the numerical calculations we set  $\alpha_x = \alpha_y = 0.01$  and  $k_x = 5$ ,  $k_y = -5$ . A solution  $\psi_1$  of (4.6) with the initial data (4.39) with a cut-off at  $R - \Delta r$ , which causes a relative error of the order  $\mathcal{O}(10^{-12})$ , is calculated on the circular domain  $\Omega_1 = [0, R] \times [0, 2\pi]$  with the radius  $R = 1$ . The absolute value

## 4 DTBCs for the two dimensional Schrödinger equation on circular domains

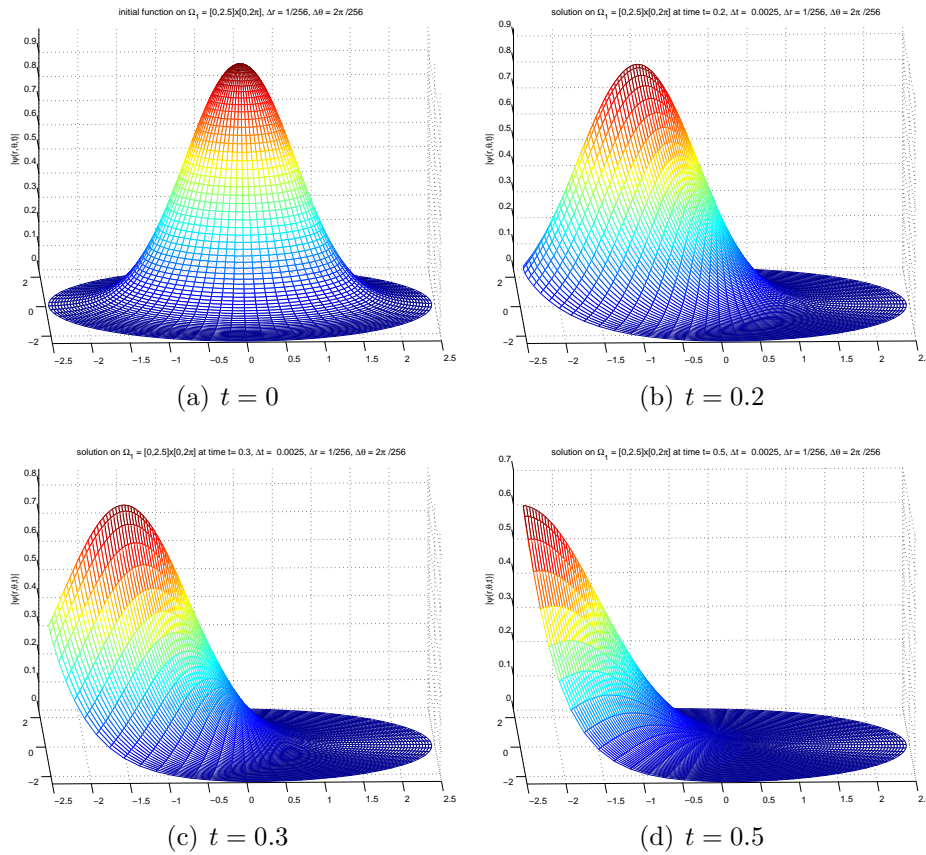


Figure 4.7: Example 2. Absolute value of the numerical solution  $\psi_1$  of (4.6) with the initial function ((4.38), with cut-off) on the computational domain  $\Omega_1$  with  $\Delta r = R/256$ ,  $\Delta \theta = 2\pi/256$ ,  $\Delta t = 0.0025$ ,  $\alpha = 2$  and the wave number  $k_x = -5$ . The potential equals 0; DTBCs are implemented at  $R - \Delta r/2$ .

## 4.4 Numerical results

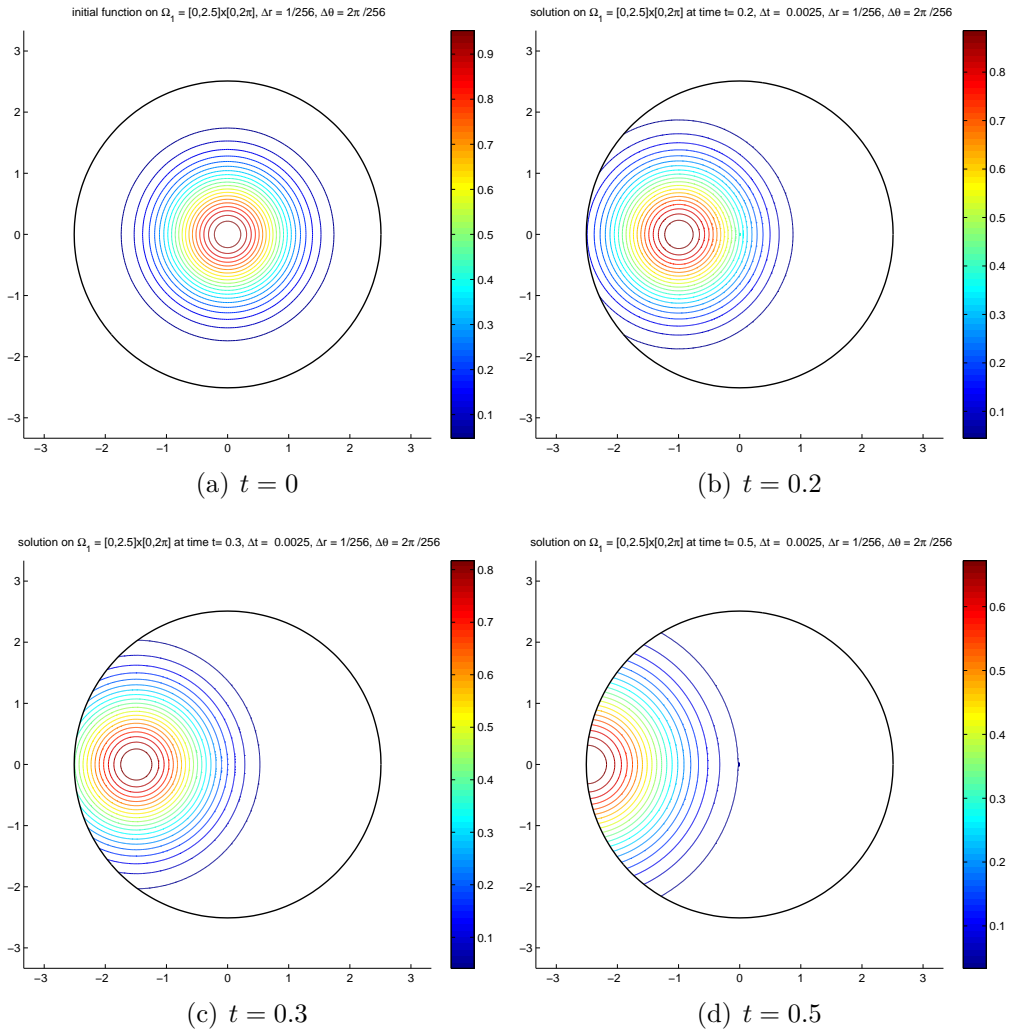
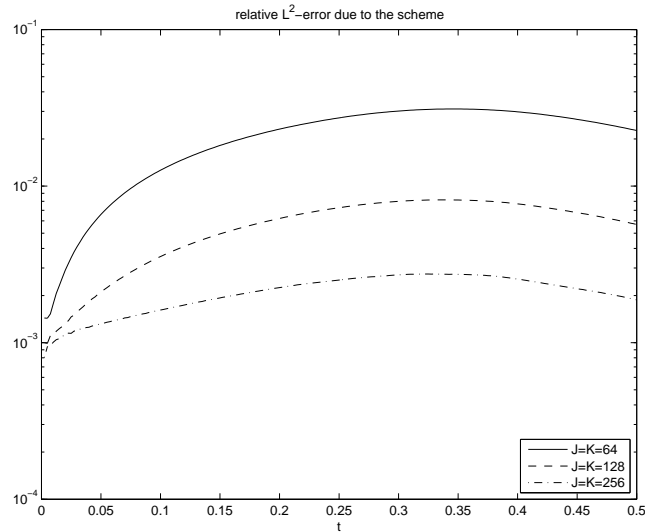
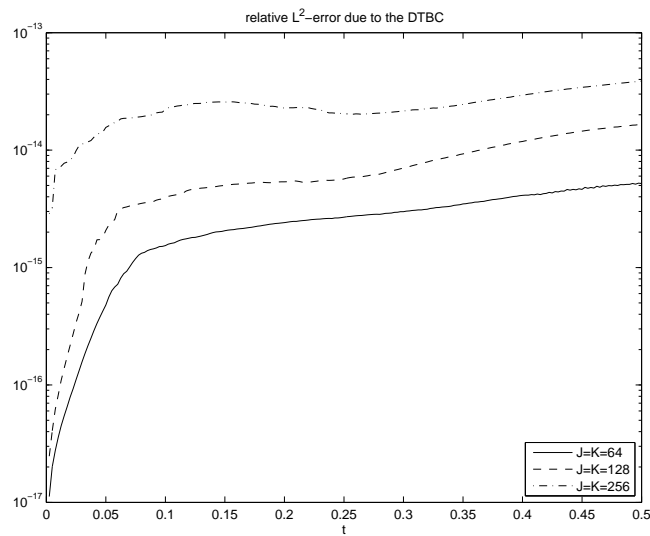


Figure 4.8: Example 2. Contour plot of the absolute value of the initial function ((4.38), with cut-off) and the calculated solution  $\psi_1$  of (4.6) on the computational domain  $\Omega_1$  for the same discretization parameters used in the calculations for Figure 4.7.

## 4 DTBCs for the two dimensional Schrödinger equation on circular domains



(a) error due to the scheme



(b) error due to the boundary condition

Figure 4.9: Example 2. (a): Relative error  $L_{\Omega_1}(\psi_2, \psi, t_n)$  due to the scheme and (b): relative error  $L_{\Omega_1}(\psi_1, \psi_2, t_n)$  due to the boundary conditions for the time evolution of initial function (4.38) for the three parameter sets with 64 (solid line), 128 (dashed line) and 256 grid points (dashed-pointed line).

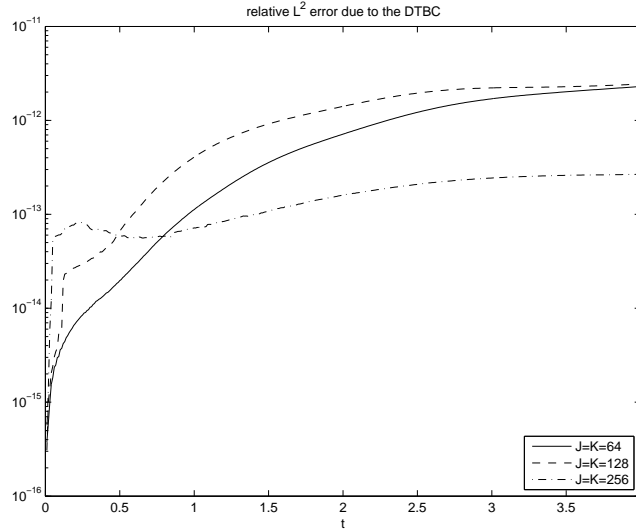


Figure 4.10: Example 2. Relative error  $L_{\Omega_1}(\psi_1, \psi_2, t_n)$  due to the boundary condition for the time evolution of initial function (4.38) with  $k_x = 0$ ,  $\alpha = 2$  for the three parameter sets with 64 (solid line), 128 (dashed line) and 256 grid points (dashed-pointed line). For all three sets we let  $\Delta t = 0.01$ .

of the initial function (4.39) and its contour plot is shown in Figure 4.11. For the DTBCs we use the approximation (4.35). As a numerical reference solution we take  $\psi_2$ , which is obtained with the exact DTBCs (4.31) on the larger domain  $[0, 2] \times [0, 2\pi]$ .

**Discretization and Results.** For the discretization parameters  $\Delta t = 0.002$ ,  $\Delta r = 1/64$ ,  $\Delta\theta = 2\pi/64$  we evolve the solution up to  $t = 0.5$ , as it is done in [JiGr06]. Hence, we calculate the solution for  $n = 250$  time steps. In the sum of exponentials we choose in three different calculations  $\nu = 2$ ,  $L = 10, 20, 40$ . We obtain the first  $2L + \nu - 1$  convolution coefficients exactly by the recursion formula (4.29) with a boundary value  $\ell_{J_\infty, m}^{(n)} := \ell_{\infty, m}^{(n)}$  taken from the 1D plane case  $\ell_{\infty, m}^{(n)} \equiv \ell_m^{(n)}$  from [ArEhSo03] for each mode  $m = 0, \dots, K - 1$  and summarize them according to (4.17). The sets  $\{b_{l, m}, q_{l, m}\}$ ,  $l = 1, \dots, L$  needed for the calculation of the approximated convolution coefficients  $\tilde{s}_m^{(n)}$ ,  $n > 2L + \nu - 1$  for all modes  $m$  are worked out by the Padé algorithm described in §4.3. We realized these calculations by a Maple code, within which we try to find  $L$  roots  $q_{l, m}$  of the polynomial  $Q_L(x)$  as it is described in Theorem 4.4 again for each mode. Due to a “nearly breakdown” by ill conditioned steps in the Lanczos algorithm (cf. [BuVa97]) it is not necessarily possible to find  $L$  roots of  $Q_{L, m}$  fulfilling the con-

## 4 DTBCs for the two dimensional Schrödinger equation on circular domains

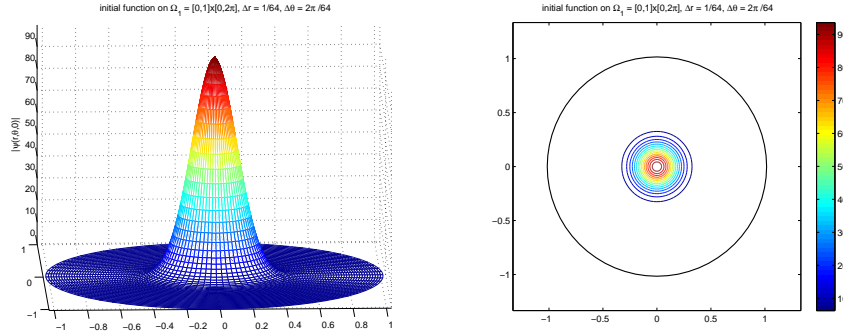


Figure 4.11: Example 3. Normal and contour plot of the absolute value of the initial function  $\psi^I$  (4.39) on the computational domain  $\Omega_1$ .

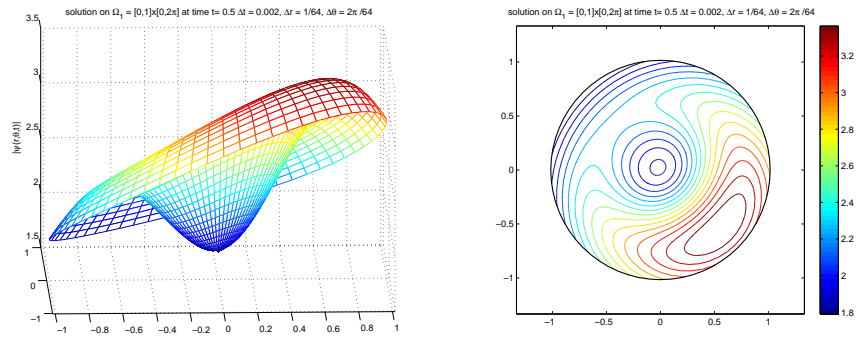
dition  $|q_{l,m}| > 1$ ,  $l = 1, \dots, L$  for all modes  $m = 0, \dots, K - 1$ . Consequently, the Maple code automatically chooses smaller and smaller values ( $L - 1, L - 2, \dots$ ) to guarantee that all roots have an absolute value larger than 1. E.g., with the initial choice  $L = 40$  you will find values for  $L$  fulfilling the above condition that vary from 18 to 32 for the different modes. The number of summands is hence just an initial guess for the final number of summands in the sum of exponential.

In Figure 4.12 we present plots and the contour plots of the absolute value of the solution  $\psi_1$  at time  $t = 0.5$  calculated with the approximated DTBCs with different values of  $L$ . For  $L = 10$  there are some unphysical reflections (see Figure 4.12(a)), for greater values of  $L$  these reflections become less (see Figure 4.12(b), 4.12(c)).

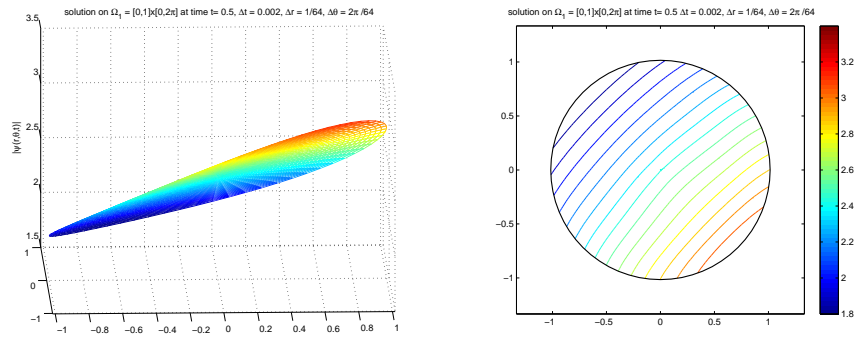
The error due to the approximated DTBCs is shown in Figure 4.13. For different initial choices of the number of coefficients  $L$  in the sum of exponentials we present the error  $L_{\Omega_1}(\psi_1, \psi_2, t_n)$  (cf. (4.37)) there. Although the coefficients  $s_m^{(n)}$ ,  $\tilde{s}_m^{(n)}$  are of different type (algebraic vs. exponential decay) the error stays bounded. In order to show that long time calculations with the approximated DTBCs are stable we evolve the initial data (4.39) with  $\alpha_x = \alpha_y = 0.01$  and  $k_x = k_y = 0$  for discretization parameters  $\Delta t = 0.002$ ,  $\Delta r = 1/64$ ,  $\Delta \theta = 2\pi/64$  for different initial choices of the number of summands  $L$  up to  $t = 20$ . The norm of the solution decays in time, as it is shown in Figure 4.14.

A typical plot of  $|s_m^{(n)} - \tilde{s}_m^{(n)}|$  versus the time steps  $n$  for the initial choice  $L = 40$  for all modes is given in Figure 4.15. Obviously only the first  $2L + \nu - 1$  coefficients (or even less if the root condition  $|q_l| > 1$  is not fulfilled) are exactly calculated, then you can observe a deviation between the exact and the approximated convolution coefficients.

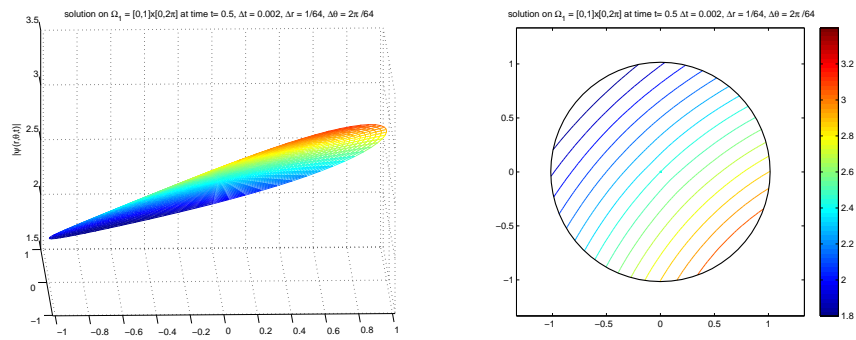
## 4.4 Numerical results



(a)  $L = 10$



(b)  $L = 20$



(c)  $L = 40$

Figure 4.12: Example 3. Normal and contour plots of the absolute value of the calculated solution  $\psi_1$  of (4.6) with the initial function (4.39) on the computational domain  $\Omega_1$ . We use approximated DTBCs with (a):  $L = 10$ , (b):  $L = 20$ , and (c):  $L = 40$  summands in the sum of exponentials.

## 4 DTBCs for the two dimensional Schrödinger equation on circular domains

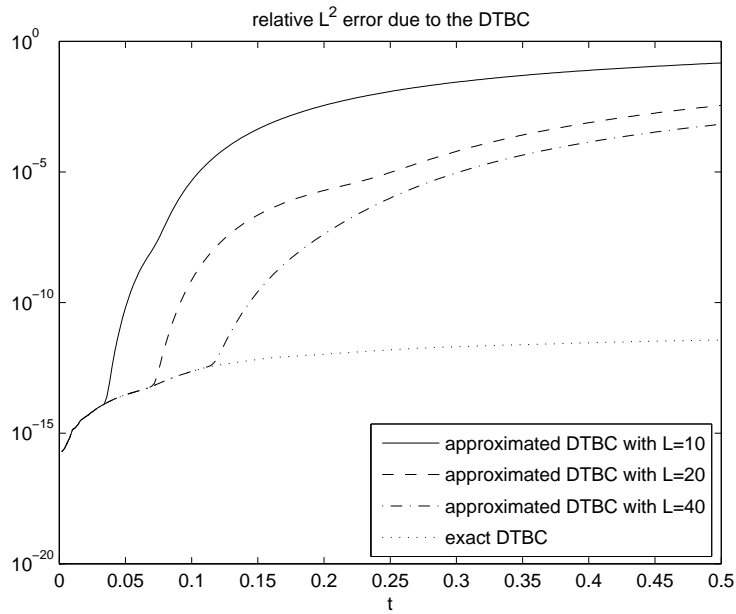


Figure 4.13: Example 3. Relative error  $L_{\Omega_1}(\psi_1, \psi_2, t_n)$  due to the approximated discrete TBCs for the time evolution of initial function (4.39) for different initial choices of the number  $L$  in the sum of exponentials, 10 (solid line), 20 (dashed line) and 40 grid points (dashed-pointed line). The relative error due to the exact discrete TBCs for this problem is plotted in the pointed line.

Let us finally remark that this approach for the 1D Schrödinger equation (including the Maple code) is presented at <http://www.dtbc.de.vu>.

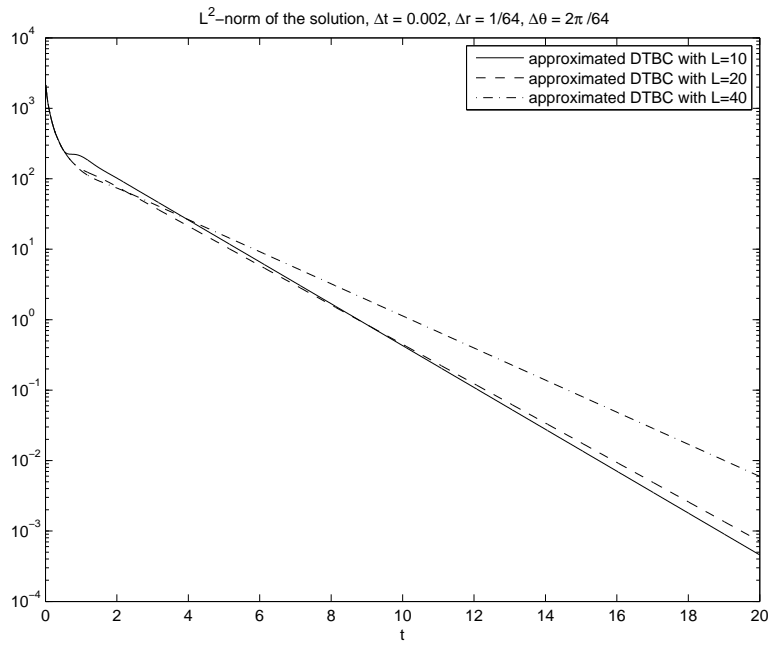


Figure 4.14: Example 3.  $L^2$ -norm of the long time evolution of the initial function (4.39) with  $\alpha_x = \alpha_y = 0.01$  and  $k_x = k_y = 0$  again for different initial choices of the number  $L$  in the sum of exponentials, 10 (solid line), 20 (dashed line) and 40 grid points (dashed-pointed line).

## 4 DTBCs for the two dimensional Schrödinger equation on circular domains

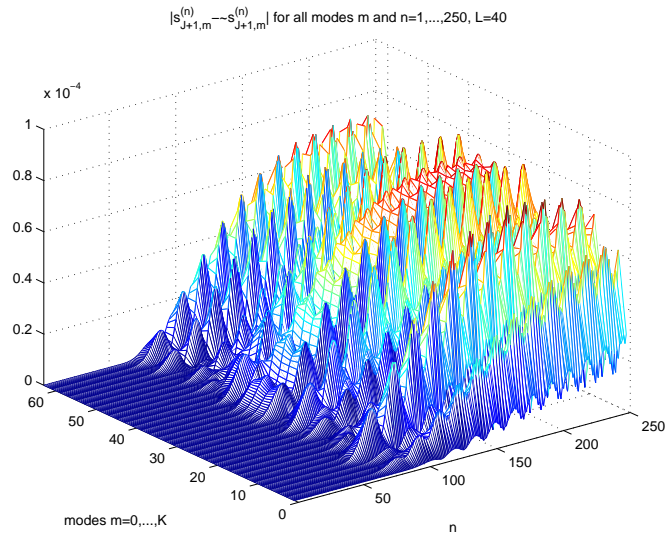


Figure 4.15: Example 3. Difference  $|s_m^{(n)} - \tilde{s}_m^{(n)}|$  as a function of time steps  $n = 0, \dots, 250$  (corresponding to  $0 \leq t \leq 0.5$ ) for the modes  $m = 0, \dots, K - 1$ , where  $\tilde{s}_m^{(n)}$  is calculated with the sum of exponentials ansatz with an initial choice of  $L = 40$  summands. We choose the same discretization parameters used in the calculations for Figure 4.12.

# Bibliography

- [AlRe02] I. Alonso–Mallo and N. Reguera: *Weak ill-posedness of spatial discretizations of absorbing boundary conditions for Schrödinger-type equations*, SIAM J. Numer. Anal. **40** (2002) 134–158
- [AlGrHa00] B. Alpert, L. Greengard and T. Hagstrom: *Rapid evaluation of nonreflecting boundary kernels for time-domain wave propagation*, SIAM J. Numer. Anal. **37** (2000) 1138–1164
- [AnBe03] X. Antoine and C. Besse: *Unconditionally stable discretization schemes of non-reflecting boundary conditions for the one-dimensional Schrödinger equation*, J. Comp. Phys. **188** (2003) 157–175
- [AnBeMo04] X. Antoine, C. Besse and V. Mouysset: *Numerical Schemes for the simulation of the two-dimensional Schrödinger equation using non-reflecting boundary conditions*, Math. Comp. **73** (2004) 1779–1799
- [Ar95] A. Arnold: *Numerically Absorbing Boundary Conditions for Quantum Evolution Equations*, VLSI Design **6** (1998) 313–319
- [ArEh98] A. Arnold and M. Ehrhardt: *Discrete transparent boundary conditions for wide angle parabolic equations in underwater acoustics*, J. Comp. Phys. **145** (1998) 611–638
- [ArEhSo03] A. Arnold, M. Ehrhardt and I. Sofronov: *Discrete transparent boundary conditions for the Schrödinger equation: Fast calculation, approximation, and stability*, Comm. Math. Sci. **1** (2003) 501–556
- [BaPo91] V.A. Baskakov and A.V. Popov: *Implementation of transparent boundaries for numerical solution of the Schrödinger equation*, Wave Motion **14** (1991) 123–128
- [BrDi95] C.H. Bruneau and L. Di Menza: *Conditions aux limites transparentes et artificielles pour l'équation de Schrödinger en dimension 1 d'espace*, C. R. Acad. Sci. Paris, Ser. I **320** (1995) 89–94
- [BuVa97] A. Bultheel and M. Van Barel: *Linear algebra, rational approximation and orthogonal polynomials*, Studies in Computational Mathematics 6, North-Holland (1997)

## Bibliography

---

- [DKSW01] A. Dedner, D. Kröner, I. Sofronov and M. Wesenberg: *Transparent Boundary Conditions for MHD Simulations in Stratified Atmospheres*, J. Comp. Phys. **171** (2001) 448–478
- [Do67] G. Doetsch: *Anleitung zum praktischen Gebrauch der Laplace-Transformation und der  $\mathcal{Z}$ -Transformation*, R. Oldenbourg Verlag München, Wien, 3. Auflage (1967)
- [EhAr01] M. Ehrhardt and A. Arnold: *Discrete Transparent Boundary Conditions for the Schrödinger Equation*, Riv. Mat. Univ. Parma **6** (2001) 57–108
- [GrSt90] L. Greengard and J. Strain: *A fast algorithm for the evaluation of heat potentials*, Comm. Pure Appl. Math. **43** (1990) 949–963
- [Ha99] T. Hagstrom: *Radiation boundary conditions for the numerical simulation of waves*, Iserles, A. (ed.), Acta Numerica **8** (1999) 47–106, Cambridge: Cambridge University Press, 47–106
- [HaHu04] H. Han and Z. Huang: *Exact Artificial Boundary Conditions for the Schrödinger Equation in  $\mathbb{R}^2$* , Comm. Math. Sci. **2** (2004) 79–94
- [JiGr06] S. Jiang and L. Greengard: *Efficient Representation of Nonreflecting Boundary Conditions for the Time-Dependent Schrödinger Equation in Two Dimensions*, to appear in Commun. Pure Appl. Math.
- [Ke83] G.E. Keiser: *Optical Fiber Communication*, McGraw–Hill, New York (1983)
- [Lev00] M.F. Levy: *Parabolic equation models for electromagnetic wave propagation*, IEE Electromagnetic Waves Series **45** (2000)
- [Ma89] B. Mayfield: *Non-local boundary conditions for the Schrödinger equation*, Ph. D. thesis, University of Rhode Island, Providence, RI (1989)
- [Sc99] A. Schädle: *Non-reflecting boundary conditions for the two dimensional Schrödinger equation*, Wave Motion **35** (2002) 181–188
- [ScDe95] F. Schmidt and P. Deuffhard: *Discrete transparent boundary conditions for the numerical solution of Fresnel’s equation*, Comput. Math. Appl. **29** (1995) 53–76
- [So93] I.L. Sofronov: *Conditions for Complete Transparency on the Sphere for the Three-Dimensional Wave Equation*, Russian Acad. Sci. Dokl. Math. **46** (1993) 397–401

- [So98a] I.L. Sofronov: *Artificial Boundary Conditions of Absolute Transparency for Two- and Threedimensional External Time-Dependent Scattering Problems*, Euro. J. Appl. Math. **9** (1998) 561–588
- [So98b] I.L. Sofronov: *Non-reflecting inflow and outflow in wind tunnel for transonic time-accurate simulation*, J. Math. Anal. Appl. **221** (1998) 92–115
- [Ta77] F.D. Tappert: *The parabolic approximation method*, in *Wave Propagation and Underwater Acoustics*, Lecture Notes in Physics 70, eds. J.B. Keller and J.S. Papadakis, Springer, New York (1977) 224–287
- [Za01] B. Zamzow: *Simulation von Glasfaserspleißen mit der Beam-Propagation-Methode*, Fortschritt-Berichte VDI Reihe 10, Nr. 655, Düsseldorf, VDI Verlag (2001)